

## ABSTRACT

Title of Dissertation: DEVELOPMENT OF SELF-ASSEMBLED ZnO  
NANOSTRUCTURES IN DIBLOCK COPOLYMERS  
ON LARGE AREA Si WAFERS AND GAS SENSOR  
APPLICATIONS

Hasina Afroz Ali, Doctor of Philosophy, 2008

Dissertation Directed By: Agis A. Iliadis

Department of Electrical and Computer Engineering

ZnO nanoparticles with improved optical properties and increased surface areas have the potential for advanced optoelectronic, gas sensor and biosensor applications. In order to exploit these unique properties of ZnO nanoparticles for the realization of nanoscale devices, we developed novel techniques for the self-assembly and functionalization of ZnO nanoparticles through diblock copolymers on large area (100)Si surfaces. These novel techniques allowed us to subsequently develop the first ZnO nanoparticle based device. Thus, a novel ZnO-nanocomposite/Si n-p heterojunction diode and a high performance hydrogen gas nanosensor have been developed, for the first time.

The thesis presents the novel technique developed for the self-assembly of ZnO nanostructures with spherical morphology through diblock copolymers on large area Si substrates. Correlation between the physical parameters of the nanoparticles

and the copolymers was evaluated from AFM studies. Control of the nanoparticle size and density was achieved by varying copolymer block lengths. The largest nanoparticles had average sizes of 250 nm and densities of  $1 \times 10^7 \text{cm}^{-2}$  while the smallest nanoparticles had average sizes of 20 nm and densities of  $1 \times 10^{10} \text{cm}^{-2}$ . XRD studies showed that the wurtzite crystal structured nanoparticles assumed the same orientation (100) as the Si substrate, indicating a pseudo-epitaxial nanostructure. Room temperature photoluminescence studies showed quantum confinement effects with a blue shift from 372 nm (large particles) to 363 nm (small particles). A broad defect related green-yellow luminescence centered at 555 nm indicative of n-type conductivity of the nanoparticles was also observed.

The n-type nanoparticles on p-type Si resulted in the development of a ZnO-nanocomposite/pSi n-p heterojunction diode for the first time. The nanodiode showed good rectification and low leakage currents. LogI-V characteristics gave built-in voltages of 0.69 and 0.7 eV, saturation currents of 2 and  $2.34 \times 10^{-8} \text{A}$ , and ideality factors of 5.9 and 5.7 for the small and large particles, respectively. The transport mechanisms of the nano-diodes were studied. C-V characteristics showed abrupt p-n junctions, suggesting an intimate junction interface consistent with the pseudo-epitaxial nature of the structure. A novel hydrogen gas nanosensor based on the ZnO-nanocomposite/Si heterojunction diode was developed for high sensitivity, rapid, room temperature sensing. Response and recovery times were reduced by a factor of 100 and smaller and denser nanoparticles were found to be faster and more sensitive.

DEVELOPMENT OF SELF-ASSEMBLED ZnO NANOSTRUCTURES IN  
DIBLOCK COPOLYMERS ON LARGE AREA Si WAFERS FOR  
GAS SENSOR APPLICATIONS

By

Hasina Afroz Ali

Dissertation submitted to the Faculty of the Graduate School of the  
University of Maryland, College Park in partial fulfillment  
of the requirements of the degree of  
Doctor of Philosophy  
2008

Advisory Committee:  
Professor Agis A. Iliadis, Advisor/Chair  
Professor Lourdes Salamanca-Riba  
Professor Martin Peckerar  
Professor Robert Newcomb  
Professor Luz Martinez-Miranda

© Copyright by  
Hasina Afroz Ali  
2008

## DEDICATION

To my parents and brothers  
for their endless love and support

## ACKNOWLEDGEMENTS

First and foremost I would like to express my sincere gratitude to my advisor, Agis Iliadis, for his continuous support and guidance during my years in graduate school. I am grateful to him for giving me the opportunity to work in the emerging field of semiconductor nanoscience and nanotechnology. This dissertation would not have been possible without his invaluable insights and encouragement throughout the course of my research work.

I am grateful to Dr. Unchul Lee of Army Research Lab (ARL) for performing the XPS measurements for us that were needed for the chemical analysis of our nanomaterials. I would also like to thank Dr. Martinez-Miranda for all her help and guidance with the XRD measurements. I greatly value and appreciate all her instructive suggestions and invaluable insights into the structural characterization of nanomaterials in our work.

I would like to thank Dr Martin Peckerar for his guidance during the course of my research. I would also like to thank Dr Newcomb and Dr Salamanca-Riba for taking the time to serve on my dissertation committee.

I appreciate the support of the National Science Foundation (NSF) in funding my research. I owe many thanks to Dr Michael Fuhrer and his student, Yung-Fu Chen from the Department of Physics, for extending their help with the AFM measurements.

Many thanks to Tom Loughran, Fablab engineer of Maryland Nanocenter, for lending his support and valuable time in assisting with the lab work. I appreciate his

help in maintaining equipments and clean room resources, and setting up experiments. John Abrahams, Fablab engineer of Maryland Nanocenter, is another person I am very grateful to for his help with electrical measurement setup.

I would also like to include my colleagues Soumya Krishanmoorthy, Kyechong Kim and Saeed Esmaili Sardari at the Semiconductor Research lab among the people whose support I greatly appreciate. They gave me moral support and served as my permanent sounding boards for my research ideas and sometimes for my research frustrations too.

My parents, Fouzia and Hatem Ali have been my greatest source of inspiration and strength. I am deeply indebted to them for their unconditional love and support throughout the years, for their hard work to give me the best in life and for giving me the confidence and encouragement to achieve my dreams. I would also like to take this opportunity to say thanks to my brothers Saadi and Mehdi for always being there for me.

## TABLE OF CONTENTS

LIST OF FIGURES .....	x
<b>CHAPTER 1: INTRODUCTION.....</b>	<b>1</b>
1.1 CONTRIBUTIONS .....	5
1.2 BACKGROUND .....	7
1.2.1 Semiconductor Nanoparticle Properties .....	7
1.2.2 Material Properties of ZnO .....	11
1.3 OUTLINE OF THESIS.....	12
<b>CHAPTER 2: SELF-ASSEMBLY OF NANOSTRUCTURES IN DIBLOCK     COPOLYMERS .....</b>	<b>14</b>
2.1 BACKGROUND .....	14
2.1.1 Block Copolymers .....	14
2.1.2 Nanoparticle synthesis through diblock copolymer self-assembly.....	18
2.2 DEVELOPMENT OF SELF-ASSEMBLY OF ZnO NANOPARTICLES FOR LARGE AREA APPLICATIONS.....	20
2.3 DIBLOCK COPOLYMERS USED IN OUR WORK.....	22
2.4 EXPERIMENTAL PROCEDURE .....	25
2.5 COMPATIBILITY OF THE SELF-ASSEMBLY PROCESS WITH DEVICE FABRICATION TECHNOLOGY .....	29
<b>CHAPTER 3: EVALUATION OF ZnO NANOSTRUCTURE SELF-     ASSEMBLY ON Si SURFACES .....</b>	<b>32</b>
3.1 CHARACTERIZATION TECHNIQUES .....	32



3.1.1	Fourier Transform Infrared Spectroscopy (FTIR) .....	32
3.1.2	X-ray Photoelectron Spectroscopy (XPS) .....	33
3.2.	RESULTS AND DISCUSSIONS.....	34
3.2.1	Fourier Transform Infrared Spectroscopy (FTIR) .....	34
3.2.2	X-ray Photoelectron Spectroscopy (XPS) .....	37
3.2.3	Reactive Ion Etching of the polymer matrix .....	42
3.2.4	Microscope images of ZnO nanoparticles in diblock copolymer .....	43
 <b>CHAPTER 4: MORPHOLOGICAL, STRUCTURAL AND OPTICAL</b>		
<b>CHARACTERIZATION OF ZnO NANOSTRUCTURES ON Si</b>		
	<b>SURFACES .....</b>	<b>46</b>
4.1	CHARACTERIZATION TECHNIQUES .....	46
4.1.1	Atomic Force Microscopy (AFM) .....	46
4.1.2	X-ray Diffraction Spectroscopy (XRD).....	47
4.1.3	Photoluminescence (PL) spectroscopy .....	49
4.2.	RESULTS AND DISCUSSIONS.....	51
4.2.1	AFM studies of the ZnO nanoparticles in copolymer on Si substrate ..	51
4.2.2	Structural characteristics of the ZnO nanoparticles in copolymer on Si substrate .....	63
4.2.3	Optical characteristics of the ZnO nanoparticles in copolymer on Si substrate .....	68
4.3	SUMMARY .....	71

<b>CHAPTER 5: ELECTRICAL CHARACTERIZATION OF ZnO-</b>	
<b>    COPOLYMER-NANOCOMPOSITE/Si HETEROSTRUCTURES.....</b>	<b>72</b>
5.1 BACKGROUND .....	72
5.1.1 P-N Heterojunction Diodes.....	72
5.1.2 Evaluation Techniques of P-N Diode Characteristics .....	76
5.2 ENERGY BAND DIAGRAM OF n-ZnO/p-Si HETEROJUNCTION.....	81
5.3 EXPERIMENTAL DETAILS .....	84
5.4 ELECTRICAL CHARACTERISTICS OF Al/n-ZnO-[PS] <sub>159</sub> [PAA] <sub>63</sub> /p-Si	
HETEROSTRUCTURE .....	85
5.4.1 Current-Voltage Characteristics.....	85
5.4.2 Capacitance-Voltage Characteristics .....	98
5.5 ELECTRICAL CHARACTERISTICS OF Au/n-ZnO-[PS] <sub>159</sub> [PAA] <sub>63</sub> /p-Si	
HETEROSTRUCTURE .....	100
5.6 ELECTRICAL CHARACTERISTICS OF Au/n-ZnO-[PS] <sub>106</sub> [PAA] <sub>4</sub> /p-Si	
HETEROSTRUCTURE .....	106
5.7 SUMMARY.....	113
<b>CHAPTER 6: DEVELOPMENT OF HIGH PERFORMANCE ZnO GAS</b>	
<b>    NANO-SENSOR DEVICES.....</b>	<b>115</b>
6.1 GAS DETECTION MECHANISM.....	115
6.1.1 ZnO Surface Metal and Target Gas Catalytic Mechanism .....	118
6.1.2 Reducing Gas Direct Interaction with ZnO Surface .....	119
6.1.3 Field Assisted Gas Detection by n- ZnO/p-Si Heterojunction Diodes	121
6.2 EXPERIMENTAL DETAILS .....	122

6.3 GAS SENSING PROPERTIES OF Au/ZnO-[PS] <sub>159</sub> [PAA] <sub>63</sub> /Si	
HETEROJUNCTION DIODES.....	123
6.4 GAS SENSING PROPERTIES OF Au/ZnO-[PS] <sub>106</sub> [PAA] <sub>4</sub> /Si	
HETEROJUNCTION DIODES.....	128
6.5 SUMMARY.....	131
<b>CHAPTER 7: CONCLUSIONS .....</b>	<b>133</b>
<b>BIBLIOGRAPHY.....</b>	<b>137</b>

## LIST OF FIGURES

Figure 2-1. Schematic of different classes of copolymers depending on the arrangement of chemically distinct polymer blocks or monomers.....	15
Figure. 2-2. Diblock copolymer composed of a majority block polymer and a minority block polymer covalently bonded and chemically distinct to each other.....	17
Figure 2-3. Schematic of a microdomain formed after phase separation between the majority and the minority blocks of diblock copolymer in solid phase. .	17
Figure 2-4. Morphologies of the microdomains formed by minority blocks in the matrix of majority blocks of the block copolymer .....	17
Figure 2-5. Chemical structures of the diblock copolymers used in our work. ....	23
Figure 2-6. Schematic of the synthesis process of ZnO nanoparticles via self-assembly in diblock copolymer. ....	24
Figure 2-7. Optical micrograph of photolithographic patterning of the copolymer film on a Si wafer .....	31
Figure 2-8. Optical micrograph of interdigitated pattern with Al metallization on copolymer on Si surface. ....	31
Figure 3-1. FTIR spectrum of the undoped copolymer. The peak at $1710\text{ cm}^{-1}$ is due to the carboxylic group. ....	35

Figure 3-2. FTIR spectrum of the precursor-doped copolymer. The peak at $1630\text{ cm}^{-1}$ is due to the Zn-carboxylate. Partial neutralization of the carboxylic also is evident due to the presence of the $1710\text{ cm}^{-1}$ peak also.....	36
Figure 3-3. XPS spectra of the $\text{ZnCl}_2$ - $[\text{PS}]_{159}/[\text{PAA}]_{63}$ nanocomposite before ozone exposure and the $\text{ZnO}$ - $[\text{PS}]_{159}/[\text{PAA}]_{63}$ nanocomposite films after ozone exposure spin-cast on (100) Si wafer.....	39
Figure 3-4. High resolution XPS data of the Zn $2p_{3/2}$ peak for the $[\text{PS}]_{159}/[\text{PAA}]_{63}$ copolymer system on Si surface before and after ozone treatment, showing shift in the binding energy of Zn $2p_{3/2}$ electron peak.....	40
Figure 3-5. Comparison of the wet $\text{NH}_4\text{OH}$ and dry ozone treatment methods for the conversion of the precursor to ZnO in the spherical domains of the $[\text{PS}]_{159}/[\text{PAA}]_{63}$ copolymer .....	41
Figure 3-6. XPS spectrum of ZnO nanoclusters after removal of copolymer matrix from the Si surface by reactive ion etching using a gas mixture of $\text{CF}_4$ and $\text{O}_2$ with a ratio of 2:1 for 1 min. ....	42
Figure 3-7. SEM image of ZnO nanoparticles developed in $[\text{PS}]_{159}/[\text{PAA}]_{63}$ copolymer on p(100) Si substrate .....	43
Figure 3-8. TEM image of ZnO nanoparticles developed in $[\text{NOR}]_{400}/[\text{NORCOOH}]_{50}$ copolymer .....	44
Figure 3-9. Atomic force micrograph (scan area size of $5 \times 5\text{um}$ ) of the ZnO- $[\text{PS}]_{318}/[\text{PMAA}]_{78}$ nanocomposite film on Si surface.....	45
Figure 4-1. Setup for $\theta$ - $2\theta$ scan of sample .....	48

Figure 4-2. 2-D and 3-D AFM image of ZnO nanoclusters in [PS] <sub>159</sub> /[PAA] <sub>63</sub> system on Si surface in a 4.5x4.5 μm scan area. ....	53
Figure 4-3. Linear surface scan profile across one of the nanoparticles indicated by the arrow in the AFM image of fig. 4-2. The profile shows the lateral size and height of the nanoparticle to be about 350 nm and 124 nm, respectively. ....	53
Figure 4-4. 2-D AFM topographic image (3x3 μm scan area) of the ZnO-[PS] <sub>139</sub> /[PAA] <sub>17</sub> nanocomposite film on (100) p-Si surface. ZnO nanostructures are observed to have lateral size distribution between 40 and 80 nm. ....	54
Figure 4-5. 3-D AFM topographic image (3x3 μm scan area) corresponding to fig. 4-4 of the ZnO-[PS] <sub>139</sub> /[PAA] <sub>17</sub> nanocomposite film on (100) p-Si surface. ....	54
Figure 4-6. 2-D AFM topographic image (2.5x2.5 μm scan area) of the ZnO-[PS] <sub>106</sub> /[PAA] <sub>17</sub> nanocomposite film on (100) p-Si surface. ZnO nanostructures are observed to have lateral size distribution between 40 and 140 nm. ....	55
Figure 4-7. 3-D AFM topographic image (2.5x2.5 μm scan area) corresponding to fig. 4-6 of the ZnO-[PS] <sub>106</sub> /[PAA] <sub>17</sub> nanocomposite film on (100) p-Si surface. ....	55
Figure 4-8. 2-D AFM topographic image (938x938 nm scan area) of the ZnO-[PS] <sub>106</sub> /[PAA] <sub>4</sub> nanocomposite film on (100) p-Si surface. ZnO nanostructures are observed to have lateral size distribution between 10 and 60 nm. ....	56

Figure 4-9. 3-D AFM topographic image (936x936 nm scan area) corresponding to fig. 4-8 of the ZnO-[PS] <sub>106</sub> /[PAA] <sub>4</sub> nanocomposite film on (100) p-Si surface.....	56
Figure 4-10. Schematic of a copolymer film with spherical nanodomains (grey regions) formed by minority blocks ( ) within the matrix formed by majority blocks ( ) of the copolymer. ....	59
Figure 4-11. Schematic of a copolymer film with decreased minority block lengths with respect to that of fig. 4-10, resulting in decreased domain size compared to that of fig. 4-10. ....	59
Figure 4-12. Schematic of a copolymer film with increased majority block lengths with respect to that of fig. 4-10, resulting in decreased domain density compared to that of fig. 4-10. ....	59
Figure 4-13. Dependence of average size of ZnO nanoparticles in [PS] <sub>m</sub> /[PAA] <sub>n</sub> copolymer on minority block length, n.....	60
Figure 4-14. Dependence of average density of ZnO nanoparticles in [PS] <sub>m</sub> /[PAA] <sub>n</sub> copolymer on majority block length, m.....	60
Figure 4-15. 2-D and 3-D AFM image of over-doped ZnO-[PS] <sub>106</sub> /[PAA] <sub>17</sub> nanocomposite films on SiO <sub>2</sub> /Si surface in a 15x15 μm scan area. ....	62
Figure 4-16. θ-2θ XRD pattern of ZnO nanoparticles in [PS] <sub>159</sub> /[PAA] <sub>63</sub> copolymer on (100) Si substrate. ....	65
Figure 4-17. XRD rocking curve corresponding to the (100) diffraction peak of ZnO nanoparticles developed in [PS] <sub>159</sub> /[PAA] <sub>63</sub> copolymer.....	66

Figure 4-18. XRD rocking curve corresponding to the (101) diffraction peak of ZnO nanoparticles developed in [PS] <sub>159</sub> /[PAA] <sub>63</sub> copolymer.....	66
Figure 4-19. XRD rocking curve corresponding to the (200) diffraction peak of ZnO nanoparticles developed in [PS] <sub>159</sub> /[PAA] <sub>63</sub> copolymer.....	67
Figure 4-20. Photoluminescence spectrum of 250 nm ZnO nanoparticles in [PS] <sub>159</sub> /[PAA] <sub>63</sub> copolymer at room temperature .....	70
Figure 4-21. Photoluminescence spectrum of 20 nm ZnO nanoparticles in [PS] <sub>109</sub> /[PAA] <sub>4</sub> copolymer at room temperature.....	70
Figure 5-1. Types of energy band alignments in heterojunction diodes.....	73
Figure 5-2. Schematic of log I-V characteristics of a practical p-n junction diode ....	79
Figure 5-3. Energy band diagram of n-ZnO and p-Si before junction formation.....	83
Figure 5-4. Energy band diagram of an abrupt n-ZnO/p-Si heterojunction at thermal equilibrium.....	83
Figure 5-5. Schematic of metal/ZnO-nanocomposite/p-Si structure used for electrical measurements at room temperature .....	84
Figure 5-6. I-V plot of Al/n-ZnO-[PS] <sub>159</sub> /[PAA] <sub>63</sub> -nanocomposite/p-Si heterostructure measured at room temperature.....	87
Figure 5-7. Log I-V plot corresponding to the I-V plot of Al/n-ZnO-[PS] <sub>159</sub> /[PAA] <sub>63</sub> -nanocomposite/p-Si heterostructure of fig. 5-6 .....	87
Figure 5-8. Log I-V plot of Al/[PS] <sub>159</sub> /[PAA] <sub>63</sub> copolymer/p-Si heterostructure.....	88



Figure 5-9. LogI-logV plot of Al/[PS] <sub>159</sub> /[PAA] <sub>63</sub> copolymer/p-Si heterostructure...	88
Figure 5-10. Series Resistance of Al/n-ZnO-[PS] <sub>159</sub> /[PAA] <sub>63</sub> -nanocomposite/p-Si heterostructure evaluated using ΔV-I plot corresponding to the logI-V..	89
Figure 5-11. Energy band diagram of an abrupt ZnO/Si heterojunction under forward bias (holes are represented by $\square$ and electrons are represented by $\circ$ ) .....	92
Figure 5-12. Log I-logV plot corresponding to the linear region of the logI-V plot of Al/n-ZnO-[PS] <sub>159</sub> /[PAA] <sub>63</sub> -nanocomposite/p-Si heterostructure of fig. 5-7. The thick line is experimental plot and thin line is fitted plot. ....	95
Figure 5-13. LogI-logV characteristics of Al/n-ZnO-[PS] <sub>159</sub> /[PAA] <sub>63</sub> -nanocomposite/p-Si heterostructure at low bias region, below 0.3 V > V > 0.5 V. ....	96
Figure 5-14. Log I-V <sub>j</sub> plot corresponding to the I-V plot of Al/n-ZnO-[PS] <sub>159</sub> /[PAA] <sub>63</sub> -nanocomposite/p-Si heterostructure of fig. 5-6 after series resistance (R <sub>s</sub> ) correction. ....	97
Figure 5-15. C-V plot of Al/n-ZnO-[PS] <sub>159</sub> /[PAA] <sub>63</sub> -nanocomposite/p-Si heterostructure measured at 100 kHz at room temperature .....	99
Figure 5-16. 1/C <sup>2</sup> -V plot of Au/n-ZnO-[PS] <sub>159</sub> /[PAA] <sub>63</sub> -nanocomposite/p-Si heterostructure corresponding to the C-V plot in fig. 5-15 .....	99
Figure 5-17. I-V plot of Au/n-ZnO-[PS] <sub>159</sub> /[PAA] <sub>63</sub> -nanocomposite/p-Si heterostructure measured at room temperature.....	104
Figure 5-18. Log I-V plot corresponding to the I-V plot of Au/n-ZnO-[PS] <sub>159</sub> /[PAA] <sub>63</sub> -nanocomposite/p-Si heterostructure of Figure 5-17 ...	104

Figure 5-19. LogI-logV characteristics of Au/n-ZnO-[PS] <sub>159</sub> /[PAA] <sub>63</sub> -nanocomposite/p-Si heterostructure at low bias region, $0.3 \text{ V} > V > 1.0 \text{ V}$ . .....	105
Figure 5-20. Log I-V <sub>j</sub> plot corresponding to the I-V plot of Au /n-ZnO-[PS] <sub>159</sub> /[PAA] <sub>63</sub> -nanocomposite/p-Si heterostructure of fig. 5-17 after series resistance (R <sub>s</sub> ) correction.....	105
Figure 5-21. I-V plot of Au/n-ZnO-[PS] <sub>106</sub> /[PAA] <sub>4</sub> -nanocomposite/p-Si heterostructure measured at room temperature.....	110
Figure 5-22. Log I-V plot corresponding to the I-V plot of Au/n-ZnO-[PS] <sub>106</sub> /[PAA] <sub>4</sub> -nanocomposite/p-Si heterostructure of fig. 5-21 .....	110
Figure 5-23. LogI-logV characteristics of Au/n-ZnO-[PS] <sub>106</sub> /[PAA] <sub>4</sub> -nanocomposite/p-Si heterostructure showing bias dependent current-voltage relation at bias regions of $0.2 \text{ V} > V > 1 \text{ V}$ (exponential behavior) and $1 \text{ V} > V > 2 \text{ V}$ (power-law behavior).....	111
Figure 6- 1. Schematic of the Au/ZnO-nanocomposite/Si structure developed for the realization of the novel nanosensor in our work with the three sequential processes involved in the gas detection mechanism labeled. ....	117
Figure 6-2. Schematic of ZnO-nanocomposite/p-Si structure used for H <sub>2</sub> gas sensing measurements at room temperature .....	122
Figure 6-3. I-V characteristics of ZnO-nanocomposite/p-Si heterojunction in [PS] <sub>159</sub> /[PAA] <sub>63</sub> copolymer system, with the 250nm average sized ZnO particles, under 10% H <sub>2</sub> (N <sub>2</sub> carrier gas) flow, at room temperature .....	125

Figure 6-4. Dynamic response of ZnO-nanocomposite/Si p-n heterojunction in [PS]<sub>159</sub>/[PAA]<sub>63</sub> copolymer system, with the 250nm average sized ZnO particles, under 10% H<sub>2</sub> (N<sub>2</sub> carrier gas) flow, at room temperature for different applied voltages ..... 126

Figure 6-5. Dynamic response of ZnO-nanocomposite/Si p-n heterojunction in [PS]<sub>159</sub>/[PAA]<sub>63</sub> copolymer system, with the 250nm average sized ZnO particles, under 3% H<sub>2</sub> (N<sub>2</sub> carrier gas) flow, at room temperature ..... 127

Figure 6-6. Dynamic response of ZnO-nanocomposite/Si p-n heterojunction in [PS]<sub>106</sub>/[PAA]<sub>4</sub> copolymer system, with the 20nm average sized ZnO particles, under 10% H<sub>2</sub> (N<sub>2</sub> carrier gas) flow, at room temperature ..... 129

Figure 6-7. Dynamic response of ZnO-nanocomposite/Si p-n heterojunction in [PS]<sub>106</sub>/[PAA]<sub>4</sub> copolymer system, with the 20nm average sized ZnO particles, under 3% H<sub>2</sub> (N<sub>2</sub> carrier gas) flow, at room temperature ..... 130

## **CHAPTER 1**

### **INTRODUCTION**

In recent years, ZnO has been of interest to researchers for its promising use in electronics, optoelectronics, and sensors. It has a direct energy band gap of 3.3 eV at room temperature and a large exciton binding energy of 60meV, allowing a high degree of stability for excitonic transitions at room temperature. This makes it a promising material for UV optoelectronic devices [1, 2, 3] such as UV light emitting diodes, and photodetectors. ZnO crystallizes in the wurtzite structure and exhibits strong piezoelectric properties [4, 5] when the c-axis is oriented perpendicular to the substrate. This property of ZnO along with its gas-sensing capabilities, and transparency to visible light, make it one of the technologically important material systems for surface acoustic wave (SAW) devices [6, 7], gas sensors [8, 9], and solar cells [10]. These remarkable intrinsic properties of ZnO material can be further enhanced through nanotechnology. ZnO nanoparticles with improved optical properties [11] and increased surface areas have the potential for advanced optoelectronic, gas sensor and biosensor applications.

In order to exploit these unique properties of ZnO nanoparticles for the realization of nanoscale devices, we developed novel techniques for the self-assembly and functionalization of ZnO nanoparticles through diblock copolymers on large area Si surfaces at room temperature. It was through our work that the first approach towards functionalization of ZnO nanoparticles on substrates was ever taken [12, 13]. There have been no reports of prior work on the development of ZnO nanoparticles

## CHAPTER 1: INTRODUCTION

on technologically important substrates. Our self-assembly approach involves template assisted self-assembly of ZnO nanostructures on large area Si surfaces using diblock copolymers at room temperature. This bottom-up approach of self-assembly has the advantage of inexpensive mass fabrication and attainment of atomic feature size [14]. The diblock copolymers provide the templates through their microphase separation and formation of nanosized domains [15]. Along with templating, the copolymer matrix also provides mechanical stability and kinetic hindrance to the agglomeration of the ZnO particles thus eliminating the need of organic capping agents as has been used in other synthesis techniques for particle size control [16]. Another advantage of using the copolymers is their easier processing capability for large area wafer application. Moreover, the size and density control of the nanoparticles on Si substrates with the diblock copolymer block lengths open up new endless possibilities for advanced optoelectronic and sensing devices as evident from size dependent optical properties and surface area dependent sensing properties of semiconductor nanostructures [17].

In the last few years, there have been some reports of ZnO nanoparticle synthesis on Si substrates using physical methods like metalorganic chemical vapor deposition [18, 19, 20], pulsed laser deposition [21], focused-ion beam evaporation [22], and reactive electron beam evaporation [23]. However, these physical methods have several drawbacks such as difficulty in controlling nanoparticle size, and density and hence their properties, long processing times, high temperature growth conditions, and the complex experimental setup required by these techniques. Thus, in terms of process complexity, processing conditions, size and density control of the

## CHAPTER 1: INTRODUCTION

nanoparticles our approach can be considered the most economic, simplest, and fastest synthesis route for functionalization of high quality ZnO nanoparticles on Si surfaces.

The choice of substrate in our work was motivated by the potential for monolithic integration of ZnO nanoparticles-based devices with CMOS peripheral circuitry and for increased functionality of CMOS integrated chips. There is a great preference in the semiconductor industry for the system-on-a-chip with as many different functional devices on one Si chip and nanotechnologies which may be integrated on the chip would be the preferred route. So the ZnO nanoparticle delivery process was developed to be compatible with the CMOS device processing technology, using spin-on application of the nanocomposite ZnO-diblock polymer on Si wafer surfaces.

The n-type ZnO nanoparticles on p-type Si was targeting the development of ZnO nano-diodes, the realization of which has been accomplished in this work. The ZnO-nanocomposite/pSi n-p heterojunction diode is presented here for the first time. Such ZnO-nanocomposite/pSi heterojunction diode helps provide a functional basis from which to develop other p-n junction based nanodevices like UV light emitting diodes, UV photodetectors, and field-assisted nano-sensor devices to realize the unique properties of ZnO nanoparticles into devices.

The development of the ZnO-nanocomposite/pSi heterojunction structure led to the development of a unique high sensitivity, rapid, gas nano-sensor operating at room temperature. ZnO has an important yet little recognized property that makes it very promising for gas sensing, that is the high reactivity of its surface. ZnO has a

## CHAPTER 1: INTRODUCTION

surface with a high isoelectronic point (IEP) of 9.5, which is substantially higher than most gases and provides a strong driving force for the gas molecules to adsorb on the surface, hence making it the metal oxide of choice for gas sensing applications.

Gas sensors are key components in environmental, biomedical, and safety protection applications. Hydrogen is well established as the fuel material for energy generation in fuel cell electric generators, as it is a clean and efficient fuel, and its detection in automotive and other critical applications is essential. Recent advances in the development of ZnO nanostructured materials especially for large area applications provided the opportunity to improve dramatically the sensitivity of hydrogen gas sensors. Such improvement is due to the increase in surface-to-volume ratios that allow more gas molecules to quickly diffuse-in and be adsorbed on the surface for detection. Reports on ZnO nanostructure based hydrogen gas sensors [24] showed promise of improving sensitivity and response time compared to ZnO bulk/film gas sensors with increased surface area.

Moreover, for effective gas sensing metal oxides require elevated temperatures (300-450°C) which increase complexity, reduce autonomy due to increased power budgets, and prohibit use in highly unstable explosive environments. The reports on ZnO nanorod-based sensors showed promise of reducing the working temperature of the sensors by introducing a metal/semiconductor rectifying contact (Schottky barrier diode) to assist with the gas sensing [25]. In our work we have also developed a Schottky assisted H<sub>2</sub> gas nano-sensor [105]. However, in this work we have found that the introduction of the novel nano-heterojunction p-n diode dramatically reduces the response and recovery times, increases sensitivity, and

## CHAPTER 1: INTRODUCTION

reduces the effective temperature of operation to room temperature. Developing the ZnO nanoparticles on large area Si substrates also enables the monolithic integration of these ‘nanosensors’ with advanced CMOS technology for read-out and processing circuitry.

In this thesis we focus on the functionalization of ZnO nanoparticles on large area Si surfaces, characterization of the developed nanoparticles on Si substrates, development of novel ZnO nanoparticle-based heterojunction diodes, and development of high performance gas nano-sensors.

### 1.1 CONTRIBUTIONS

The major contributions of our work are:

- **Self-assembly of ZnO nanoparticles** – We developed a novel procedure for the self-assembly of ZnO nanostructures with spherical morphology. This was accomplished by diblock copolymer self-assembly. The synthesis process was developed to be compatible with the CMOS device processing technology.
- **Size and density control of ZnO nanoparticles** – The size and density of the ZnO nanoparticles was controlled by varying the copolymer block lengths. The correlation between the physical parameters of the ZnO nanoparticles and the copolymer was determined.
- **Functionalization of ZnO nanoparticles on Si substrates** – The self-assembly of the ZnO nanoparticles was developed on large area Si wafers with techniques compatible with the standard CMOS processing technology. Photolithographic



patterning of the ZnO nanoparticles in copolymer on Si substrate was developed to be compatible with the copolymer systems. Contact metal deposition with standard lift-off process on the ZnO-nanocomposite film was performed. Functionalization of ZnO nanoparticles on Si substrates provides the advantage of monolithic integration with CMOS peripheral circuitry.

- **Characterization of ZnO-nanocomposite on p-(100) Si substrate** – ZnO nanoparticles of wurtzite crystal structure was developed on (100) Si substrate with orientation as that of the Si substrate, indicating a pseudo-epitaxial structure of the nanoparticles. Quantum confinement effects were observed from room temperature photoluminescence of smaller ZnO nanoparticles.
- **Development of novel ZnO-nanocomposite/Si n-p heterojunction diode** – ZnO-nanocomposite/p-Si heterojunction n-p diodes were developed for the first time. Current-voltage measurement showed rectifying n-p heterojunction diode properties. Capacitance-voltage measurements showed the formation of abrupt ZnO-nanocomposite/p-Si heterojunction diodes.
- **Development of novel high performance ZnO hydrogen gas nanosensor** - A novel hydrogen gas nanosensor based on ZnO-nanocomposite/Si heterojunction diode was developed for high sensitivity, rapid, room temperature sensing. The dependence of nano-sensor sensitivity and response-recovery times on size and density of the ZnO nanoparticles, applied bias and gas concentration was studied.

## 1.2 BACKGROUND

### 1.2.1 Semiconductor Nanoparticle Properties

The last few decades have shown a tremendous increase in the research of semiconductor nanoparticles following the pioneering works of Efros and Efros [26], and Brus [27] on the study of quantum-size effects in these particles. Experimental studies showed the enormous range of physical properties affordable by size tuning the semiconductor nanoparticles of sizes below 100nm. For example, in the prototypical material, CdS, the band gap can be tuned from 2.5 eV to 4 eV [28], the melting temperature varies from 1600 C to 400 C [29], and the pressure required to induce transformation from a four- to a six-coordinate phase increase from 2 to 9 GPa [30]. All these variations in the fundamental properties of CdS were achieved by reducing the size of the crystal, not altering the chemical composition. The two major factors that play an important role in altering the fundamental properties of semiconductor nanoparticles are – 1) the quantum size effects, i.e. the effects of quantum confinement of the charge carriers in the material and 2) the large surface-to-volume ratio of the nanoparticle compared to its bulk counterpart.

The most direct consequence of the quantum confinement effects on semiconductor nanoparticles is the widening of the energy band gap. This change in the electronic structure causes pronounced changes in the optical properties of the nanoparticle as compared to the corresponding bulk semiconductor. Changes in the electrical and optical properties are also observed as result of systematic transformation in the density of electronic energy levels as a function of the size of

## CHAPTER 1: INTRODUCTION

the particles. Qualitatively, it can be understood as a particle in a box problem, where the energy levels become discrete as the box dimensions are reduced due to quantum confinement. This simple idea gives a picture for qualitative understanding of the increase in the band gap with decrease in particle size. Several approaches have been used for quantitative understanding of these effects. The mostly used approaches are the effective mass approximation (EMA) method [26, 27, 31, 32], empirical pseudopotential method [33] and the tight binding approach (TBA) [34, 35]. The energy band gaps calculated using the EMA approach has been found to agree with the experimental data results for larger nanoparticles, but are usually overestimated for smaller particles.

While there are several ways to quantitatively understand the quantum-size phenomenon of the semiconductor nanoparticles from a theoretical standpoint, the experimental determination of the band gap variation as a function size is mostly performed by ultraviolet-visible absorption spectroscopy, with the absorption threshold corresponding to the direct band gap in the material. Significant blue shift of the absorption edge in the absorption spectra has been observed as the particle size is reduced [36]. An important contributor to the spectroscopy of semiconductor is the presence of weakly bound excitons called Mott-Wannier excitons. The existence of the exciton has a strong influence on the optical absorption properties of the material. The photon induced transitions between the hydrogen atom like system of energy levels of the excitons produce a series of absorptions peaks in the spectra. Due to quantum confinement in semiconductor nanoparticles, these excitonic absorption features have been found also to blue shift toward higher energies with decrease in

## CHAPTER 1: INTRODUCTION

particle size [36]. This blue shift is observed when the size of the nanoparticle becomes comparable to the exciton Bohr radius and is due to the enhanced spatial overlap of the electron and hole wavefunctions with restricted translation motion of the exciton in the decreasing particle size. As a result the electron-hole interaction is enhanced and the exciton binding energy is increased. The increase in the exciton binding energy of nanoparticles has also made it possible to observe the excitonic absorption peaks at room temperature. However in the case of nanoparticles with size much smaller than the exciton Bohr radius, the motion of the electron and hole become independent and the exciton does not exist [31].

The larger percentage of atoms located at the surface of nanoparticles makes a more distinct contribution to the optical properties compared to their corresponding bulk semiconductor. A surface is a strong perturbation to any lattice, creating many dangling bonds. These unsaturated dangling bonds of the nanoparticles are energetically unfavorable and create a high concentration of deep or shallow energy levels within the band gap. These surface states act as electron hole recombination centers, causing non-radiative transitions of electrons and holes prior to the radiative recombination, thus causing emissions to occur at lower energies than the band gap energy of the nanoparticles. Due to the larger contribution of the surface atoms in nanoparticles, degradation of the optical properties is more pronounced in nanoparticles than in bulk semiconductors. Passivation techniques have been adopted to improve the properties by bonding the surface atoms with another material of a much larger band gap [37, 38].

## CHAPTER 1: INTRODUCTION

The surface atoms also play a key role in altering the thermodynamic properties of semiconductor nanoparticles from their bulk properties, like the decrease in solid to liquid transition temperature observed with decreasing nanoparticle size [39, 40, 41]. This change can be understood by taking into account the fact that a large fraction of the total atoms in a nanoparticle are located at the surface and a large energy is associated with these surface atoms. Since melting is believed to start at the surface and reduces the total surface energy present in the solid phase, the smaller the nanoparticle, the larger the contribution made by the surface energy to the overall energy of the system, the more dramatic the melting temperature reduction. Similarly the pressure required to induce solid-solid transformations in nanoparticles have been found to differ from that required by their corresponding bulk semiconductors [42].

These are only some of the striking properties of semiconductor nanoparticles. From these it can be understood why the advances in the science of semiconductor nanoparticles show no sign of abating. Steady improvement in the range of materials which can be prepared as nanoparticles are expected in the future. At the same time the currently developed semiconductor nanoparticles are of sufficient quality to enable a new generation of experiments to functionalize and integrate into devices. An important application that has been found for the size dependent optical properties of the nanoparticles is in LEDs and photodetectors, where one type of semiconductor can be used to produce a whole spectrum of visible light simply by changing the particle diameter. Another promising area of application being researched for these particles with their large surface-to-volume ratio is in sensors.

### 1.2.2 Material Properties of ZnO

Zinc oxide has a hexagonal wurtzite structure and the lattice constants of ZnO hexagonal unit cell are  $a=b=3.249 \text{ \AA}$  and  $c=5.206 \text{ \AA}$  [43]. ZnO has strong piezoelectric properties as a consequence of the lack of symmetry in the ZnO crystal structure along c-axis with piezoelectric coefficient ( $e_{31}$ ) of  $0.43 \text{ C/m}^2$  [44] and large electromechanical coupling coefficients of 5% on sapphire substrates [45]. The exciton binding energy of ZnO is 60 meV [46] as compared to that of GaN which is 25 meV. This energy value is an indicator of radiative recombination efficiency of photogenerated carriers which seems to improve for ZnO and thus indicates ZnO to be a possible alternative to GaN in optoelectronic devices. ZnO has a band gap of 3.3 eV and as a result allows over 80% transmission in the visible and near infrared wavelength range. This property of ZnO has found application as transparent conductive contact in optoelectronics [47]. This band gap can be increased by reducing the size of the ZnO material to the nanometer regime which allows transmission in the UV range as reported in literature and in our work. ZnO is a non-stoichiometric compound and an n-type semiconductor due to intrinsic point defects [43]. The point defects in ZnO can be zinc interstitials or oxygen vacancies [43]. However, there is still debate about whether zinc interstitial or oxygen vacancy is the dominant defect.

### 1.3 OUTLINE OF THESIS

This chapter introduces the goals of our research and presents the contributions of our work. The novel properties of semiconductor nanoparticles have been discussed. The important properties of ZnO material have been presented.

Chapter 2 reports the development of a novel procedure for the self-assembly of ZnO nanostructures on large area Si substrates using diblock copolymers. Background on diblock copolymers and their intrinsic nature to form nanoscale domains in a polymer matrix have been provided. The domains of copolymers have been used as templates for the self-assembly of ZnO nanoparticles. Review of other self-assembly processes and their limitations have been reported.

Chapter 3 presents the evaluation of the self-assembly of ZnO nanostructures on Si substrates. Fourier transform infrared spectroscopy was used to examine the metal precursor association to the minority blocks, X-ray photoelectron spectroscopy confirmed the conversion to ZnO from precursor and microscopy tools were used to verify the spherical morphology of the developed nanoparticles.

Chapter 4 discusses the characteristics of the ZnO nanoparticles. The size and density of the nanoparticles in different copolymers were evaluated with AFM. The correlation between the physical parameters of the nanoparticles and diblock copolymer was developed. XRD studies were performed on the nanoparticles to determine the crystal structure and orientation of the nanoparticles on (100) Si substrate. Photoluminescence studies of two different sizes of ZnO nanoparticle performed at room temperature are reported and discussed.

## CHAPTER 1: INTRODUCTION

Chapter 5 presents the development of novel ZnO-nanocomposite/Si n-p heterojunction diodes and the studies of the electrical and transport properties of these heterostructures. Current-voltage and capacitance-voltage measurements were performed in order to evaluate the devices. These nano-diode heterojunctions showed rectifying properties with good rectification ratio and small leakage currents.

Chapter 6 presents the development of a high performance nano gas sensor with ZnO-nanocomposite/Si n-p heterojunction diodes. A sensitive and a fast responsive nano gas sensor has been developed by employing high surface area of the developed ZnO nanoparticles along with metal catalyst and introducing the added benefit of field-assisted gas sensing. The dependence of sensor sensitivity and response-recovery times on size and density of ZnO nanoparticles, applied bias and gas concentration was studied.

Chapter 7 summarizes the results of this thesis and proposes some future areas of research.



## **CHAPTER 2**

# **SELF-ASSEMBLY OF NANOSTRUCTURES IN DIBLOCK COPOLYMERS**

This chapter presents a background of self-assembly through copolymers synthesis and our novel procedure developed for the self-assembly of ZnO nanostructures on large area Si substrates using diblock copolymers. The intrinsic nature of diblock copolymers to form nanoscale domains in a polymer matrix was used to template the ZnO nanostructures on Si. Diblock copolymers with spherical domains were used to obtain ZnO nanostructures of spherical morphology.

## **2.1 BACKGROUND**

### **2.1.1 Block Copolymers**

Polymers are macromolecules composed of a large number of repeated molecular units termed monomers which are covalently bonded to each other. Copolymers are hybrid polymers composed of chemically distinct monomers, linked together to form a single macromolecule. Depending on the arrangement of the monomers within the polymer molecule, the copolymers can be classified as alternating, block, random and graft copolymers. Fig. 2-1 shows the schematic of the various categories of copolymer, where A and B are two chemically distinct monomers. The copolymers exhibit properties which are largely dependent on the arrangement and interaction between the different polymers in the copolymer. Some

of the properties exhibited by the copolymers are characteristics of the individual polymer blocks but some properties are novel to both the polymer blocks. One such novel property is the formation of microdomains in diblock copolymers.

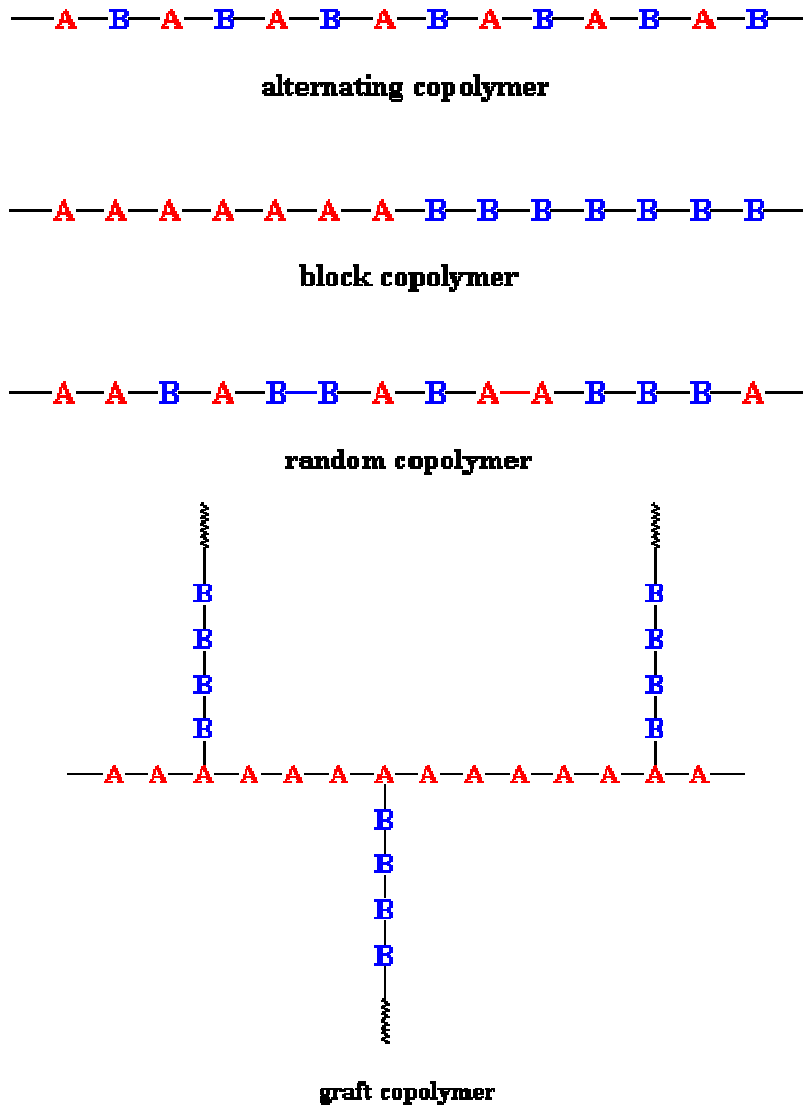


**Figure 2-1. Schematic of different classes of copolymers depending on the arrangement of chemically distinct polymer blocks or monomers**

## CHAPTER 2: SELF-ASSEMBLY OF NANOSTRUCTURES

Block copolymers (fig. 2-1) are comprised of repeated sequence of two or more chemically distinct homopolymer segments covalently bonded to form a single polymer chain. Homopolymers are polymers made up of a single type of monomer and each homopolymer segment in a copolymer is termed as a block. Depending on the number of chemically distinct blocks present in a copolymer, the copolymer is termed as diblock, triblock, tetrablock, multiblock, etc.

Diblock copolymers are made of two chemically distinct blocks. Fig. 2-2 shows a schematic of a diblock copolymer with block A bonded to block B. The block with the larger number of repeat units (monomers) is termed as the majority block (block A) and that with the smaller number of repeat units is the minority block (block B) of the copolymer. These blocks of homopolymers are immiscible in each other. Due to this immiscibility of the two blocks of the diblock copolymers, thermodynamics drive the blocks to phase separate in the solid phase. However, the covalent bonding between the blocks prevents them from macrophase separation i.e. form pure phases of block A and block B. As an alternative route to reach equilibrium state, the minority blocks of the diblock copolymer self-assemble to form domains in the matrix of the majority block (fig. 2-3). This process of phase separation is termed as microphase separation and the domains are termed as microdomains even though the characteristic lengths of these domains are in the nanometer regime. Depending on the volume fraction of each block, the morphologies of the microdomains ranges from spherical, cylindrical, bi-continuous and lamellar [48] as shown in fig. 2-4.

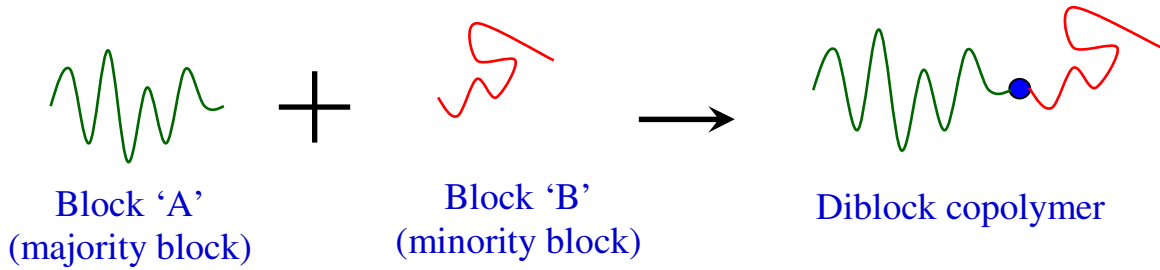


**Figure. 2-2. Diblock copolymer composed of a majority block polymer and a minority block polymer covalently bonded and chemically distinct to each other**

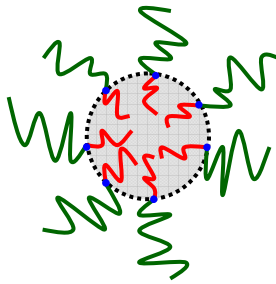


**Figure 2-3. Schematic of a microdomain formed after phase separation between the majority and the minority blocks of diblock copolymer in solid phase.**

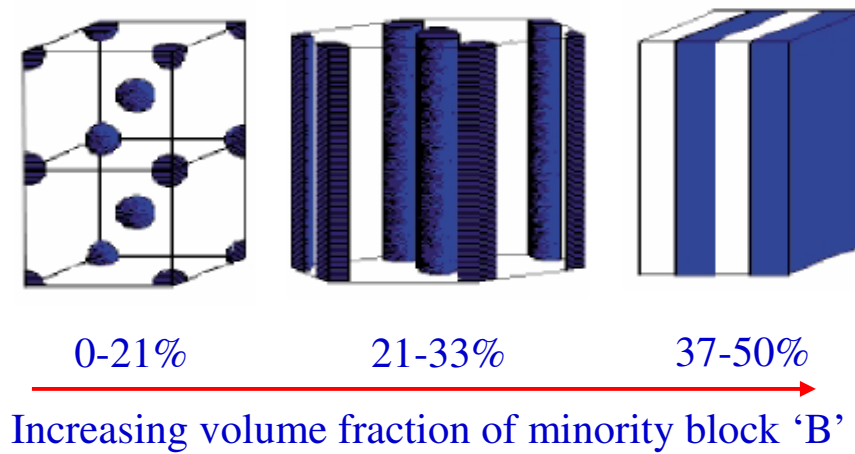


**Figure 2-4. Morphologies of the microdomains formed by minority blocks in the matrix of majority blocks of the block copolymer**

Besides controlling the morphologies of the domains, the domain sizes can also be tuned by adjusting the molecular block lengths and the block repeat unit ratios. These domains of diblock copolymers have been used to develop novel economical lithography techniques [49, 50]. These domain features of the diblock copolymers make them the ideal chemical templates for the synthesis of nanostructures.

### **2.1.2 Nanoparticle synthesis through diblock copolymer self-assembly**

There has been considerable interest in the in situ production of semiconductor nanoparticles confined within the nano-sized spherical domains of block copolymers. This approach offers advantage over other chemical techniques of nanoparticle synthesis by eliminating the preliminary steps required to synthesize, stabilize, and store the clusters, and the complicated steps required to make nanocomposite films. The polymer matrix also provides kinetic hindrance to the aggregation of the particles in this process. Over the past decade different techniques of incorporating the inorganic material into the domains have been developed by several research groups.

Early works by Cohen research group in the formation of semiconductor nanoparticles using diblock copolymers involved the synthesis of organometallic monomers [51, 52, 53, 54, 55]. These monomers were used as one of the blocks of the diblock copolymer, producing microphase separated domains containing pre-specified and nearly identical concentrations of metal precursors. Subsequent chemical treatment of these metal containing domains precipitated semiconductor

## CHAPTER 2: SELF-ASSEMBLY OF NANOSTRUCTURES

nanoparticles within the domains. However the drawbacks of this scheme are the difficult monomer synthesis and the need of different monomers for different type of nanoparticles.

A more general methodology was developed with the intent of using one diblock copolymer system for the synthesis of a range of nanoparticles [56]. In this scheme the metal precursor was sequestered into preformed microphase separated block copolymer domains that contained reactive metal-binding moieties instead of incorporating into the monomer. Yue et al [56] developed a metal loading technique that made use of the carboxylic acid functionalities in minority blocks of the diblock copolymer as the metal-sequestering groups. Metal loading into the domains occurred via ion exchange between the carboxylic anions and the desired metal cations during the treatment of the microphase separated diblock copolymer with aqueous metal salt solution [57] or with vapor of metal-alkyl compounds [58]. The desired nanoparticles were then precipitated within the microdomains by reduction or sulfidation of the metals complexes. A modification to the generalized loading scheme via aqueous metal salt solution developed by Yue et al was introduced by Clay et al [59]. A pretreatment of the diblock copolymer containing the carboxylic acid functionality was done with NaOH solution to improve the metal ion uptake from the aqueous metal salt solution into the microdomains. The enhancement in metal loading is attributed to the fact that  $\text{Na}^+$  cations more readily dissociate from the carboxylate anions than  $\text{H}^+$  and as a result the uptake of metal into the microdomains is facilitated. However such methodologies via aqueous salt solution or vapor of metal alkyl compound are constrained by diffusion limitations of the metal ions.

Despite these constraints, the use of diblock copolymers has been successful in developing good enough quality semiconductor nanoparticles to encourage further research in this area.

### **2.2 DEVELOPMENT OF SELF-ASSEMBLY OF ZnO NANOPARTICLES FOR LARGE AREA APPLICATIONS**

The spherical microdomains of diblock copolymers were used as a templating medium for the development of ZnO nanoparticles on large area Si substrates. The diblock copolymers with their intrinsic nature to form nanoscale domains within a polymer matrix make ideal candidates for the synthesis of ZnO nanoparticles. This allows the use of capping agents to be avoided as the polymer matrix provides kinetic hindrance to the aggregation of self-assembled ZnO nanoparticles. The application of capping agents in the synthesis of ZnO nanoparticles is not favorable as it reduces the surface reactivity of the nanoparticles for sensor application. The use of diblock copolymers also allows easier manipulation of nanoparticle shape, size, and density. In addition, photoresist equivalent spin-cast application for delivery of nanoparticles over large area wafers was possible with this approach of synthesis. This enabled us to develop a novel inexpensive mass fabrication technique for the delivery of ZnO nanoparticles on substrates at room temperature. This is a faster and less complicated technique than top-down approaches like optical lithography and focused ion beam lithography and fabrication by physical methods like pulsed laser deposition, metalorganic chemical vapor deposition and reactive electron beam evaporation. This

## CHAPTER 2: SELF-ASSEMBLY OF NANOSTRUCTURES

process was developed to be compatible with the standard CMOS device processing techniques in the semiconductor industry.

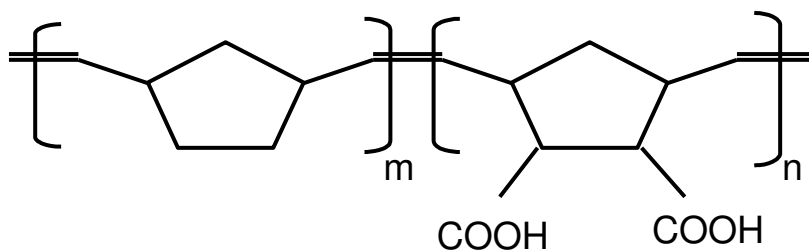
The basic steps involved in the procedure developed for the self-assembly of ZnO nanoparticles on Si wafers are the introduction of a metal salt precursor to the minority blocks of the copolymer in liquid phase at room temperature, followed by the application of the precursor-doped copolymer solution on large area Si wafers by means of spin-casting and subsequently, the conversion of the self-assembled precursor in the microdomains to ZnO. To aid in the attachment of the precursor to the minority blocks, the diblock copolymers were used with carboxylic acid functional group in the minority blocks. The templating process in our work is markedly different from the previous works mentioned earlier. In our process, the precursor is introduced while the copolymer is in solution, before the microphase separation of the copolymer blocks. This process has the advantage of rapid diffusion and attachment of the metal to the minority blocks as both are in liquid state.



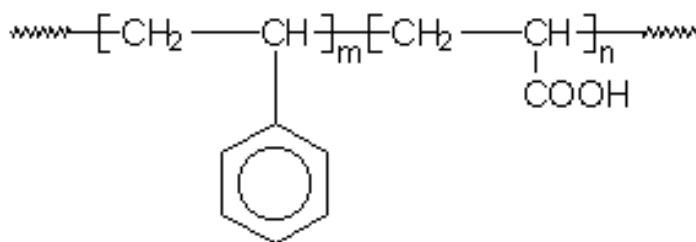
### 2.3 DIBLOCK COPOLYMERS USED IN OUR WORK

The different diblock copolymers used in our work to study the self-assembly of ZnO nanoparticles are poly-norbornene-norbornene-dicarboxylic acid ( $[\text{PNOR}]_m/[\text{PNORCOOH}]_n$ ), poly-styrene-acrylic acid ( $[\text{PS}]_m/[\text{PAA}]_n$ ), and poly-styrene-methacrylic acid ( $[\text{PS}]_m/[\text{PMAA}]_n$ ). Fig. 2-5 shows the chemical structures of these diblock copolymers. The 'm' denotes the molecular block length of the majority block and 'n' is the molecular block length of the minority block. The acid blocks in all the copolymer systems are the minority blocks to which the metal precursor is to be attached and the matrix providing the mechanical stability to the nanoparticles is formed by the majority blocks.

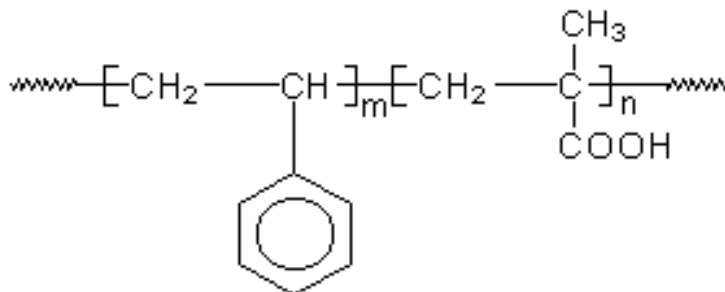
For the self-assembly of ZnO nanoparticles in our work, the diblock copolymers were selected with spherical microdomains as predicted from the volume fraction of the blocks and the block repeat unit ratios. The poly-norbornene-norbornene-dicarboxylic acid copolymer was prepared by Dr Kofinas' group at University of Maryland, College Park and the other two copolymers were purchased from Polymer Source Incorporated. The  $[\text{PNOR}]_m/[\text{PNORCOOH}]_n$  was used with block repeat unit ratio, m/n of 450/50, the  $[\text{PS}]_m/[\text{PAA}]_n$  with four different ratios, m/n of 159/63, 139/17, 106/17 and 106/4, and the  $[\text{PS}]_m/[\text{PMAA}]_n$  with m/n of 318/78. The four different ratios of  $[\text{PS}]_m/[\text{PAA}]_n$  was to study the size and density dependence of the ZnO nanoparticles on the copolymer block lengths which will be discussed in chapter 4.



**[NOR]<sub>m</sub>/[NORCOOH]<sub>n</sub> (polynorbornene-norbornene carboxylic acid)**



**[PS]<sub>m</sub>/[PAA]<sub>n</sub> (polystyrene-acrylic acid)**



**[PS]<sub>m</sub>/[PMAA]<sub>n</sub> (polystyrene-methacrylic acid)**

**Figure 2-5. Chemical structures of the diblock copolymers used in our work.**

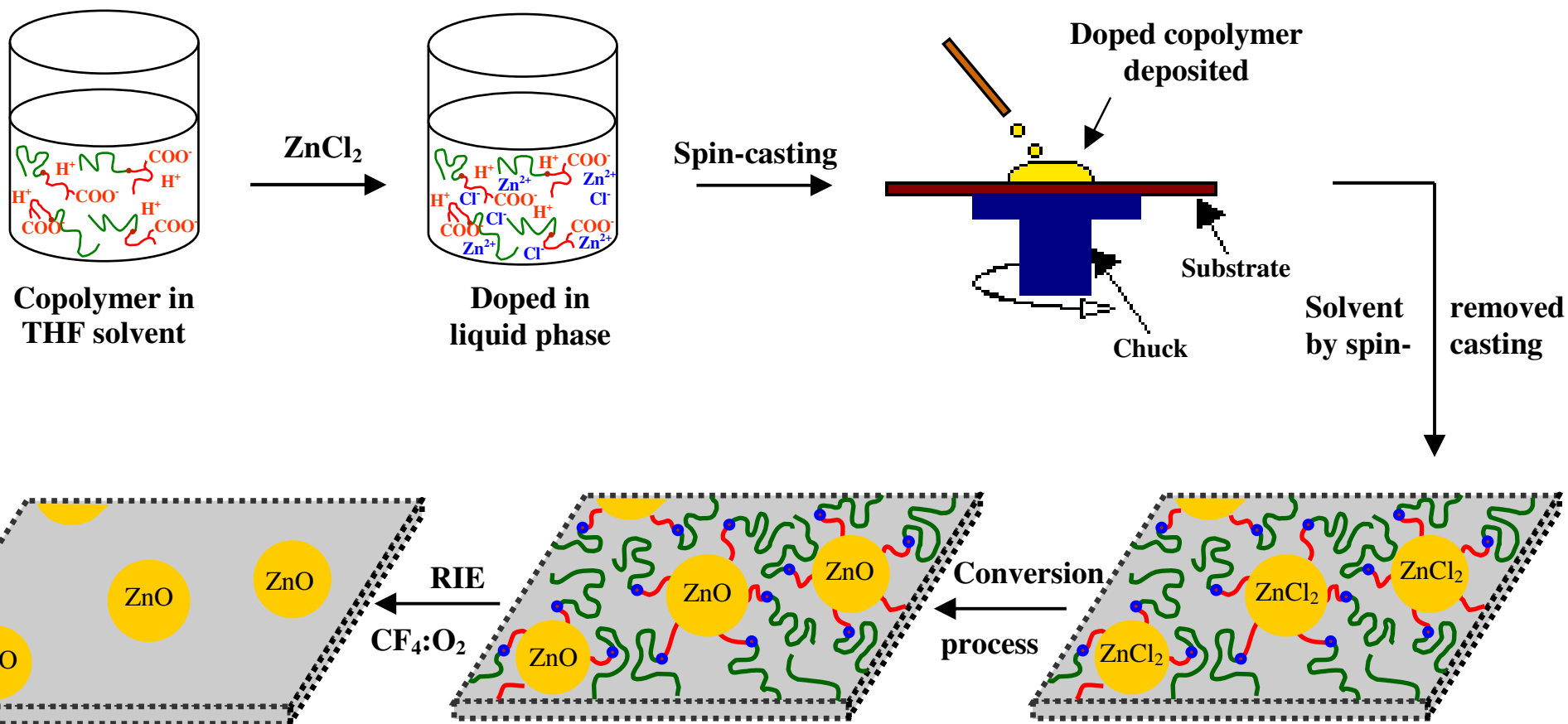


Figure 2-6. Schematic of the synthesis process of ZnO nanoparticles via self-assembly in diblock copolymer.

## 2.4 EXPERIMENTAL PROCEDURE

Fig. 2-6 shows a schematic of the process steps involved in the self-assembly of ZnO nanoparticles on large area substrates.

***Copolymer Doped in Solution*** - The first step of the synthesis process involved the preparation of the doped copolymer in solution. The solvent for the copolymer solution was selected such that it was favorable for both the copolymer and the metal salt precursor. The solution was made by dissolving the copolymers in anhydrous tetrahydrofuran (THF) solvent to make a 1% solution. This was followed by doping of the copolymer solution with ZnCl<sub>2</sub> precursor at room temperature. The dopant precursor used was a 0.5M ZnCl<sub>2</sub> solution in THF bought from Sigma-Aldrich Inc. The precursor was added in solution form for faster interaction of the metal with the acid blocks of the copolymer. The Zn<sup>2+</sup> ions of the precursor associate with the carboxyl radical of the minority blocks of the copolymer. Stoichiometric doping amounts were used for saturation of the carboxyl radicals with the Zn<sup>2+</sup> cations. The doped copolymer solution was left to stir for several hours to assure the maximum association of the metal ions with the carboxyl radicals. The metal association to the carboxyl radical of the minority block was confirmed with Fourier Transform Infrared Spectroscopy (FTIR), as will be discussed in chapter 3.

***Precursor-Copolymer Nanocomposite Film*** - The doping step was followed by the application of the doped copolymer solution onto the Si surfaces. The Si wafers used in this study were 100 mm diameter p-type wafers with surface

## CHAPTER 2: SELF-ASSEMBLY OF NANOSTRUCTURES

orientation of (100), and a resistivity of 14-22  $\Omega$ -cm. The wafers were degreased in solvents and then etched in a 10% HF solution to remove the native oxide from the surface prior to copolymer application. Copolymer application can be accomplished either by static casting directly on the Si surface or by spin-casting on the surface. However, spin casting provided a more uniform and dry film in a fraction of the time needed for static casting to solidify the films. As no data exist on spin casting of these copolymers on Si surfaces, a study was performed to examine best conditions for spin casting for our application in Si technology. Our study showed that an optimal film morphology can be achieved by spin casting the copolymer at relatively low speeds (700 rpm) and for longer time (2 min) as compared with standard photoresist processing. These are the conditions of spin casting under which samples were processed in our work. Spin-casting is a standard technique used in the semiconductor industry for depositing thin films on flat substrates and has been used for many years in photolithography. The procedure involves covering of a flat substrate with a solution which is the doped copolymer solution in our case and then rotating the substrate at an angular speed depending on the thickness of film required. Excess material is blown off the substrate by the centrifugal force, leaving behind a uniform layer of material. Since the solvent THF is highly volatile, it evaporates rapidly during the spin-casting, leaving a thin layer of nanocomposite film on the substrate. On solvent evaporation, microphase separation occurs of the blocks with  $\text{ZnCl}_2$  nanoparticles confined within the domains of the minority blocks of the copolymer within the matrix of the majority blocks and the carboxyl groups regenerated to their acid form.

*ZnO-Copolymer nanocomposite Film* – Spin-casting was followed by the conversion of the  $\text{ZnCl}_2$  precursor to  $\text{ZnO}$ . Two conversion techniques were developed and compared to determine the most effective method. Both the methods developed were compatible with Si processing technology. A wet chemical process using a weak base ( $\text{NH}_4\text{OH}$ ) solution and a dry process using ozone were developed.

For the wet chemical process, the base was diluted to pH 12 before treating the nanocomposite film in the base solution. The base was diluted to slow down the reaction of  $\text{ZnO}$  with the base once it was converted as  $\text{ZnO}$  is an amphoteric oxide which reacts with both acid and base. The nanocomposite film was treated for 24 hrs and then washed in  $\text{H}_2\text{O}$  to remove water-soluble salts and to decompose unstable zinc hydroxides to  $\text{ZnO}$ .

The ozone process was developed using an ultra violet ozone cleaning system (UVOCS). This system consists of a chamber in atmospheric pressure fitted with low-pressure quartz-mercury vapor lamp that generates UV emissions in the 185-254 nm range. Ozone and atomic oxygen are generated when the atmospheric oxygen reacts with the UV light. The UVOCS is also connected to an exhaust system that ensures a clean and controlled environment for the process by the continuous venting of the chamber. For the dry conversion process, the sample was placed in the chamber for ozone exposure times between 1 and 2 hrs depending on the exhaust flow in the chamber. With higher flow the ozone produced in the chamber is vented out of the chamber before complete reaction occurs and as a result, increases the conversion time.

The conversion processes were evaluated with the help of X-ray photoelectron spectroscopy (XPS) as discussed in chapter 3. The dry process was found to be the most effective with substantially shorter treatment times and insignificant loss of ZnO compared to the wet chemical process. The ZnO being an amphoteric oxide, dissolved slightly during the treatment with  $\text{NH}_4\text{OH}$  solution.

*Stand-alone ZnO nanoparticles on Si* – After the conversion process, the copolymer can remain as a metal-oxide (ZnO)-nanocomposite polymer on the Si surface, or the polymer matrix can be removed for stand-alone metal-oxide nanoparticles. The removal of the polymer matrix for stand-alone nanostructures was developed by reactive ion etching.

Reactive ion etching is a process similar to plasma etching, except that it involves bombardment of the surface being etched with accelerated reactive ions. These accelerated ions sputter material off the substrate as they hit its surface, as well as react with the substrate material. Thus, with RIE, etching is accomplished by two processes: sputtering and chemical reaction.

We employed this etching technique to develop stand-alone ZnO nanoparticles on the substrates. The copolymer matrix was reactive ion etched using a  $\text{CF}_4:\text{O}_2$  gas mixture at a ratio of 2:1, with an RF power of 50 watt. Oxygen and carbon tetrafluoride ( $\text{CF}_4$ ), when mixed together for use in plasma etching, create the oxyfluoride ion ( $\text{OF}^-$ ). The oxyfluoride ion is a powerful etching agent for polymeric substances. This ion is particularly adept at cutting the carbon-carbon molecular bonds in the polymer backbone and the reaction with oxygen radicals produces CO,

H<sub>2</sub>O and CO<sub>2</sub>. These reaction products are quickly removed as gases from the vacuum system. ZnO-nanocomposite films casted at 700 rpm were found to require about 30 min of etching for all the copolymer systems.

## **2.5 COMPATIBILITY OF THE SELF-ASSEMBLY PROCESS WITH DEVICE FABRICATION TECHNOLOGY**

The ZnO-nanocomposite films were investigated for compatibility with standard photolithographic patterning using a spin-on photoresist (Shipley 1813) on the nanocomposite film, and metal (Al) deposition by thermal evaporation in vacuum. Standard photoresist processing requires photoresist pre-bake and post-bake cycles at 90 and 120 °C respectively, which will affect the integrity of the copolymer. This is because the glass transition temperature of the matrix polymer is reported to be 105°C. According to literature, heating the polymer above this temperature will result in deformation of the matrix. Thus, in order for the photoresist processing to be compatible with the copolymer systems, a special pre-bake and post-bake cycle was developed that used moderate temperatures (80 °C) and times during photoresist pre-bake and post-bake cycles, to preserve the integrity of the copolymer under higher temperature treatments. Fig. 2-7 shows an optical microscope photograph of the ZnO-nanocomposite film with a spin-on (4500 rpm, 30 sec) Shipley 1813 photoresist film that has been pre-baked at 80 °C, exposed through a photomask, with the pattern developed and post-baked, prior to metal deposition in vacuum and lift-off for metal definition. No “run-off” is observed for the copolymer for the bake temperatures



## CHAPTER 2: SELF-ASSEMBLY OF NANOSTRUCTURES

applied here, and line definition, in this case, was limited by the quality of the mask rather than the copolymer. Standard lift-off techniques for the photoresist were applied to form the metallization pattern successfully. Fig. 2-8 shows an interdigitated pattern after 50 nm of metal (Al) deposition and lift-off with acetone to form the metallization pattern, where finger width of 2  $\mu\text{m}$  and a spacing of 1  $\mu\text{m}$  are observed. The Al metal was deposited by thermal evaporation in vacuum ( $5 \times 10^{-7}$  torr). The photolithographic patterning using Shipley 1813 photoresist, and the metallization of the nanocomposite film on the Si substrates shows promise for selective application of the ZnO nanoparticles on surfaces and also integration of the nanoparticles into CMOS device technologies.

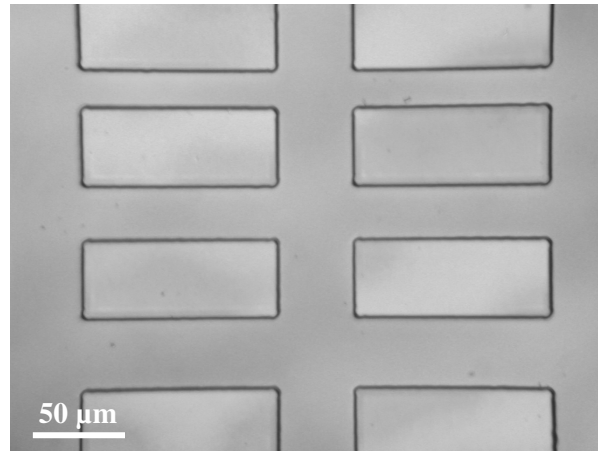


**Figure 2-7. Optical micrograph of photolithographic patterning of the copolymer film on a Si wafer**

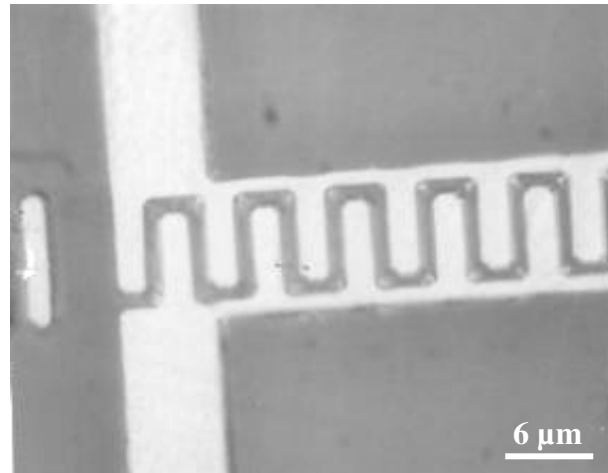


**Figure 2-8. Optical micrograph of interdigitated pattern with Al metallization on copolymer on Si surface.**

## **CHAPTER 3**

# **EVALUATION OF ZnO NANOSTRUCTURE SELF-ASSEMBLY ON Si SURFACES**

This chapter presents confirmation of the self-assembly of ZnO nanostructures on Si substrates. Fourier transform infrared spectroscopy was used to examine the metal precursor association to the minority blocks, X-ray photoelectron spectroscopy was used to confirm the conversion to ZnO and microscopy tools was used to verify the spherical morphology of the developed nanoparticles.

### **3.1 CHARACTERIZATION TECHNIQUES**

#### **3.1.1 Fourier Transform Infrared Spectroscopy (FTIR)**

Fourier Transform Infrared Spectroscopy (FTIR) is a powerful analytic tool for identifying types of chemical bonds (functional groups) based on the absorption of infrared radiation at their characteristic frequencies. Molecular bonds vibrate either by stretching or bending at various frequencies depending on the elements and the type of bonds. The incident infrared radiation is absorbed only when it is of the same frequency as of the characteristic vibrational frequency of the chemical bond. This corresponds to a peak in the spectrum that appears only when the given bond is present. This method is most useful in identifying the formation or destruction of a specific bond with processing.

### 3.1.2 X-ray Photoelectron Spectroscopy (XPS)

X-ray photoelectron spectroscopy is a material characterization technique widely used to investigate the chemical composition of materials. The technique is based on collecting the electrons that are ejected from atoms of the sample being analyzed when irradiated by X-rays. It uses the principle of photoelectric effect. The kinetic energy (K.E) of the emitted electron is equal to the x-ray energy minus the energy with which the electron is bound to the atom [60]. Soft X-rays with energy < 1.5 keV are used to ionize atoms from the core shells of the sample. The energy states of atoms in the valence band region have characteristic ionization energies that reflect perturbations by the surrounding lattice and this environment is proved by the measurement. The X-ray photons do not cause any structural damage to the sample and only those photoelectrons that escape the material without undergoing inelastic scattering are used in the analysis. The technique is non destructive and highly surface sensitive. XPS provides qualitative detection of elements present at concentrations > 0.1% and semi quantitative with 10-20% error, compositional analysis of approximately the top 10nm of material below the studied samples surface. Information about the chemical environment and bonding state of the atoms detected can also be obtained, by means of resolving chemical shifts in the binding energy of the corresponding analyzed photoelectrons. These capabilities alone make the technique a powerful tool for studying the structure and chemistry of the aforementioned self-assembled ZnO nanoparticles.

## 3.2. RESULTS AND DISCUSSIONS

### 3.2.1 Fourier Transform Infrared Spectroscopy (FTIR)

FTIR spectroscopy was employed in our work to monitor the association of  $\text{Zn}^{2+}$  ions of the precursor-dopant with  $\text{COO}^-$  ions of the minority blocks. This association is crucial for the self-assembly of the ZnO nanoparticles on Si. Fig. 3-1 and fig. 3-2 shows the FTIR spectrum obtained for undoped  $[\text{NOR}]_{400}/[\text{NORCOOH}]_{50}$  copolymer film and precursor-doped  $[\text{NOR}]_{400}/[\text{NORCOOH}]_{50}$  copolymer film, respectively. The peak at  $1710\text{ cm}^{-1}$  in fig. 3-1 corresponds to the vibrational frequency known in literature for carbonyl stretch of the carboxylic group [61]. According to [62] this peak disappears and two new peaks at  $1578\text{ cm}^{-1}$  and  $1414\text{ cm}^{-1}$  appear in the spectrum when the carboxylic groups are ionized to carboxylate anions. These new peaks are a result of symmetrical and asymmetrical stretching of the carboxylate anions. In the spectrum for the precursor-doped film (fig. 3-2), another peak appeared at  $1630\text{ cm}^{-1}$  besides the peak  $1710\text{ cm}^{-1}$  for carbonyl group. The appearance of the new peak can be attributed to the attachment of the Zn cation to the carboxylate anion, which altered the stretch of the carbonyl bond, thus verifying the Zn association with the microdomains. The presence of the carbonyl peak at  $1630\text{ cm}^{-1}$  in this spectrum also indicates partial neutralization of the carboxylic functional groups in the doped copolymer solution.

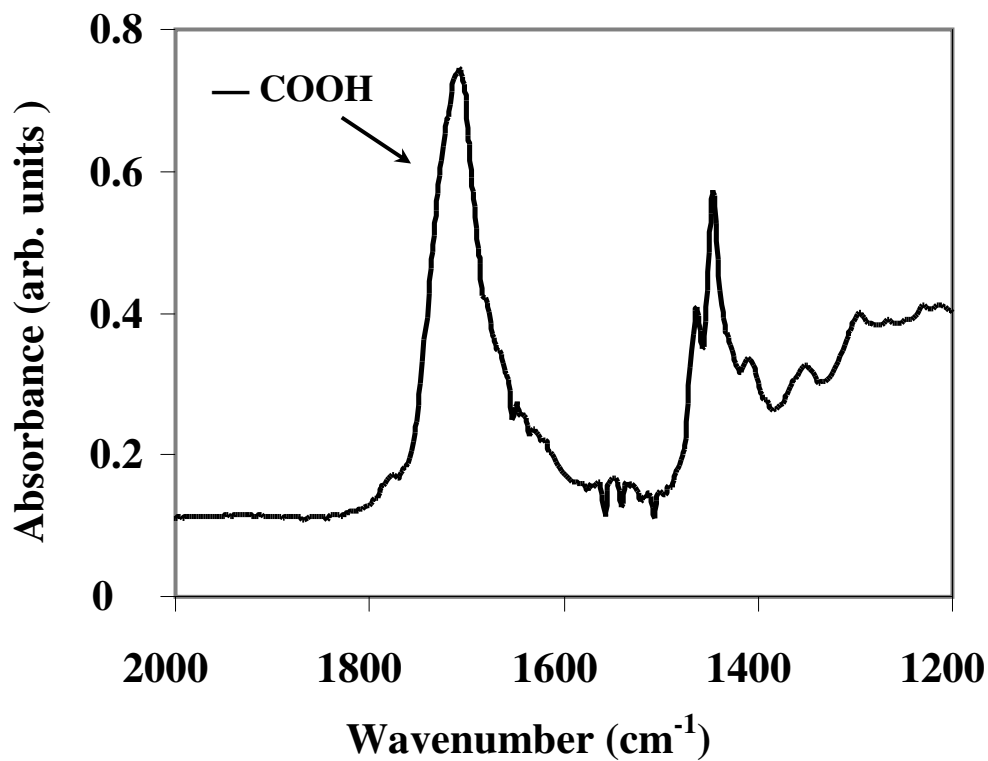


**Figure 3-1. FTIR spectrum of the undoped copolymer. The peak at 1710 cm<sup>-1</sup> is due to the carboxylic group.**

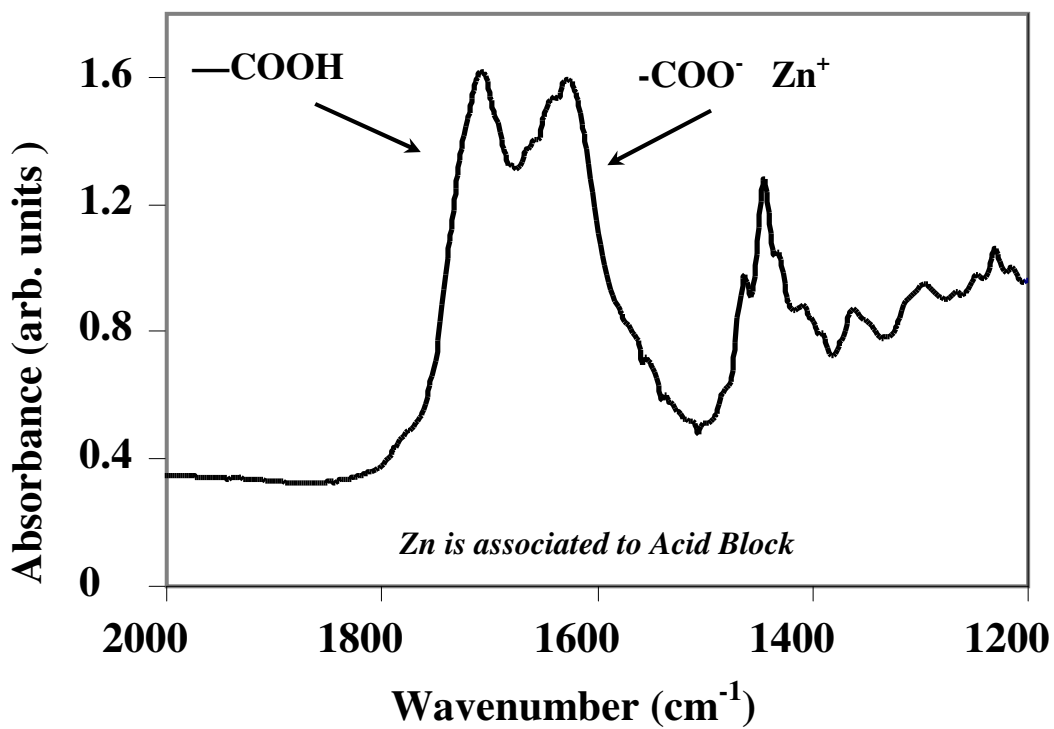


Figure 3-2. FTIR spectrum of the precursor-doped copolymer. The peak at 1630 cm<sup>-1</sup> is due to the Zn-carboxylate. Partial neutralization of the carboxylic also is evident due to the presence of the 1710 cm<sup>-1</sup> peak also.

### 3.2.2 X-ray Photoelectron Spectroscopy (XPS)

X-ray photoelectron spectroscopy (XPS) using a Physical Electronics (PHI 5800) electron spectroscopy for chemical analysis (ESCA) system was employed for the study of the conversion of  $\text{ZnCl}_2$  into ZnO in the microdomains of the copolymer. The energy position of the peaks was calibrated against an elemental carbon peak at 284.8 eV and the concentration of constituents is calculated using peak area and peak height sensitivity factors of every element. Standard Shirley background subtraction is utilized. Probing depth is between 20 and 100 Å depending on material, and elemental sensitivity is around 0.3%.

XPS spectra were obtained for samples before and after chemical treatment to examine the conversion of the precursor to ZnO. The binding energies of electrons in the  $2p_{3/2}$  orbital of Zn atom, in the 1s orbital of O atom and in the 2p orbital of Cl atom were examined to determine the presence of  $\text{ZnCl}_2$  and ZnO in the nanocomposite films developed on Si surfaces. The upper plot of fig. 3-3 shows the XPS spectrum obtained from  $\text{ZnCl}_2$ -[PS]<sub>159</sub>/[PAA]<sub>63</sub> copolymer nanocomposite film on Si before treated under ozone. The lower plot of fig. 3-3 shows the XPS spectrum of the same sample after treatment under ozone exposure. Both the spectra show that peaks are present at binding energies corresponding to the Zn  $2p_{3/2}$  electron binding energies of Zn compounds. However, peak corresponding to the Cl 2p electron binding energy is absent only in the lower spectrum. This indicates the removal of chlorine atoms from the ozone treated nanocomposite film on Si.



To confirm the replacement of the chlorine atoms in  $\text{ZnCl}_2$  by oxygen atoms to form ZnO, the binding energies of the Zn  $2p_{3/2}$  electrons emitted from the sample before and after treatment were examined. Fig. 3-4 shows the high-resolution XPS spectra of the Zn  $2p_{3/2}$  electron binding energy peaks corresponding to the full XPS spectra of fig. 3-3 . It is clearly evident that the binding energy of the Zn  $2p_{3/2}$  electrons shifted from a higher energy of 1023.1 eV to a lower energy of 1021.7 eV in the ozone treated nanocomposite film. These observed energies are in excellent agreement with the characteristic energy values of Zn  $2p_{3/2}$  electrons for  $\text{ZnCl}_2$  (1023.3 eV) and that for ZnO (1021.7 eV) found in the literature [63, 64, 65, 66]. This confirms the formation of the Zn-O bond and as a result conversion of the precursor into ZnO in the  $[\text{PS}]_{159}/[\text{PAA}]_{63}$  copolymer system. Similar evaluations were carried out for all the copolymer systems mentioned earlier and the successful conversion of ZnO was confirmed.

XPS spectra were also obtained to examine the conversion efficiency of the wet chemical technique with  $\text{NH}_4\text{OH}$  solution. These spectra also demonstrated the conversion of ZnO with the absence of Cl 2p peak and the required energy shift of the Zn  $2p_{3/2}$  electrons after  $\text{NH}_4\text{OH}$  treatment. However, in comparison to the spectra for the ozone technique, a significant loss of ZnO was observed in these spectra for the wet chemical process. Fig. 3-5 shows the XPS spectra obtained from two nanocomposite films treated with  $\text{NH}_4\text{OH}$  solution (upper) and ozone (lower), respectively. Comparing the Zn  $2p_{3/2}$  peaks in the two spectra, the loss of ZnO in wet chemical process is evident from the lower intensity of the Zn  $2p_{3/2}$  energy peak.

Thus, the dry conversion method developed with ozone was found to more effective for the self-assembly of the ZnO nanoparticles on Si surfaces.

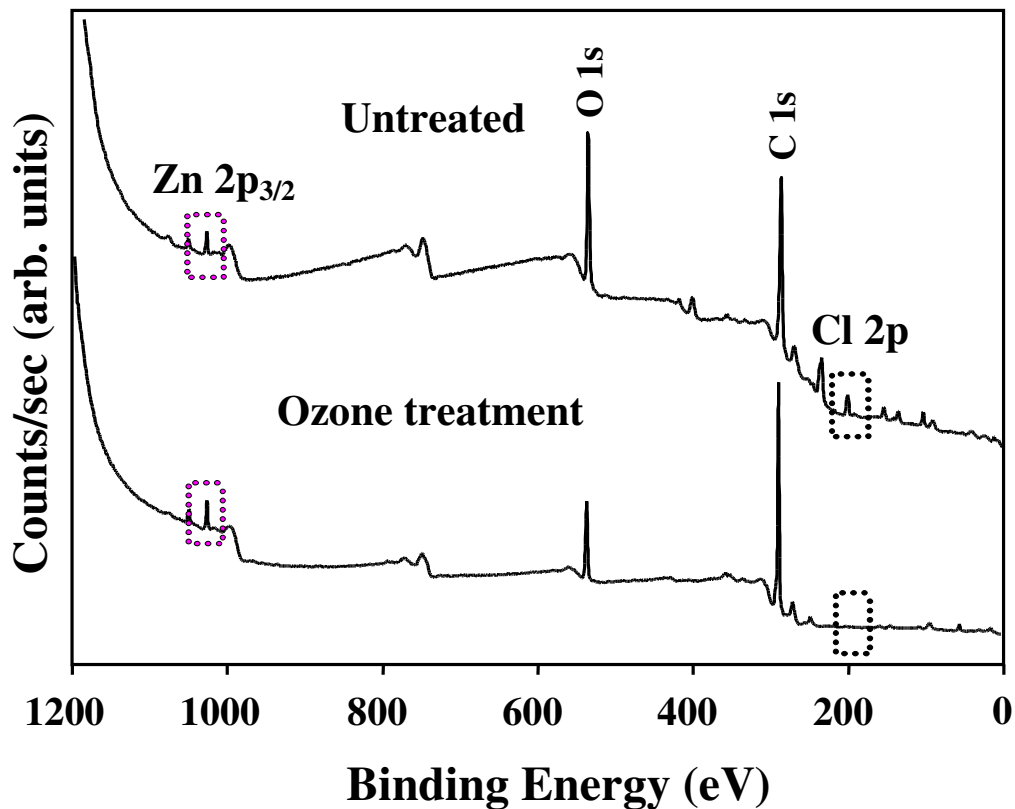
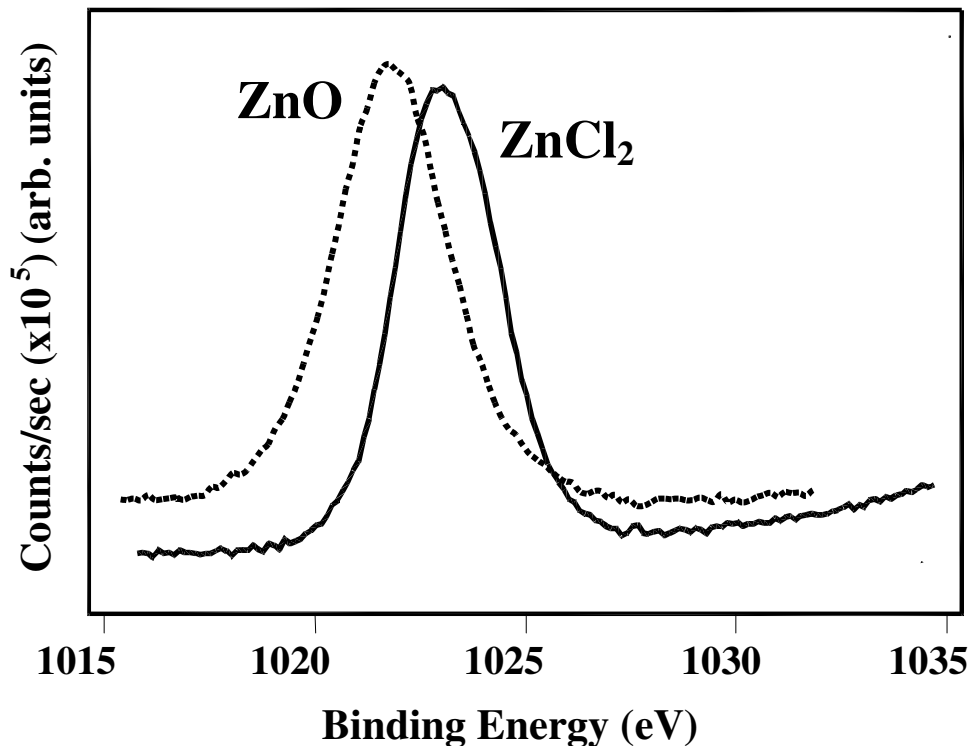


**Figure 3-3. XPS spectra of the ZnCl<sub>2</sub>-[PS]<sub>159</sub>/[PAA]<sub>63</sub> nanocomposite before ozone exposure and the ZnO-[PS]<sub>159</sub>/[PAA]<sub>63</sub> nanocomposite films after ozone exposure spin-cast on (100) Si wafer.**



— Zn 2p<sub>3/2</sub> of **ZnCl<sub>2</sub>**  
 ..... Zn 2p<sub>3/2</sub> of **ZnO** (ozone treatment)

	Lit. B. E. (eV)	Exp. B. E. (eV)
ZnCl <sub>2</sub>	1023.3	1023.1
ZnO	1021.7	1021.7

Figure 3-4. High resolution XPS data of the Zn 2p<sub>3/2</sub> peak for the [PS]<sub>159</sub>/[PAA]<sub>63</sub> copolymer system on Si surface before and after ozone treatment, showing shift in the binding energy of Zn 2p<sub>3/2</sub> electron peak.

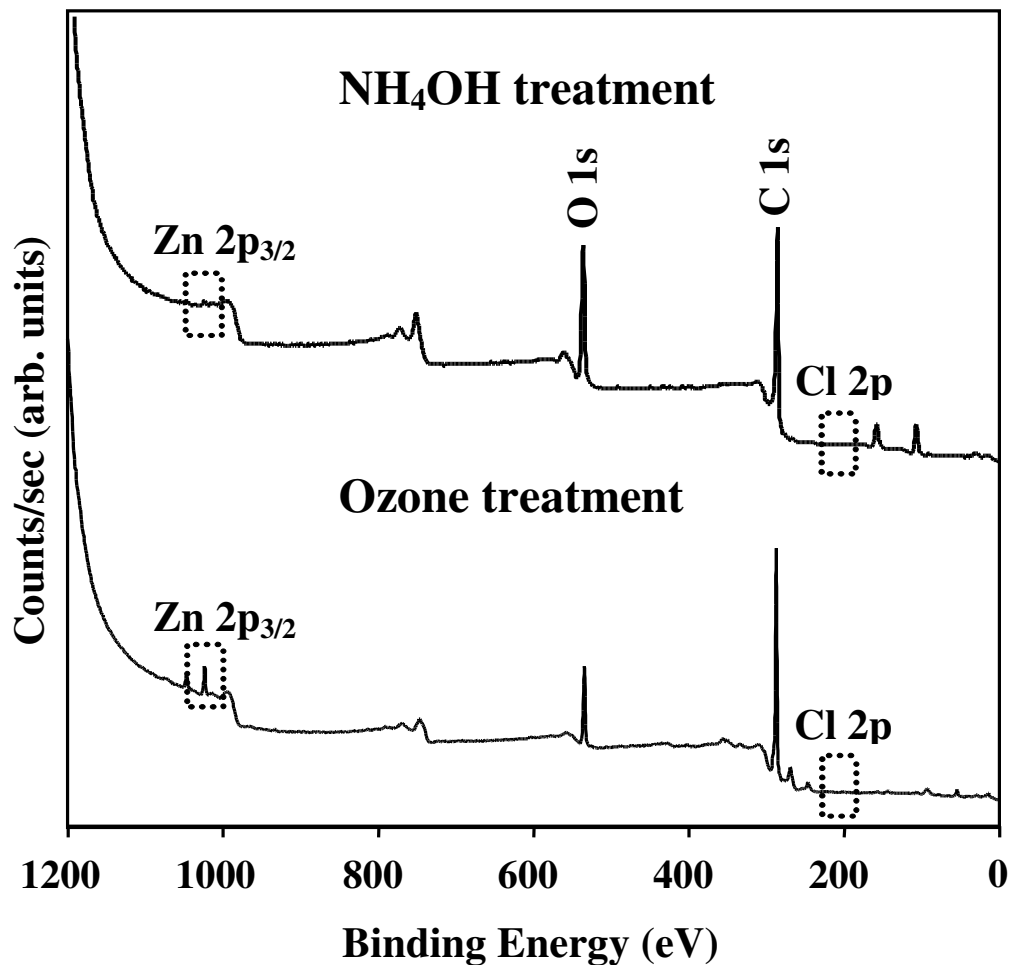
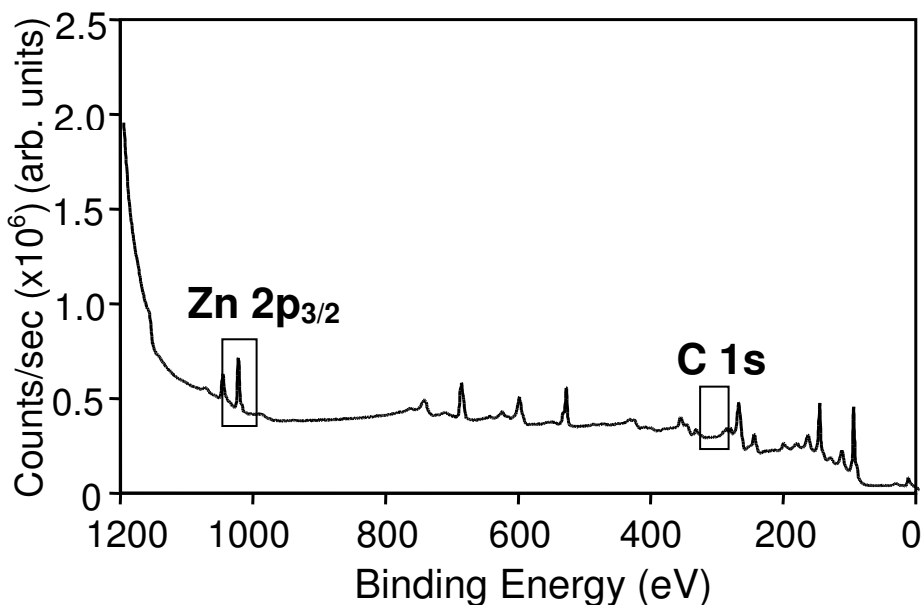


Figure 3-5. Comparison of the wet NH<sub>4</sub>OH and dry ozone treatment methods for the conversion of the precursor to ZnO in the spherical domains of the [PS]<sub>159</sub>/[PAA]<sub>63</sub> copolymer

### 3.2.3 Reactive Ion Etching of the polymer matrix –

The effective removal of the polymer matrices of the ZnO-nanocomposite films on Si surfaces for all copolymer systems was confirmed with XPS by monitoring the C 1s electron binding energy peaks of carbon atoms and Zn 2p<sub>3/2</sub> peaks. Fig. 3-6 shows the spectrum of ZnO-nanocomposite film on Si after RIE. The spectrum shows the presence of the Zn 2p<sub>3/2</sub> peak and the absence of carbon peaks (C 1s) from the copolymer, which were clearly present in large amount in the spectra of the samples prior to reactive ion etching as seen in fig. 3-3. It is evident that under these conditions reactive ion etching effectively removes the polymer matrix from the Si surface without removing the ZnO nanoparticles.

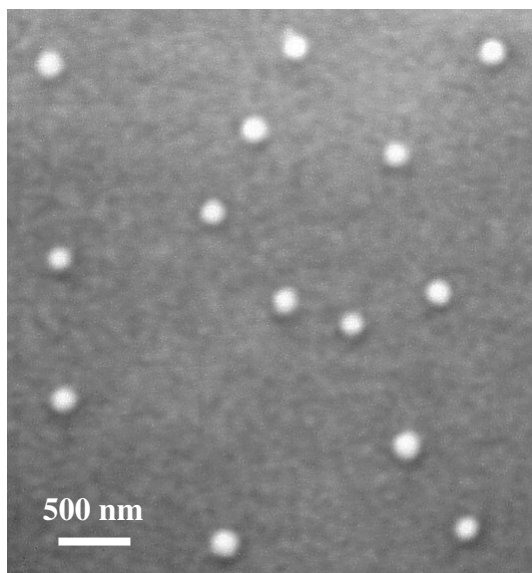


**Figure 3-6. XPS spectrum of ZnO nanoclusters after removal of copolymer matrix from the Si surface by reactive ion etching using a gas mixture of CF<sub>4</sub> and O<sub>2</sub> with a ratio of 2:1 for 1min.**

### 3.2.4 Microscope images of ZnO nanoparticles in diblock copolymer

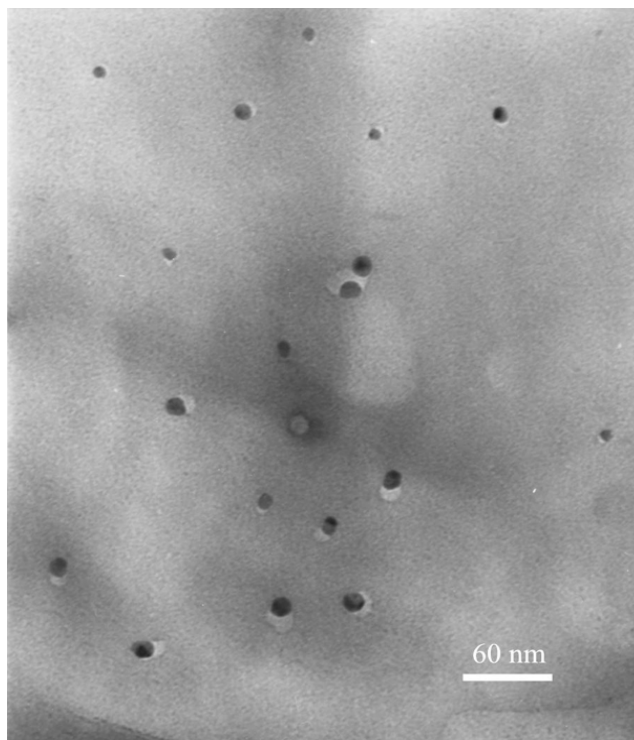
Once conversion of the ZnO nanoparticles was confirmed, microscopy tools were used to examine and confirm the spherical morphology of the ZnO nanostructures as targeted by the selected copolymers with spherical microdomains.

Fig. 3-7 shows a scanning electron micrograph (SEM) of the ZnO-[PS]<sub>159</sub>/[PAA]<sub>63</sub> nanocomposite film on Si surface which shows the spherical morphology of the nanoparticles in this copolymer system. The SEM micrograph is in an area of 6 x 4 μm. The lateral size distribution of the nanoparticles was about 200–300 nm. The average density of the nanoparticles was  $3 \times 10^7/\text{cm}^2$



**Figure 3-7. SEM image of ZnO nanoparticles developed in [PS]<sub>159</sub>/[PAA]<sub>63</sub> copolymer on p(100) Si substrate**

TEM image (fig. 3-8) obtained for the ZnO nanoparticles within the polymer matrix of [NOR]<sub>400</sub>/[NORCOOH]<sub>50</sub> showed spherical morphology as targeted by the choice of copolymer. The size of the nanoparticles obtained with this copolymer was ranged between 7 and 15 nm.



**Figure 3-8. TEM image of ZnO nanoparticles developed in [NOR]<sub>400</sub>/[NORCOOH]<sub>50</sub> copolymer**

### CHAPTER 3: EVALUATION OF ZnO NANOSTRUCTURE SELF-ASSEMBLY

With the polystyrene-methacrylic acid, [PS]<sub>318</sub>/[PMAA]<sub>78</sub>, we also obtained ZnO nanostructures with spherical morphology as shown in fig. 3-9. The nanoparticles were observed to have a lateral size distribution between 100 and 250nm and a height distribution between 50 and 90nm.

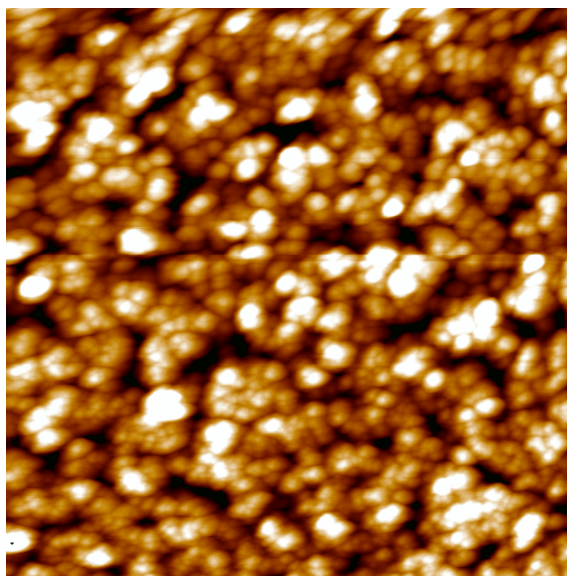


**Figure 3-9. Atomic force micrograph (scan area size of 5x5 $\mu$ m) of the ZnO-[PS]<sub>318</sub>/[PMAA]<sub>78</sub> nanocomposite film on Si surface**



## **CHAPTER 4**

# **MORPHOLOGICAL, STRUCTURAL AND OPTICAL CHARACTERIZATION OF ZnO NANOSTRUCTURES ON Si SURFACES**

This chapter presents the characteristics of the ZnO nanoparticles developed on large area Si wafers using diblock copolymers. The size and density of the nanoparticles in different copolymers were evaluated with AFM. The correlation between the physical parameters of the nanoparticles and diblock copolymer were developed. XRD studies showed wurtzite crystal structure of the ZnO nanoparticles with orientation along the (100) Si substrate. Photoluminescence studies at room temperature of two different sizes of nanoparticles showed quantization effect in the smaller particles.

## **4.1 CHARACTERIZATION TECHNIQUES**

### **4.1.1 Atomic Force Microscopy (AFM)**

Atomic force microscopy (AFM) has been demonstrated to be an invaluable technique for the surface morphological characterization of nanostructures. This technique provides 2-D and 3-D images of the nanostructure surfaces for evaluation. The microscopy uses a tiny cantilever beam with an attached tip to interact with the surface. The deflection of the cantilever due to repulsive electronic interactions between the atoms of the tip end and the specimen is measured to provide an image of

the surface structure. Both contact and tapping mode AFM is possible, the latter employed in case of soft surfaces avoiding contact of the tip with the surface.

#### 4.1.2 X-ray Diffraction Spectroscopy (XRD)

X-ray diffraction (XRD) is a non-destructive tool that helps to determine the crystal structure and crystal orientation of bulk materials, powders, thin films and nanomaterials. In this technique, the sample is irradiated with a beam of X-ray of a single wavelength which produces reflections from the sample to form a diffraction pattern. These reflections are a result of constructive interference between diffracted X-ray waves when scattered by the atoms of the crystal sample. Constructive interference among the waves occur for only those waves that follow the Bragg's law,  $2d \cdot \sin \theta = n\lambda$ , where  $d$  is the inter-plane distance of the crystal lattice,  $\theta$  is the refraction angle and  $\lambda$  is the wavelength of the X-ray. The diffraction pattern is obtained only if the X-ray waves are reflected back from planes or atoms with interplanar or interatomic distance of  $d$  and only in the direction where the path length difference of the diffracted waves is an integer multiple of the X-ray wavelength. Thus the diffraction pattern informs about the atoms or planes that are arranged in a periodic manner in a particular direction to the crystal plane. A reason for using X-ray and not any other radiation is because of its comparable wavelength to the lattice constants of crystals, in the range of (1-100 Å). Other radiations can also produce diffraction patterns when impinged on crystals but not as significant as X-rays.

Fig. 4-1 shows the setup that is used for  $\theta$ - $2\theta$  scan of crystal samples to determine the orientation of the sample with respect to the substrate normal. Lattice constants and structural phases of the thin films can also be derived. The out-of-plane alignment of the film with respect to the substrate is judged by the line width of the  $\omega$ -scan. For determining the out-of-plane orientation of films, the  $2\theta$  value of the selected peak is fixed and the angle  $\theta$  scanned for few degrees. The FWHM value obtained from this gives the degree of orientation of the film.

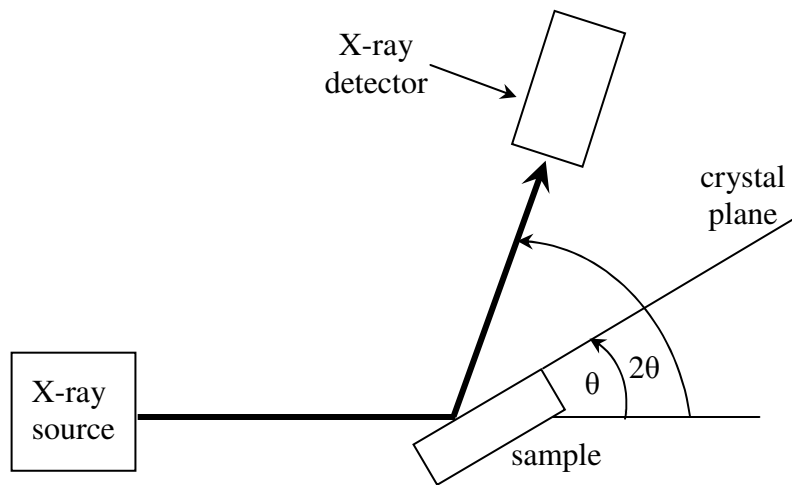


**Figure 4-1. Setup for  $\theta$ - $2\theta$  scan of sample**

### 4.1.3 Photoluminescence (PL) spectroscopy

PL spectroscopy is a contact-less, nondestructive method of probing the electronic structure of materials. A photon whose energy equals or exceeds the energy band gap can excite a valence electron across the energy gap. Absorption occurs when the photon raises an electron from a neutral donor to the conduction band or from the valence band to a neutral acceptor. It is also possible to induce absorptive transitions from the valence band to an ionized donor, or from an ionized acceptor to the conduction band. They also lead to the more sensitive probe of photoluminescence, which occurs when the excited electron returns to its initial state. If the return process is radiative, it emits a photon whose energy gives the difference between the excited and initial state energies. The emission spectrum shows a fingerprint peak related to the energy of each excited level.

The absorption process depends on whether the semiconductor has a direct or an indirect band gap. The energy is conserved during this process according to

$$\hbar\nu = E_f - E_i, \quad \text{for direct band gap transition}$$

$$\hbar\nu = E_f - E_i \pm \hbar\omega, \quad \text{for indirect band gap transition}$$

where  $E_i$  and  $E_f$  are the initial and final state energies respectively and  $\hbar\nu$  is the photon energy. In indirect band gap transitions, the excited electron requires additional momentum to reach the conduction band minimum that is at non-zero wave vector and it gains this energy from a phonon interaction [67].

An electron-hole pair can recombine non-radiatively [68] and the experimental study of these processes is then very difficult because the mechanism

manifests itself only by the absence of a photon. Some non-radiative emission processes include phonon emission, surface recombination and Auger effect. In Auger effect, the energy released by a recombining electron is immediately absorbed by another electron, which then dissipates this energy by emitting photons. This is thus a three body collision process and one that depends on carrier-carrier interaction and becomes more intense as carrier concentration increases. Since the carrier concentration increases with temperature, the Auger effect reduces at lower temperatures. Surface recombination refers to the presence of dangling bonds, which can absorb the recombining electrons. Also a cascade of phonon emissions could occur during recombination. At lower temperatures, lattice vibrations reduce significantly, thus lowering phonon emissions. Thus non-radiative recombination decreases at lower temperatures, increasing the efficiency of the PL measurements. PL measurements at room temperatures can still be obtained, though with larger thermal broadening of the excited energy carriers. At room temperature,  $T$  the thermal broadening is roughly  $k_B T$ , where  $k_B$  is Boltzmann's constant. This gives rise to a broadening of 25meV at room temperature [69]. All our PL measurements were performed at room temperature.

## 4.2. RESULTS AND DISCUSSIONS

### 4.2.1 AFM studies of the ZnO nanoparticles in copolymer on Si substrate

This imaging technique has proved to be effective in our study of the morphology and physical parameters of the resultant ZnO nanoparticles. Due to soft polymer surface we used tapping mode atomic force microscopy (AFM) at a scan rate of 1.2Hz using a JSPM 4210 (JEOL) scanning probe microscope.

AFM images obtained for the nanocomposite films in all the copolymers verified spherical morphology for the ZnO nanoparticles. Fig. 4-2 show the AFM topographic image and corresponding 3-D image, respectively, of the ZnO-[PS]<sub>159</sub>/[PAA]<sub>63</sub> nanocomposite film on (100) p-Si surface in a scan area of 4.5x4.5  $\mu\text{m}$  at the center of the sample. The nanoparticles had a size distribution centered around 250nm, with a few larger particles around 350nm, resulting in an average size of 250nm. The density of the particles averaged over different areas at and near the center of a sample was found to be  $4 \times 10^7 \text{ cm}^{-2}$ . A linear surface scan profile across one of the nanoparticles (indicated by an arrow in fig. 4-3) is shown in fig. 4-2. The profiled nanoparticle has a lateral size of 350 nm and a height of about 124 nm. Similar evaluations for the nanoparticles in the ZnO-[PS]<sub>139</sub>/[PAA]<sub>17</sub> nanocomposite film on (100) p-Si surface (fig. 4-4 and fig. 4-5, scan area of 3 x 3  $\mu\text{m}$ ) with shorter block lengths revealed sizes ranging from 40 to 80 nm, with most particles at 60 nm, resulting in an average size of 60nm. The measured average density of the particles for this copolymer was found to be  $7 \times 10^8 \text{ cm}^{-2}$ . Fig. 4-6 and fig. 4-7 are AFM topographic image and its corresponding 3-D image, respectively, of nanoparticles

#### CHAPTER 4: CHARACTERIZATION OF ZnO NANOSTRUCTURES ON Si

developed using copolymer [PS]<sub>106</sub>/[PAA]<sub>17</sub> with similar minority block length, n but shorter majority block length, m as compared to that of [PS]<sub>139</sub>/[PAA]<sub>17</sub> copolymer on (100) p-Si in a scan area of 2.5x2.5 μm. In this system, the particle sizes measured on a sample ranged from 40 to 140 nm but it was found to be 60 nm when averaged over a large area on the sample. The average density of the nanoparticles for this copolymer was also evaluated as the other nanocomposite samples and found to be  $1 \times 10^{10} \text{ cm}^{-2}$ . Fig. 4-8 and fig. 4-9 show the nanocomposite films developed in [PS]<sub>106</sub>/[PAA]<sub>4</sub> copolymer in a scan area of 938 x 938 nm, having similar majority block length, m but shorter minority block length, n than that of [PS]<sub>106</sub>/[PAA]<sub>17</sub> copolymer. This resulted in ZnO nanoparticles with lateral size distribution, average size, and density of 10 to 60 nm, 20 nm, and  $1 \times 10^{10} \text{ cm}^{-2}$ , respectively.

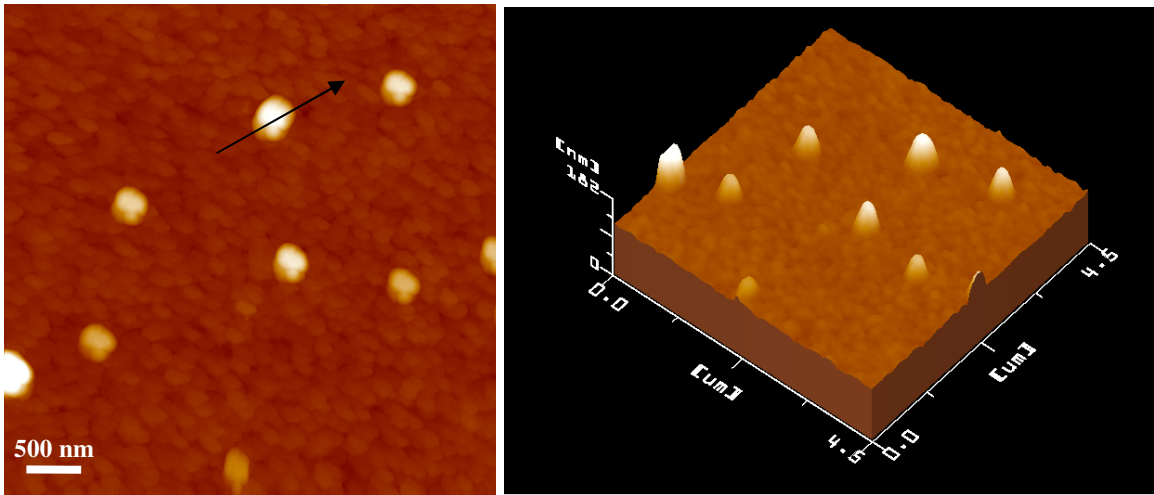


**Figure 4-2.** 2-D and 3-D AFM image of ZnO nanoclusters in [PS]<sub>159</sub>/[PAA]<sub>63</sub> system on Si surface in a 4.5x4.5 µm scan area.

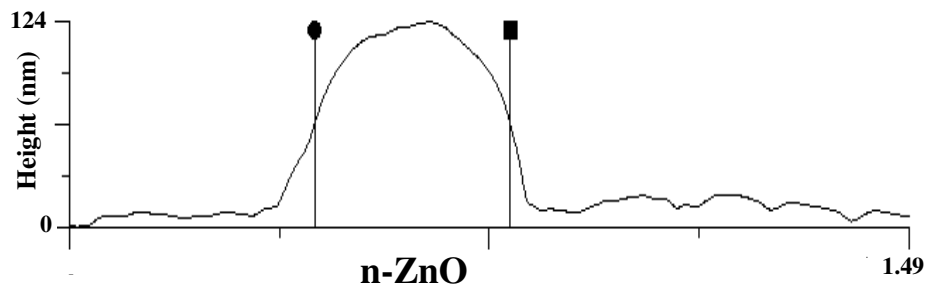


**Figure 4-3.** Linear surface scan profile across one of the nanoparticles indicated by the arrow in the AFM image of fig. 4-2. The profile shows the lateral size and height of the nanoparticle to be about 350 nm and 124 nm, respectively.



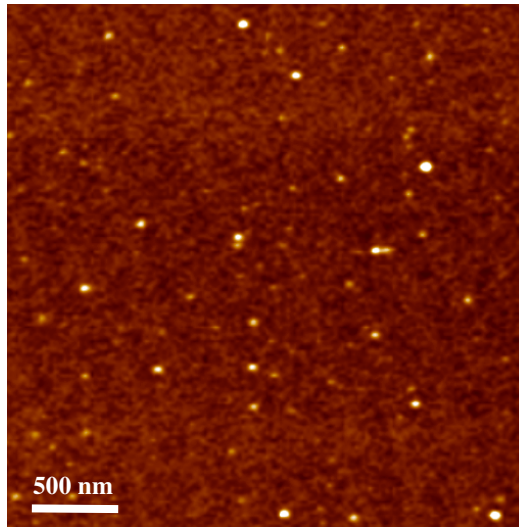


**Figure 4-4. 2-D AFM topographic image (3x3  $\mu\text{m}$  scan area) of the ZnO-[PS]<sub>139</sub>/[PAA]<sub>17</sub> nanocomposite film on (100) p-Si surface. ZnO nanostructures are observed to have lateral size distribution between 40 and 80 nm.**

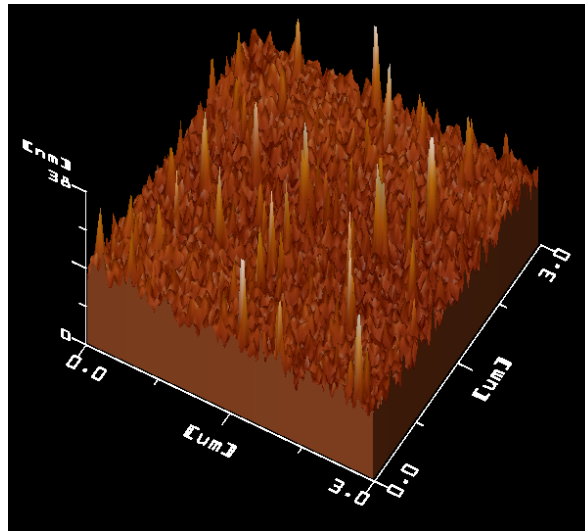


**Figure 4-5. 3-D AFM topographic image (3x3  $\mu\text{m}$  scan area) corresponding to fig. 4-4 of the ZnO-[PS]<sub>139</sub>/[PAA]<sub>17</sub> nanocomposite film on (100) p-Si surface.**

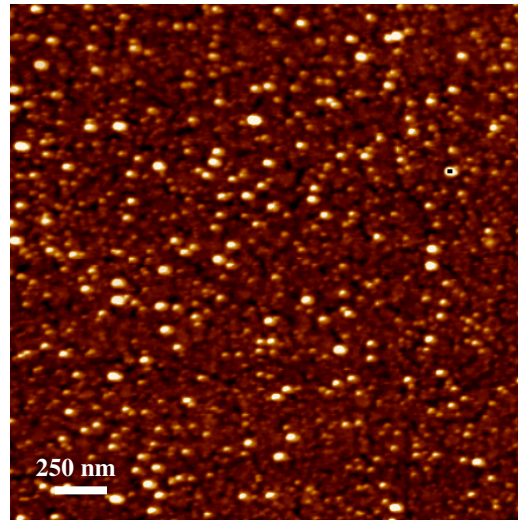


**Figure 4-6. 2-D AFM topographic image (2.5x2.5  $\mu\text{m}$  scan area) of the ZnO-[PS]<sub>106</sub>/[PAA]<sub>17</sub> nanocomposite film on (100) p-Si surface. ZnO nanostructures are observed to have lateral size distribution between 40 and 140 nm.**

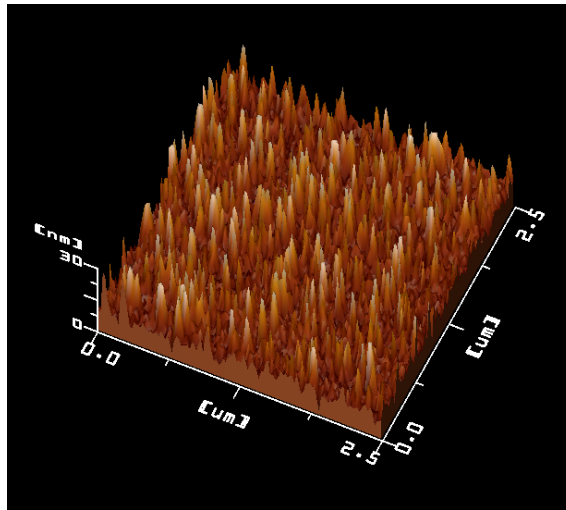


**Figure 4-7. 3-D AFM topographic image (2.5x2.5  $\mu\text{m}$  scan area) corresponding to fig. 4-6 of the ZnO-[PS]<sub>106</sub>/[PAA]<sub>17</sub> nanocomposite film on (100) p-Si surface.**

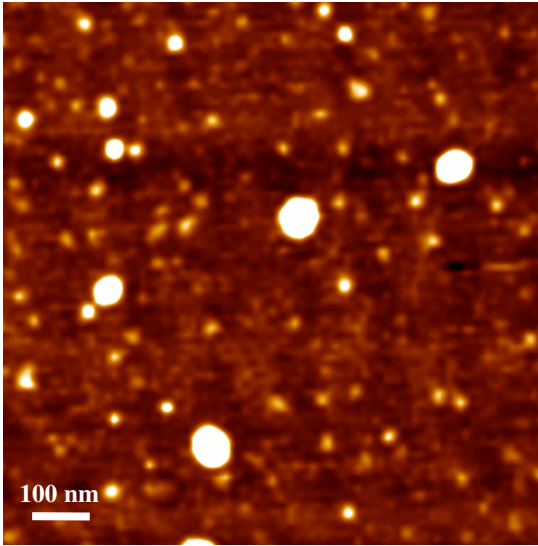


**Figure 4-8. 2-D AFM topographic image (938x938 nm scan area) of the ZnO-[PS]<sub>106</sub>/[PAA]<sub>4</sub> nanocomposite film on (100) p-Si surface. ZnO nanostructures are observed to have lateral size distribution between 10 and 60 nm.**

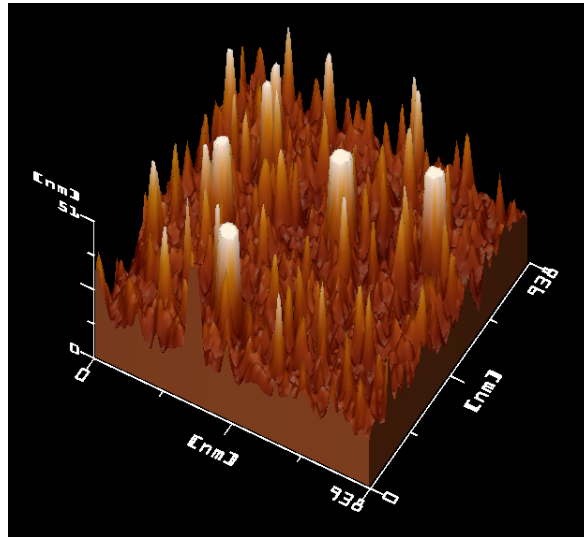


**Figure 4-9. 3-D AFM topographic image (936x936 nm scan area) corresponding to fig. 4-8 of the ZnO-[PS]<sub>106</sub>/[PAA]<sub>4</sub> nanocomposite film on (100) p-Si surface.**

The AFM evaluations showed that the size of the particles decreased with decreasing  $n$  of the copolymer from 63 to 17 to 4. On the other hand, similar sized particles were obtained in copolymers with the same  $n$  ( $n=17$ ) but with different  $m$  ( $m=139$  and  $106$ ). In terms of average density, we noticed that it increased with reducing  $m$  from 159 to 139 to 106, whereas, no significant change was observed in copolymers with the same  $m$  ( $m=106$ ), but different  $n$  ( $n=17$  and  $4$ ). This correlation between the copolymer parameters and nanoparticles can be explained with the help of the schematics in fig. 4-10, fig. 4-11, and fig. 4-12. Schematic of fig. 4-10 represents a copolymer film with spherical domains formed by microphase separation of minority blocks (thin solid line) from majority blocks (thick solid line) of a copolymer. As shown schematically in fig. 4-11, decreasing the minority block lengths with respect to those in fig. 4-10, decreases the domain size and increasing the majority block lengths only affects the density of domains by separating the domains further apart in the polymer matrix (fig. 4-12.) and vice versa. Since the spherical domains serve as templates for the ZnO nanoparticle synthesis, the factors affecting the domain size and density has similar effect on the developed nanoparticles as was evident in the AFM images. Thus comparing the ZnO nanoparticles obtained in all the copolymer systems showed that the smaller and denser particles are formed in the  $[PS]_{106}/[PAA]_4$  copolymer. This result is consistent with the fact that the  $[PS]_{106}/[PAA]_4$  copolymer has the shortest block lengths, ( $m$ ,  $n$ ), as compared with the other copolymers used. From these evaluations, we established that the average size of the ZnO nanoparticles is linearly dependent on the copolymer minority block

#### CHAPTER 4: CHARACTERIZATION OF ZnO NANOSTRUCTURES ON Si

length,  $n$ , (fig. 4-13), while the average density decreases exponentially with increasing copolymer majority block length,  $m$ , (fig. 4-14).

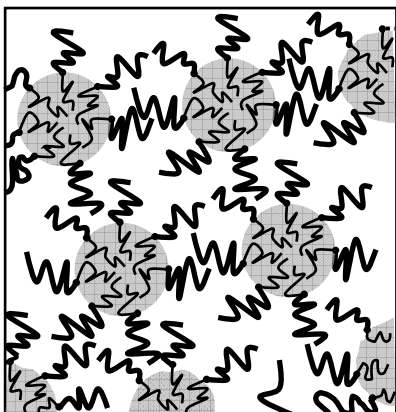


Figure 4-10. Schematic of a copolymer film with spherical nanodomains (grey regions) formed by minority blocks (—) within the matrix formed by majority blocks (—) of the copolymer.

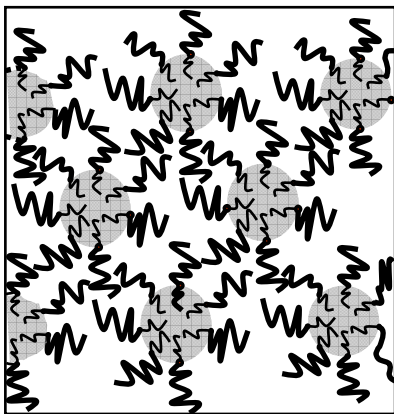


Figure 4-11. Schematic of a copolymer film with decreased minority block lengths with respect to that of fig. 4-10, resulting in decreased domain size compared to that of fig. 4-10.

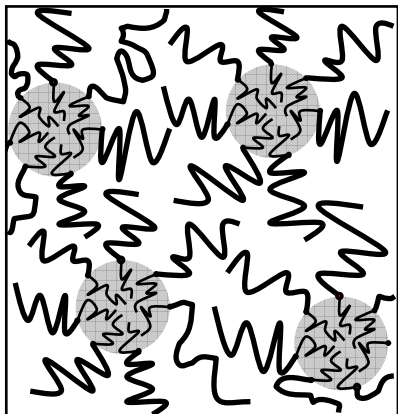
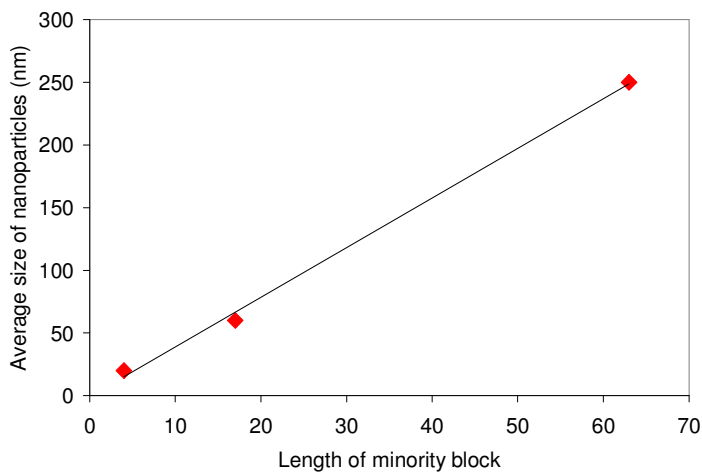
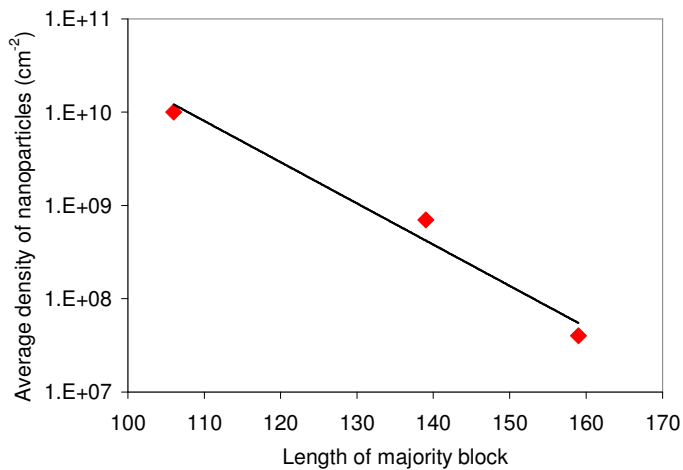


Figure 4-12. Schematic of a copolymer film with increased majority block lengths with respect to that of fig. 4-10, resulting in decreased domain density compared to that of fig. 4-10.



**Figure 4-13. Dependence of average size of ZnO nanoparticles in  $[PS]_m/[PAA]_n$  copolymer on minority block length, n.**



**Figure 4-14. Dependence of average density of ZnO nanoparticles in  $[PS]_m/[PAA]_n$  copolymer on majority block length, m.**

### **Effects of precursor non-stoichiometric doping**

To investigate the effects of precursor over-doping in the self-assembly process, the copolymer solution was doped with double the required stoichiometric amount of ZnCl<sub>2</sub> solution and all the other parameters of the synthesis process were kept constant. The over-doped ozone treated nanocomposite films were studied with AFM. Fig. 4-15 shows a 2-D AFM topographic image and its corresponding 3-D image of ZnO nanoclusters in the [PS]<sub>106</sub>/[PAA]<sub>17</sub> copolymer matrix on SiO<sub>2</sub>/Si surface with ZnCl<sub>2</sub> over-doping in a 15x15µm scan area. As a result of the non-stoichiometric doping the nanoparticles were found to have a significantly larger lateral size distribution (80-650 nm), than without over-doping (fig. 4-6). We also observed that the excess doping did not significantly affect the average density of the nanoparticles, which depends on the density of the nanodomains that are dependent on minority block length of the copolymer. The density of the nanoclusters in this over-doped system was evaluated to be  $1.7 \times 10^8/\text{cm}^2$ .



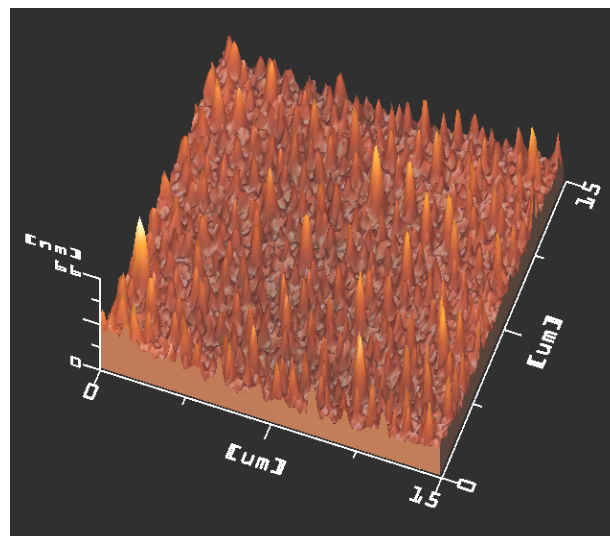
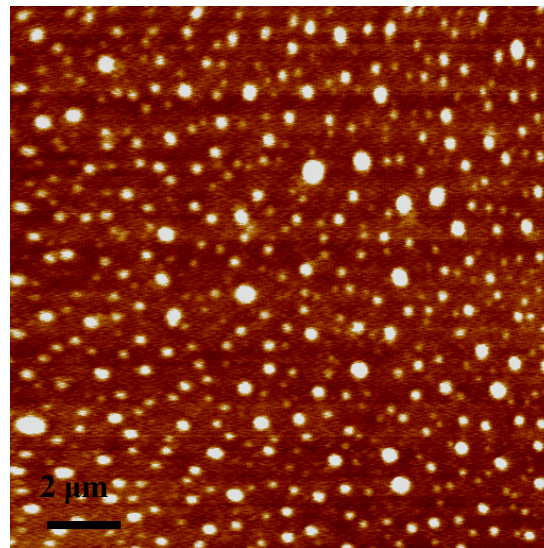


**Figure 4-15. 2-D and 3-D AFM image of over-doped ZnO-[PS]<sub>106</sub>/[PAA]<sub>17</sub> nanocomposite films on SiO<sub>2</sub>/Si surface in a 15x15 μm scan area.**

#### 4.2.2 Structural characteristics of the ZnO nanoparticles in copolymer on Si substrate

X-ray diffraction  $\theta$ - $2\theta$  scans were recorded for  $2\theta$  values between  $30^\circ$  and  $75^\circ$  for structural evaluation of the developed ZnO nanoparticles in the nanocomposite films on (100) Si substrate. The measurements were performed at room temperature with a Rigaku 18 kW rotating anode source x-ray diffractometer (XRD) using the Cu  $K_{\alpha 1}$  line ( $\lambda = 1.54 \text{ \AA}$ , energy = 8.8 keV) and operating at 50 kV, 100 mA with slits set at  $10 \times 2 \text{ mm}^2$ . The samples were attached to a post and placed in the center of a four-circle goniometer for the  $\theta$ - $2\theta$  scans. The Si (111) peak was used to center the diffraction patterns.

X-ray diffraction (XRD) was performed in the  $\theta$ - $2\theta$  scan mode to determine the crystallographic orientation and quality of the ZnO nanoparticles on Si. In fig. 4-16, the diffraction pattern obtained for the ZnO-[PS]<sub>159</sub>/[PAA]<sub>63</sub> nanocomposite film on p-type (100) Si substrate before and after misalignment of  $\theta$  by  $6^\circ$  is shown by the solid line and the dotted line, respectively. Due to the smaller dimensions and large separations between the nanoparticles as observed from the AFM images, the nanoparticle diffraction patterns exhibited low signal-to-noise ratio and broad peaks. This caused some of the ZnO peaks to be masked by the sharper Si peaks present at  $2\theta$  values close to that of ZnO. These peaks could be clearly detected only when  $\theta$  was misaligned by  $6^\circ$  with the substrate orientation to remove the stronger Si peaks from the substrate (fig. 4-16, dotted line). The peaks observed at  $31.8^\circ$ ,  $36.5^\circ$ ,  $47.9^\circ$  and  $65.1^\circ$  are attributed to (100), (101), (103) and (200) ZnO crystal orientations,

respectively. The  $\theta$ - $2\theta$  scan thus showed that the particles formed in [PS]<sub>m</sub>/[PAA]<sub>n</sub> copolymer matrix have a wurtzite crystal structure and indicated the (100) diffraction peak to be the dominant orientation.

XRD rocking curves of the (100), (101), and (200) ZnO diffraction peaks were also measured as shown in fig. 4-17, fig. 4-18, and fig. 4-19, respectively, to maximize the signal of the peaks and evaluate their FWHM values. Comparing these figures we see that the FWHM values of both the (100) and (200) peaks were about 13°, and was almost half of that of the (101) peak which was about 25°. The sharper peaks along the (100) direction confirm the preferential orientation of the self-assembled nanoparticles on the (100) Si substrate.

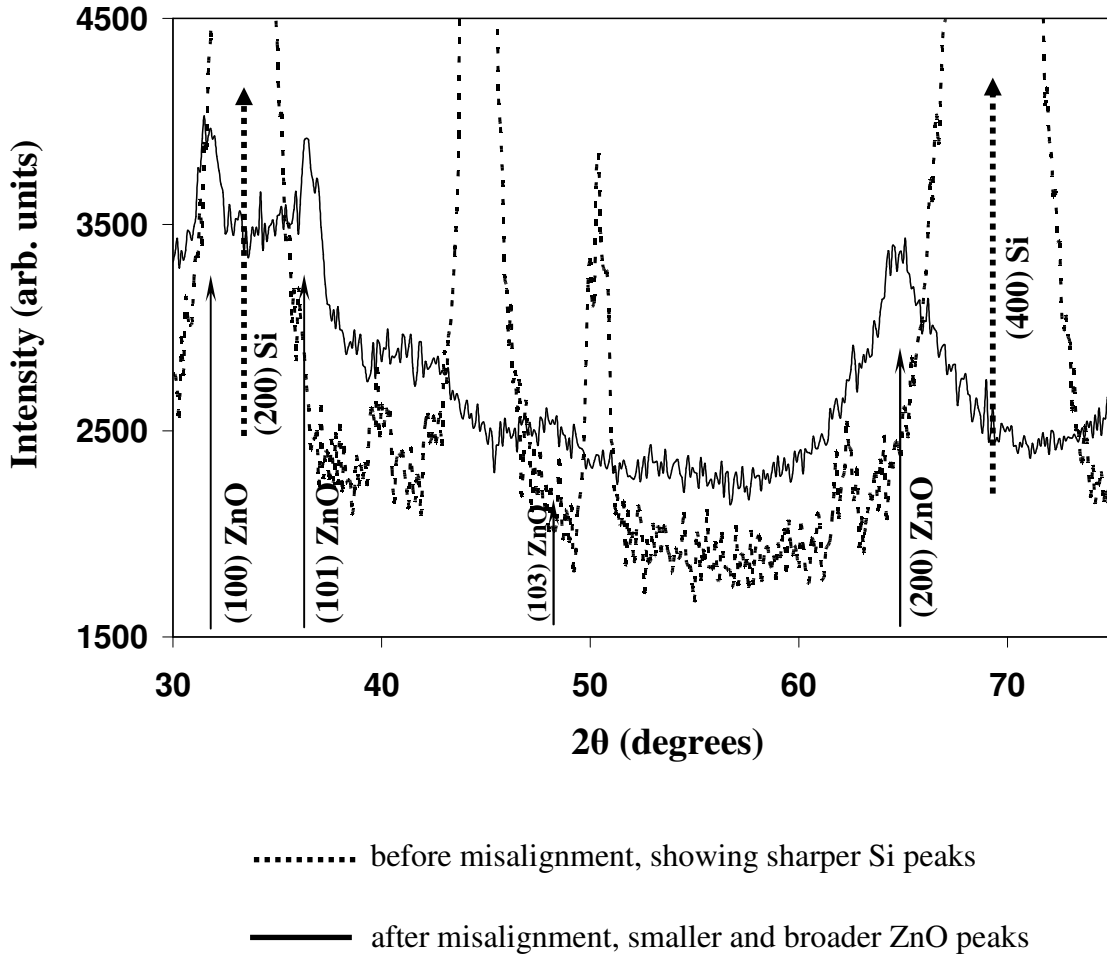


**Figure 4-16.  $\theta$ - $2\theta$  XRD pattern of ZnO nanoparticles in [PS]<sub>159</sub>/[PAA]<sub>63</sub> copolymer on (100) Si substrate.**

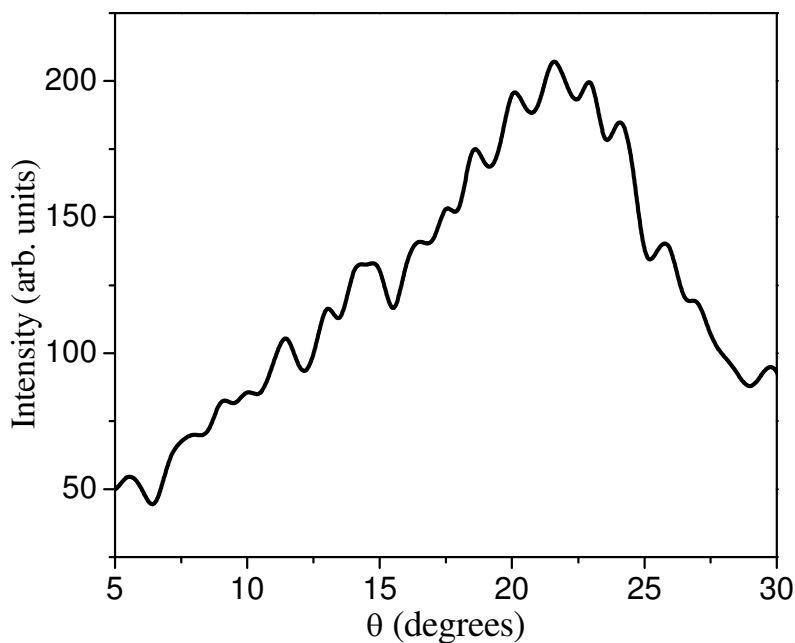


**Figure 4-17. XRD rocking curve corresponding to the (100) diffraction peak of ZnO nanoparticles developed in [PS]<sub>159</sub>/[PAA]<sub>63</sub> copolymer.**

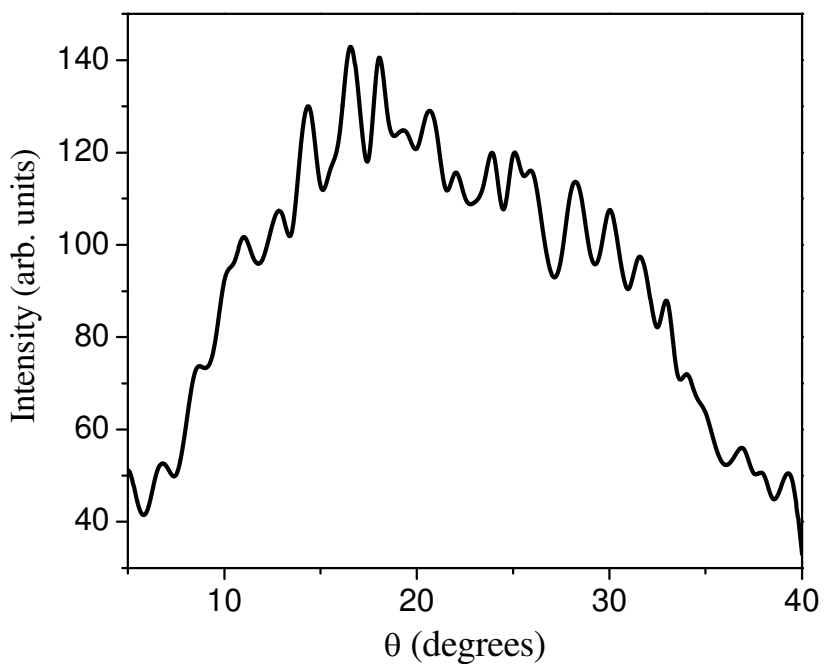


**Figure 4-18. XRD rocking curve corresponding to the (101) diffraction peak of ZnO nanoparticles developed in [PS]<sub>159</sub>/[PAA]<sub>63</sub> copolymer.**

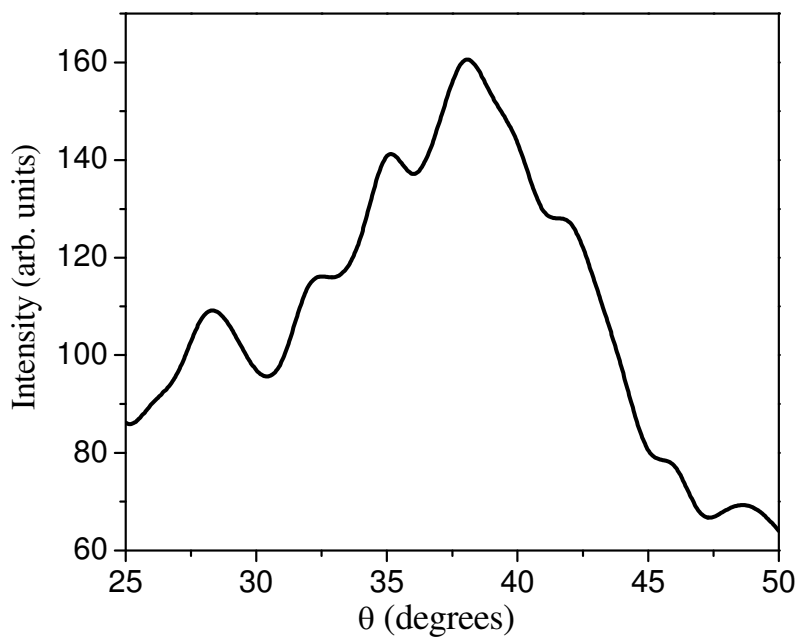


**Figure 4-19. XRD rocking curve corresponding to the (200) diffraction peak of ZnO nanoparticles developed in [PS]<sub>159</sub>/[PAA]<sub>63</sub> copolymer**

### **4.2.3 Optical characteristics of the ZnO nanoparticles in copolymer on Si substrate**

Room temperature photoluminescence measurements were performed on ZnO nanostructures of two different sizes on Si substrates with a Cary Eclipse Spectrophotometer. The excitation source of the spectrophotometer is a Xenon flash lamp. The PL spectrum was obtained for an excitation wavelength set at 270 nm with the help of an external bandpass filter centered at 270 nm and a bandwidth of 10 nm.

The optical properties of the nanoparticles were studied by photoluminescence spectroscopy in order to evaluate the luminescence properties, the effect of quantum confinement on the energy band gaps, and the defect levels and quality of nanostructures, with size and density. Fig. 4-20 and fig. 4-21 shows room temperature photoluminescence spectra of ZnO nanoparticles on Si substrate in [PS]<sub>153</sub>/[PAA]<sub>60</sub> copolymer with an average size of 250 nm and in [PS]<sub>106</sub>/[PAA]<sub>4</sub> copolymer with an average size of 20 nm, respectively. Photoluminescence obtained from 250 nm ZnO nanostructures at room temperature showed a UV emission peak at 372 nm corresponding to near band edge luminescence with energy of 3.33 eV. In comparison, photoluminescence from the 20 nm ZnO nanostructures exhibited a peak at 363 nm corresponding to near band edge energy luminescence of 3.42 eV. This showed a blue shift in the UV emission of the smaller particles with respect to the larger particles. This is in agreement with the size quantum confinement effect as evident by the blue shift of the UV emission peaks and the corresponding widening of their energy band gaps [70]. A green-yellow luminescence centered at 555 nm corresponding to a defect level of 2.23 eV was observed in both the nanoparticle

#### CHAPTER 4: CHARACTERIZATION OF ZnO NANOSTRUCTURES ON Si

systems. This defect level can be attributed to the presence of intrinsic defects, like oxygen vacancies and Zn interstitials [71, 72, 73]. Thus the presence of the green luminescence is indicative of n-type conductivity of the unintentionally doped ZnO nanoparticles.



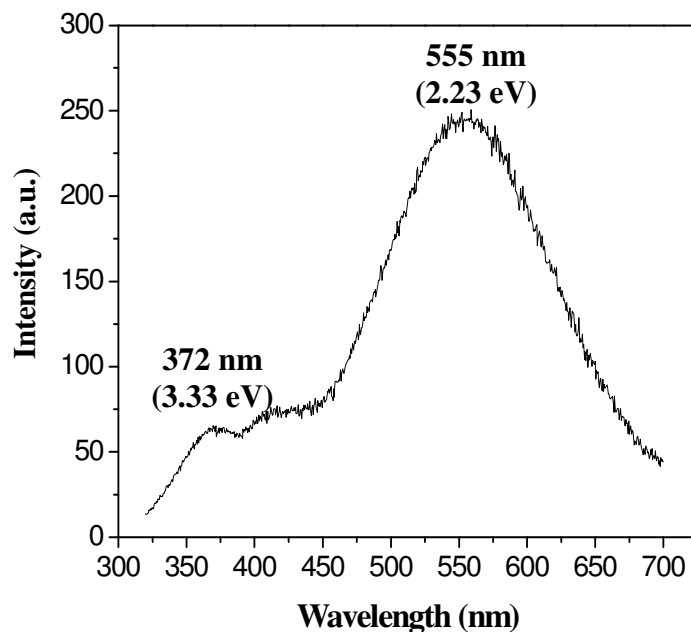


**Figure 4-20. Photoluminescence spectrum of 250 nm ZnO nanoparticles in [PS]<sub>159</sub>/[PAA]<sub>63</sub> copolymer at room temperature**

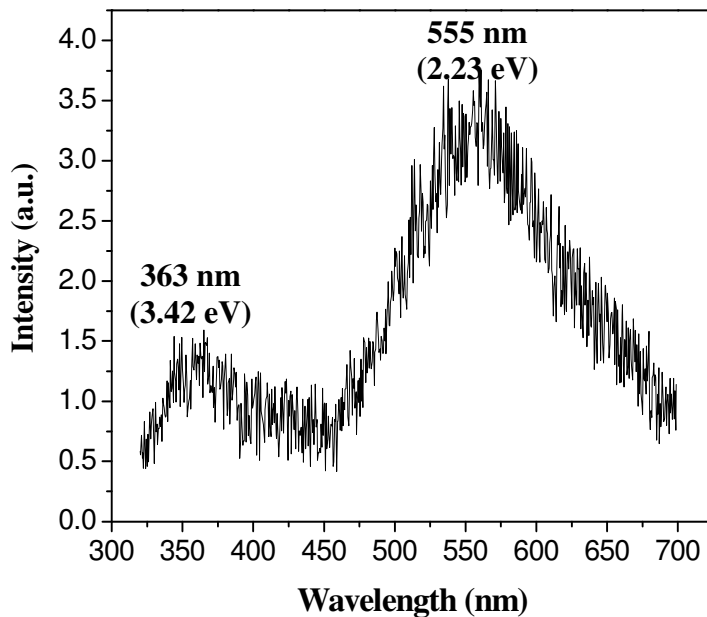


**Figure 4-21. Photoluminescence spectrum of 20 nm ZnO nanoparticles in [PS]<sub>109</sub>/[PAA]<sub>4</sub> copolymer at room temperature**

### 4.3 SUMMARY

This chapter presents the characteristics of the ZnO nanoparticles developed on large area Si wafers using diblock copolymers. AFM was used to evaluate the size and density of ZnO nanoparticles in four different configurations of the  $[PS]_m/[PAA]_n$  copolymer. The largest nanostructures had average sizes of 250 nm and densities of  $1 \times 10^7 \text{cm}^{-2}$  for the 159/63 ratio copolymer while the smallest nanostructures had average sizes of 20 nm and densities of  $1 \times 10^{10} \text{cm}^{-2}$  for the 106/4 ratio copolymer. AFM studies helped determine the correlation between the particle parameters and the copolymer block lengths (m, n) and established that the nanoparticle average size increased linearly with minority block length n, while the average density decreased exponentially with majority block length m. X-ray diffraction revealed wurtzite structure with dominant orientation along (100) that of Si substrate suggesting pseudo-epitaxial nature of the nanoparticles.

Photoluminescence obtained from 250 nm ZnO nanostructures at room temperature showed a UV emission peak at 372 nm corresponding to near band edge luminescence with energy of 3.33 eV. In comparison, photoluminescence from the 20 nm ZnO nanostructures exhibited a blue shifted peak at 363 nm corresponding to near band edge energy luminescence of 3.42 eV that is in agreement with size quantum confinement effect. A green-yellow luminescence centered at 555 nm corresponding to a defect level of 2.23 eV was observed in the nanoparticle systems. This defect level can be attributed to the presence of intrinsic defects, like oxygen vacancies and Zn interstitials.

## **CHAPTER 5**

# **ELECTRICAL CHARACTERIZATION OF ZnO-COPOLYMER-NANOCOMPOSITE/Si HETEROSTRUCTURES**

This chapter presents the development of novel ZnO-nanocomposite/Si n-p heterojunction diodes and the studies of the electrical and transport properties of these heterostructures. Current-voltage and capacitance-voltage measurements were performed in order to evaluate the devices. These nano-diode heterojunctions showed rectifying properties with good rectification ratio and small leakage currents.

## **5.1 BACKGROUND**

### **5.1.1 P-N Heterojunction Diodes**

A p-n heterojunction diode is similar to a p-n homojunction diode in principle but is formed between two dissimilar semiconductors. A unique feature of the heterojunction diode is the band discontinuity or band offset formed at the metallurgical junction of the diode due to unequal band gaps of the semiconductors involved. The band offsets play an important role in the current transport properties of heterojunction diodes. Depending on the alignment of the energy bands of the semiconductors in the heterojunction diodes, they can be classified as (fig. 5-1): a) straddled or Type I alignment, b) staggered or Type II alignment, and c) broken gap alignment.

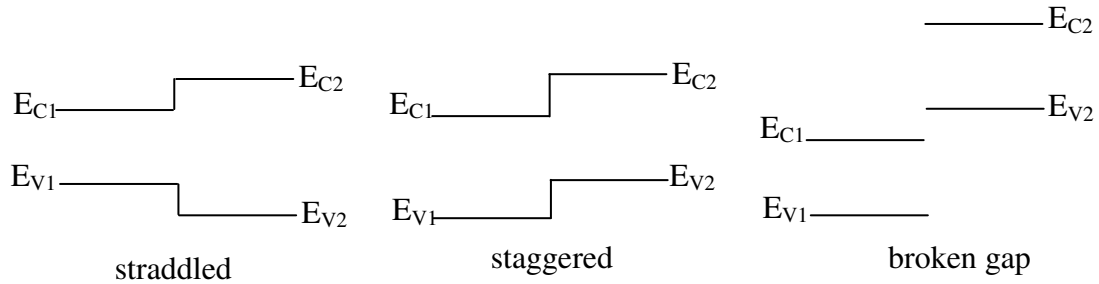


**Figure 5-1. Types of energy band alignments in heterojunction diodes**

The first heterojunction of Ge/GaAs was developed by Anderson in 1960. He developed the electron affinity model also known as the Anderson model to determine the energy band diagram of heterojunctions at the interface which helps to predict current flow in heterojunctions [76]. This is considered to be the fundamental model for heterojunctions. The model is based on the ideal performance of a heterojunction diode in which current transport is assumed to be entirely by injection of carriers over the band offsets into the quasi-neutral region of the diode and no interface states are present at the junction. This is rarely the case in typical heterojunctions but this model is used as a basis to evaluate performances of other heterojunctions.

The model gives the relationships between the bandgaps, electron affinities and work functions of the two semiconductors to determine the band discontinuities and total band bending at the interface (built-in voltage) of the heterojunction. Assuming semiconductor 1 and 2 to have bandgaps of  $E_{g1}$  and  $E_{g2}$ , electron affinities of  $\chi_1$  and  $\chi_2$ , work functions of  $\Phi_1$  and  $\Phi_2$ , doping densities of  $N_1$  and  $N_2$ , and

dielectric constants of  $\epsilon_1$  and  $\epsilon_2$ , respectively, the relationships defined by the Anderson model are given below.

$$\Delta E_C = \chi_1 - \chi_2 \dots\dots\dots (1)$$

$$\Delta E_V = (E_{g1} - E_{g2}) \pm \Delta E_C \dots\dots\dots (2)$$

$$V_{bi} = \Phi_1 - \Phi_2 \dots\dots\dots (3)$$

$$V_{bi} = V_{b1} + V_{b2} \dots\dots\dots (4)$$

$$V_{b1}/V_{b2} = N_2\epsilon_2/N_1\epsilon_1 \dots\dots\dots (5)$$

$\Delta E_C$  and  $\Delta E_V$  are the conduction and valence band discontinuities, respectively, and in Eq. 2 the  $\Delta E_C$  is subtracted for type I and added for type II alignment heterojunctions. According to the sign convention for  $\Delta E_V$ , positive value suggests that the valence band of semiconductor is higher than that of semiconductor 2.  $V_{b1}$  and  $V_{b2}$  are the portions of the built-in ( $V_{bi}$ ) voltage or the total band bending of the heterojunction supported by each semiconductor at thermal equilibrium and the ratio of band bending at each side of the semiconductor at the interface is given by Eq. 5. The Anderson model has been used to predict the energy band diagram of the ZnO/Si material system used in our work which is a type II alignment heterojunction as shown in fig. 5-3. Anderson model has been successful in predicting the band discontinuities of many heterojunctions but the current-voltage relationship given by this model usually does not agree with experimental values obtained from

heterojunctions. This is due to the abrupt metallurgical junction and the absence of interface states assumed in the model which are not always possible to achieve during heterojunction fabrication. In practical heterojunction diodes, current transport usually arises from a combination of carrier injection over band offsets (diffusion or thermionic emission), recombination of carriers in depletion region and tunneling of carriers into interface states but with only one of them being the dominant transport. There is not a definite model to predict current transport in heterojunctions as it is strongly influenced by the quality of the fabricated junction. Depending on junction properties, there are several transport models that have been proposed. Some of them are mentioned here. Injection of carriers and diffusion in the quasi-neutral region has been proposed for abrupt junctions with well lattice-matched semiconductors and small difference in band offsets of the heterojunction. Recombination in the depletion region of the smaller bandgap semiconductor for junctions with large difference in band offsets and interface states. This induces single carrier flow over the smaller band offset and bottlenecks the flow of the opposite carrier over the larger band offset of the heterojunction which results in recombination in the depletion region (discussed in §5.4.1). Another is the tunneling-recombination dominated transport for junctions with large density of interface states and highly doped semiconductors (discussed in §5.4.1).

**5.1.2 Evaluation Techniques of P-N Diode Characteristics**

Current-Voltage Measurements

The current-voltage relation of an ideal p-n diode is expressed by the Shockley diode equation [74],

$$I = I_s \left[ \exp\left(\frac{qV}{kT}\right) - 1 \right] \dots\dots\dots (6)$$

where  $I_s$  is the reverse saturation current,  $V$  is the voltage at the junction or applied voltage, and  $kT/q$  is the thermal voltage. Shockley’s ideal theory predicts voltage-independent saturation current for reverse bias, and forward current that follows the exponential law,  $\exp(qV/kT)$  for forward bias. However, non-idealities observed due to recombination-generation current from recombination and generation of carriers in the depletion region was recognized by Sah, Noyce and Shockley. They developed the space-charge layer recombination-generation theory [74] which showed that reverse current is voltage dependent and does not saturate to a constant  $-I_s$  as in the Shockley model and at low forward bias, current follows the exponential law,  $\exp(qV/2kT)$ . To account for this non-ideality, the ideal diode equation is modified by including the parameter  $\eta$ ,

$$I = I_s \left[ \exp\left(\frac{qV}{\eta kT}\right) - 1 \right] \dots\dots\dots (7)$$

where  $\eta$  is the junction ideality or quality factor which determines the departure from the ideal diode characteristics. The recombination-generation current theory [75] accounts for the ideality factor values in the range of  $1 < \eta \leq 2$ . As per the Sah–Noyce–Shockley theory, forward current dominated by recombination of minority

carriers in the quasi-neutral regions i.e. current limited by diffusion gives an ideality factor of 1 and that dominated by recombination of carriers in the depletion region gives an ideality factor of 2.

There are other effects that have not been accounted for in the Sah-Noyce-Shockley model or equation (7) that lead to non-ideal behavior. These include effects due to recombination in surface states, tunneling of carriers between states in the band-gap, high injection of carriers at large bias and voltage drop across quasi-neutral regions and at external contacts. These effects give rise to components in the diode current and most often account for  $\eta > 2$ . The effect due to voltage drop in the diode other than the depletion region is known as the series resistance effect and becomes pronounced at high voltages which then gives the diode I-V relation as,

$$I = I_s \left[ \exp\left(\frac{qV - IR_s}{\eta kT}\right) - 1 \right] \dots\dots\dots (8)$$

where,  $R_s$  is the series resistance and  $IR_s$  is the voltage drop in the quasi-neutral region of the semiconductor. In this bias region, due to the series resistance effect the current no longer exhibits exponential dependence on the applied voltage instead behaves linearly with voltage.

In order to evaluate the performance of a p-n junction diode, the characteristic parameters of the diode like reverse saturation current, ideality factor, and series resistance are determined to measure against those of an ideal diode. To determine the characteristics of the diode, dc current-voltage measurements of the diode are plotted on a semi-logarithmic scale and the diode parameters are extracted from the plot. The ideality factors of the diode are obtained from the slope of the log I-V plot and the y-



intercept gives the reverse saturation current of the diode. This follows from Eq. 7 for  $V > 3kT/q$  and with series resistance neglected by taking its natural logarithm which gives equation (9),

$$\ln I = \ln I_s + \frac{qV}{\eta kT} \dots\dots\dots (9)$$

Eq. (9) represents a straight line on a log I vs. V plot with  $q/\eta kT$  as the slope and  $I_s$  as the y-intercept. From Eq (9), the ideality factor can be expressed as,

$$\eta = \frac{q}{kT} \frac{dV}{d(\ln I)} \dots\dots\dots (10)$$

Thus, taking the slope of linear regions of logI-V plots of diodes and solving Eq. (10) gives the ideality factors.

Fig. 5-2 shows a schematic of log I-V characteristics of a practical p-n junction diode with the four regions generally observed although the high injection region is often masked by the series resistance effects. The figure shows the graphical determination of the reverse saturation current from the y-intercept of the straight line from the ideal diode region. The ideality factors at different regions of the plot calculated from the slope of the linear part of those regions are shown. The ideal diode region has an ideality factor of 1 whereas the recombination and high injection region has an ideality factor of 2. At larger bias it can be seen that the current starts to deviate from its exponential behavior due to series resistance effect. The deviation of the plot from linearity is marked with  $\Delta V$  in the figure. Since  $\Delta V = IR_s$ , the slope obtained from a plot of  $\Delta V$  vs I gives the series resistance,  $R_s$  of the diode.

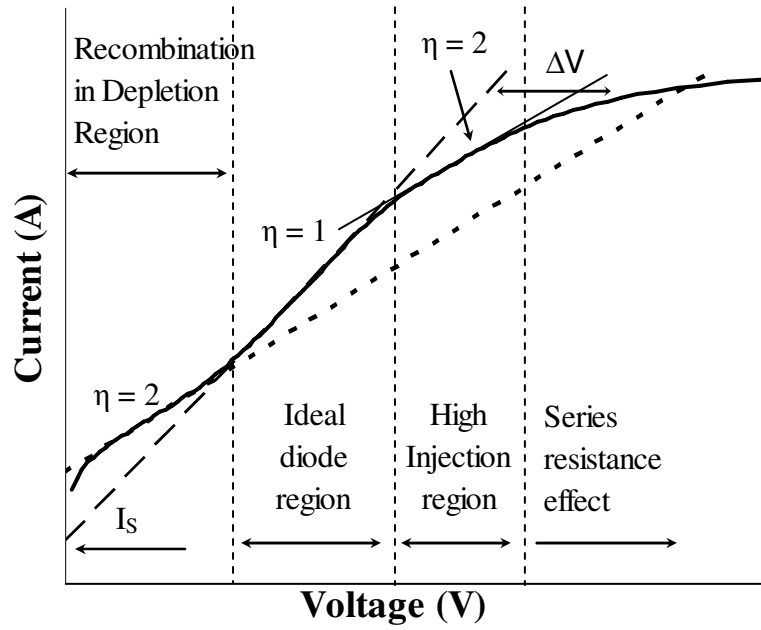


Figure 5-2. Schematic of log I-V characteristics of a practical p-n junction diode

Capacitance-Voltage Measurements

Capacitance-voltage characteristics of a p-n junction diode can be used to determine the junction properties of the diode. From measured C-V plots of diodes the abrupt nature of the junction, built-in voltage and doping density can be determined. For an abrupt p-n heterojunction diode, the capacitance-voltage relation is given by [89],

$$C^2 = \frac{qA^2 N_1 N_2 \epsilon_1 \epsilon_2}{2(N_1 \epsilon_1 + N_2 \epsilon_2)(V_{bi} - V_a)} \dots\dots\dots (11)$$

where C is the depletion region capacitance,  $V_a$  is the applied bias,  $V_{bi}$  is the built-in voltage,  $N_1$  and  $N_2$  are the majority doping densities, and  $\epsilon_1$  and  $\epsilon_2$  are the dielectric constants of semiconductor 1 and 2 of the heterojunction, respectively.

Eq. 11 can be written as,

$$\frac{1}{C^2} = \frac{2(N_1 \epsilon_1 + N_2 \epsilon_2)}{qA^2 N_1 N_2 \epsilon_1 \epsilon_2} (V_{bi} - V_a) \dots\dots\dots (12)$$

Eq. 12 represents a straight line on a plot of  $1/C^2$  vs  $V_a$  with an inverse slope of

$$\frac{2(N_1 \epsilon_1 + N_2 \epsilon_2)}{qA^2 N_1 N_2 \epsilon_1 \epsilon_2}$$

and extrapolation of the straight line to  $1/C^2 = 0$  gives an intercept at

$$V_a = V_{bi}.$$

Thus a linear plot of the  $C^{-2}$ -V characteristics of the diode predicts the abrupt nature of the junction and the x-intercept gives the built-in voltage. With the doping density of one of the semiconductors known, the doping density of the other semiconductor can be predicted from the slope of the linear  $C^{-2}$ -V plot with Eq.13

$$\frac{d(1/C^2)}{dV_a} = \frac{2(N_1 \epsilon_1 + N_2 \epsilon_2)}{qA^2 N_1 N_2 \epsilon_1 \epsilon_2} \dots\dots\dots (13)$$

## 5.2 ENERGY BAND DIAGRAM OF n-ZnO/p-Si HETEROJUNCTION

Fig. 5-4 shows a proposed energy band diagram of an abrupt n-ZnO/p-Si heterojunction at thermal equilibrium. The band diagram was determined based on our experimental results of the 250 nm n-ZnO nanoparticles on p-Si and reported values with the effect of interface and surface states neglected according to standard heterojunction theory (Anderson model) [76].

From our C-V measurements (§ 5.4.2), it was determined that an abrupt heterojunction was formed and a donor density of  $3 \times 10^{15} \text{ cm}^{-3}$  was evaluated for the ZnO nanoparticles. The p-Si substrate was used with a doping density of  $1 \times 10^{15} \text{ cm}^{-3}$ . An energy band gap of 3.33 eV was used for ZnO as indicated by our photoluminescence studies and an energy band gap of 1.12 eV was used for Si as reported [74]. The electron affinities ( $\chi$ ) of ZnO and Si have been reported to be 4.35 eV and 4.05, respectively [77, 78].

Since the energy band gaps of the two materials are different, band discontinuities are expected in one or both band edges at the interface. The conduction band discontinuity ( $\Delta E_C$ ) at the interface of the heterojunction was calculated to be 0.3 eV by following the electron affinity rule of the Anderson model,  $\Delta E_C = \chi_{\text{ZnO}} - \chi_{\text{Si}}$ . The valence band discontinuity ( $\Delta E_V$ ) then follows as,  $\Delta E_V = (E_{g,\text{ZnO}} - E_{g,\text{Si}}) + \Delta E_C$ , which was found to be -2.51 eV. The negative value suggests that the valence band of ZnO is lower than that of Si.

The value of  $\delta_n = 0.18 \text{ eV}$ , was calculated from,  $\delta_n = E_{Fn} - E_{Cn} = kT \ln(N_d/N_C)$  with  $N_C = 2.94 \times 10^{18} \text{ cm}^{-3}$  calculated from

$$N_c = 2 \left( \frac{2\pi m_n^* kT}{h^2} \right)^{3/2}, \text{ where the electron effective mass of ZnO, } m_n^* = 0.24m_o \text{ [71]}$$

and  $h$  is the Plank's constant. For  $\delta_p$ , the value of 0.24 eV was calculated from

$$\delta_p = E_{Vp} - E_{Fp} = kT \ln \frac{N_a}{N_v} \text{ with } N_v = 1.04 \times 10^{19} \text{ cm}^{-3} \text{ [82].}$$

The total built-in voltage  $V_{bi}$ , of the heterojunction is the sum of the partial built-in voltages supported by ZnO ( $V_{b1}$ ) and Si ( $V_{b2}$ ) [82]. The ratio of the built-in voltages is determined from  $V_{b1}/V_{b2} = N_A \epsilon_{Si} / N_D \epsilon_{ZnO}$  satisfying charge conservation of the depletion region of the heterojunction. The ratio was calculated to be 1:2.8 with  $\epsilon_{ZnO} = 8.5$  [79] and  $\epsilon_{Si} = 11.9$  [82]. The built-in voltage of the heterojunction is calculated from the difference in work function of the two materials. This is given by,

$$V_{bi} = \Phi_{Si} - \Phi_{ZnO} = \chi_{Si} + (E_{g,Si} - \delta_p) - (\chi_{ZnO} + \delta_n) \text{ and was found to be 0.4 eV.}$$

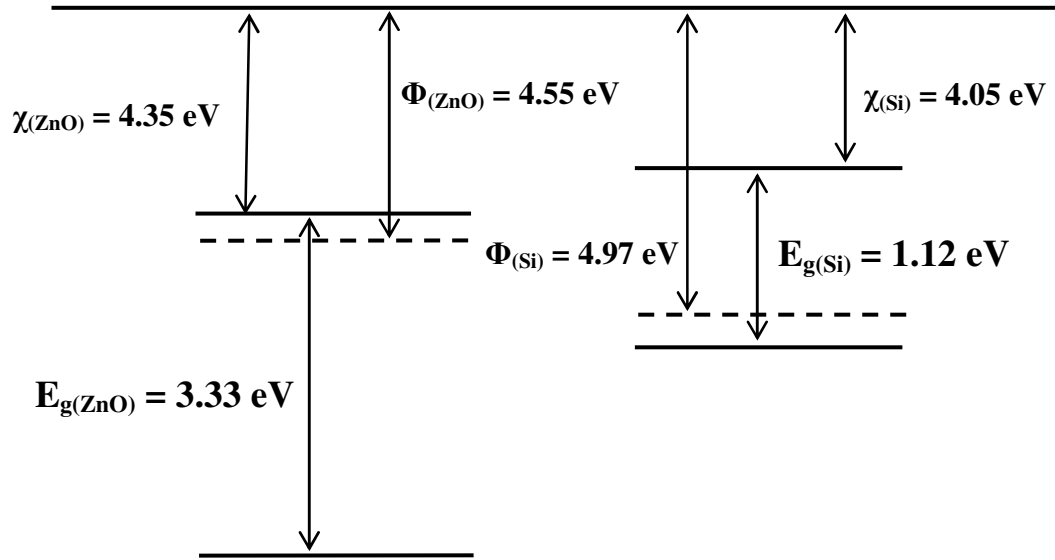


Figure 5-3. Energy band diagram of n-ZnO and p-Si before junction formation

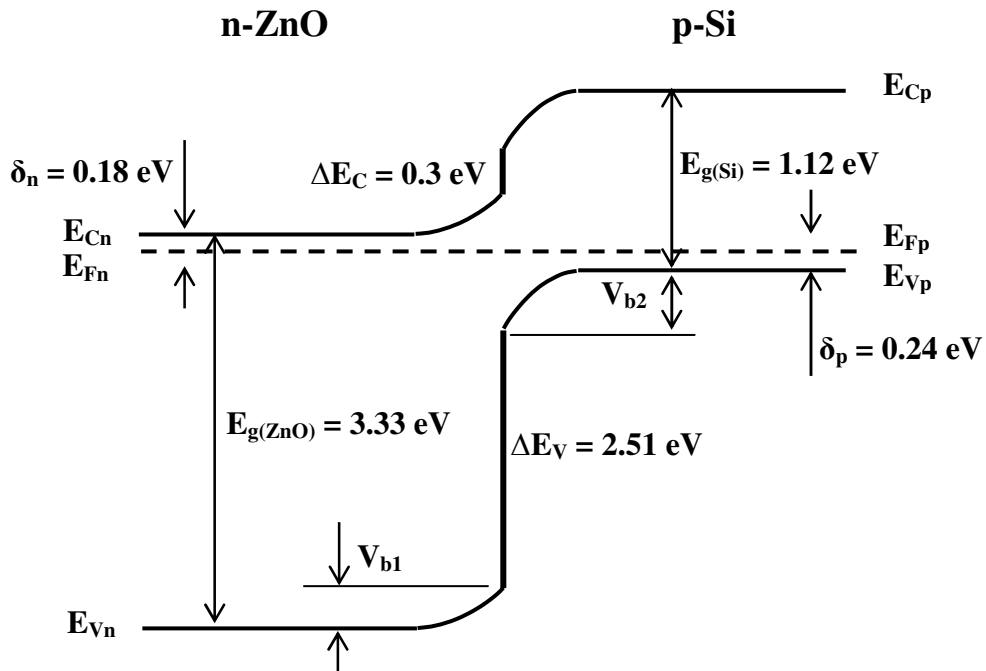
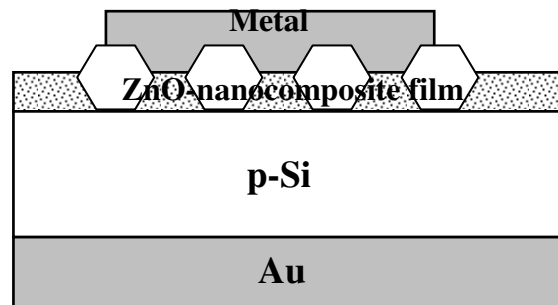


Figure 5-4. Energy band diagram of an abrupt n-ZnO/p-Si heterojunction at thermal equilibrium

### 5.3 EXPERIMENTAL DETAILS

The electrical studies were carried out for nanocomposite films of ZnO nanoparticles in the two copolymers of [PS]<sub>159</sub>[PAA]<sub>63</sub> and [PS]<sub>106</sub>[PAA]<sub>4</sub> on p-Si substrates. As mentioned earlier in chapter 4, the [PS]<sub>159</sub>[PAA]<sub>63</sub> system gave nanoparticles with size and density of 250 nm and  $4 \times 10^7 \text{ cm}^{-2}$  respectively, and the [PS]<sub>106</sub>[PAA]<sub>4</sub> system gave substantially smaller nanoparticle size at 20 nm and higher density  $1 \times 10^{10} \text{ cm}^{-2}$ . Fig. 5-5 shows a schematic of the heterostructure used to study the current-voltage and capacitance-voltage characteristics of the developed ZnO-copolymer-nanocomposite/Si heterostructure. The I-V and C-V measurements were made for two different top metal electrodes – Al and Au – on the ZnO-copolymer nanocomposite film. In both cases, top contacts were made with a diameter of 0.5 mm and a thickness of 50 nm and a large area Au contact was deposited on the back of the p-Si substrate with a thickness of 100 nm. The top metal contacts were patterned with the help of a shadow mask and deposited by thermal evaporation in a high vacuum chamber under a pressure of  $10^{-6}$  torr. The I-V and C-V measurements were made at room temperature using a HP4155C semiconductor analyzer and a Keithley 590 CV analyzer at 100 KHz, respectively.



**Figure 5-5. Schematic of metal/ZnO-nanocomposite/p-Si structure used for electrical measurements at room temperature**

## 5.4 ELECTRICAL CHARACTERISTICS OF Al/n-ZnO-[PS]<sub>159</sub>[PAA]<sub>63</sub>/p-Si HETEROSTRUCTURE

### 5.4.1 Current-Voltage Characteristics

Au contacts on p-type Si were tested for ohmic resistivity and were ensured to be ohmic on p-Si as shown in the inset of fig. 5-6. For ohmic contacts, Al with a lower work function of ~4.2 eV compared to that of ZnO (~4.3-4.5 eV) [80] was used on the n-ZnO nanoparticles as also reported in the literature for ZnO films, nanowires, and nanorods [81]. The circular contact pads ( $0.00196 \text{ cm}^2$ ) covered an average of  $8 \times 10^4$  ZnO nanoparticles based on the density of the nanoparticles ( $4 \times 10^7 \text{ cm}^{-2}$ ) for the [PS]<sub>159</sub>/[PAA]<sub>63</sub> copolymer nanocomposite. Fig. 5-6 and fig. 5-7 shows the I-V and corresponding logI-V characteristics of Al/n-ZnO-[PS]<sub>159</sub>/[PAA]<sub>63</sub>-nanocomposite/p-Si heterostructure plotted on a linear and semilog scale, respectively. The I-V plots showed rectifying behavior with forward bias corresponding to positive voltage on Si substrate with respect to ZnO-nanocomposite film. Diode-like behavior was evident, with a good rectification ratio,  $I_F/I_R$ , defined as the ratio of the current at a large voltage  $V$  divided by the negative of the current at the corresponding negative potential  $-V$ , of  $3 \times 10^5$  at  $\pm 2V$ , a low leakage current of  $3 \times 10^{-9}$  A at  $V_r = -2V$  and no breakdown was evident for bias voltages up to 4V. It also showed a turn-on voltage of 0.56 V measured at a current of 1  $\mu$ A. The logI-V showed a linear region extending two orders of current magnitude over a bias of 0.5V to 1.4V. This exponential dependence of current on forward bias indicated possible



formation of heterojunction diodes between the distributed n-ZnO nanoparticles in the copolymer and the p-type Si substrate.

For confirming the contribution of ZnO nanoparticles in the formation of the distributed n-ZnO-nanocomposite/p-Si heterojunction diodes, I-V measurements were also performed on the copolymer without the ZnO nanoparticles. For this the undoped copolymer was spin-casted on Si, thinned down by ozone treatment to the same thickness of the ZnO-nanocomposite for direct comparison, and the same circular Al metal contacts were deposited as before. The ozone treated copolymer film thickness was found to be  $\sim 100 \text{ \AA}$ . The logI-V characteristics of the Al/copolymer/pSi structure presented in fig. 5-9 showed the characteristic behavior of a Si Metal Insulator Semiconductor (MIS) tunnel structure [82] with a symmetrical forward-reverse characteristic, and no evidence of linear region to show the exponential dependence of a diode current on forward bias voltage. LogI-logV plots for the Al/copolymer/pSi MIS structure showed a current-voltage power law dependence proportional to the square of the voltage ( $I \propto V^2$ ) as shown in fig. 5-9. This kind of dependence is generally attributed to space-charge limited current flow in insulators [82] without traps or filled traps, in this case the copolymer used as a template in the heterostructure. This shows that the incorporation of the ZnO nanoparticles in the copolymer results in the formation of a typical diode structure between the ZnO nanoparticles in copolymer and the Si substrate.

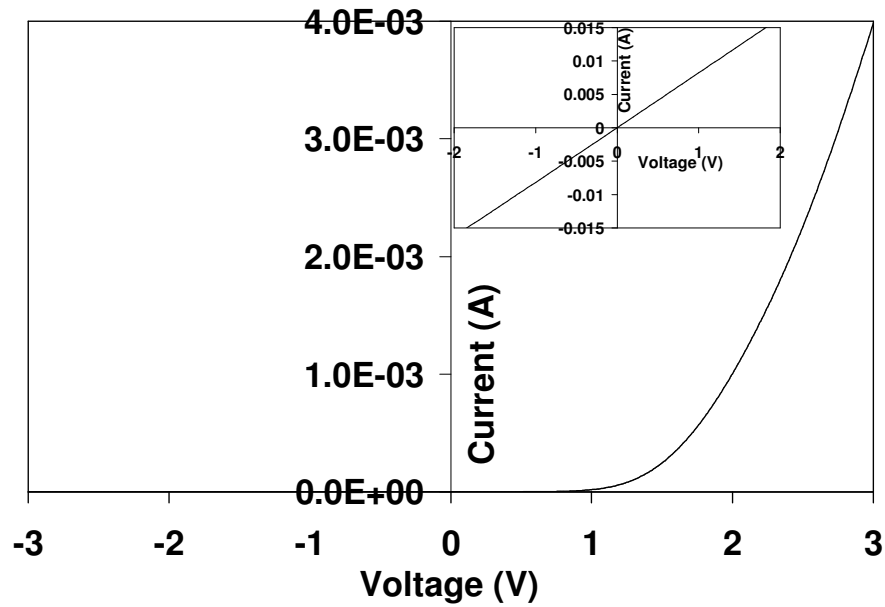


Figure 5-6. I-V plot of Al/n-ZnO-[PS]<sub>159</sub>/[PAA]<sub>63</sub>-nanocomposite/p-Si heterostructure measured at room temperature

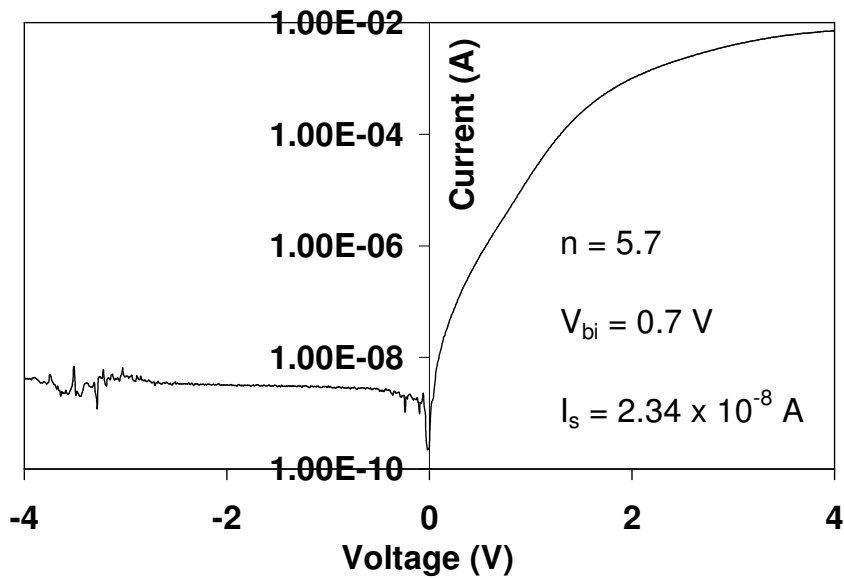


Figure 5-7. Log I-V plot corresponding to the I-V plot of Al/n-ZnO-[PS]<sub>159</sub>/[PAA]<sub>63</sub>-nanocomposite/p-Si heterostructure of fig. 5-6

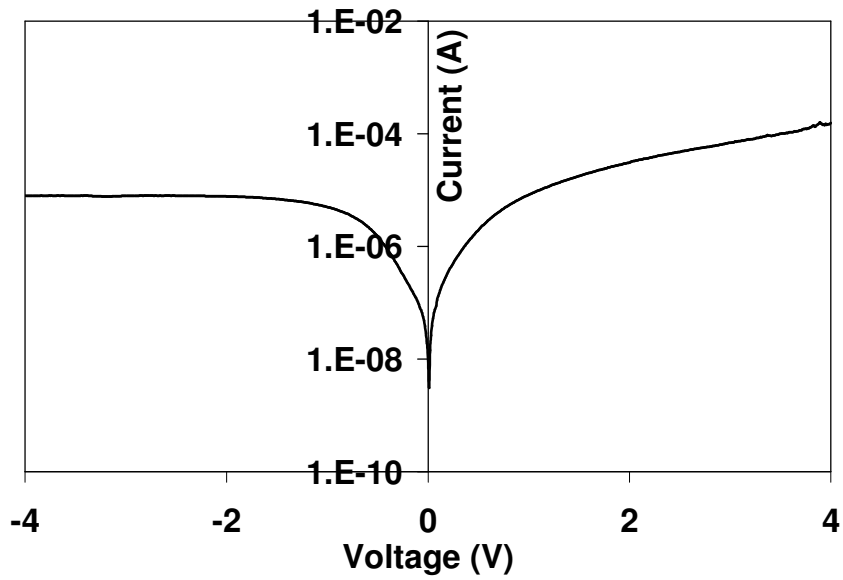


Figure 5-8. Log I-V plot of Al/[PS]<sub>159</sub>/[PAA]<sub>63</sub> copolymer/p-Si heterostructure

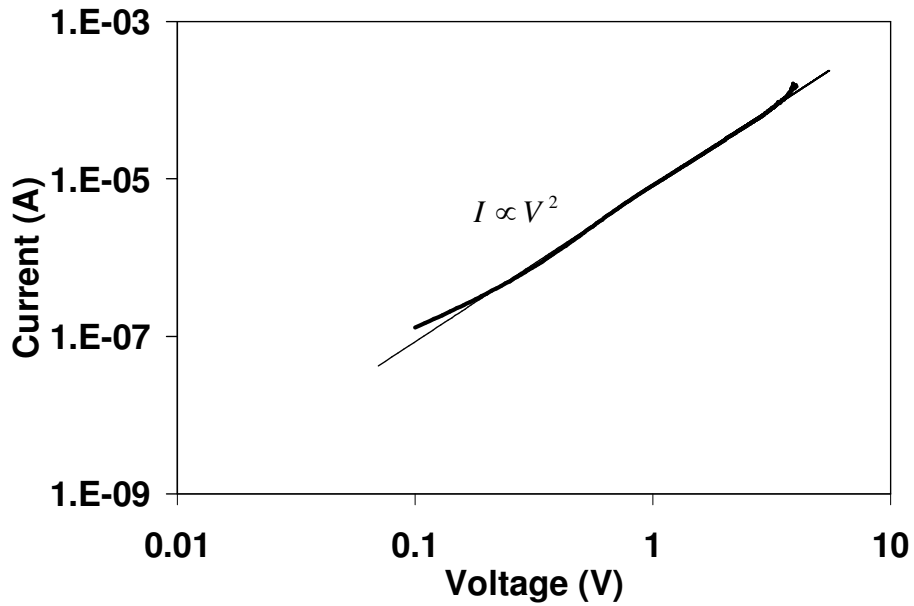
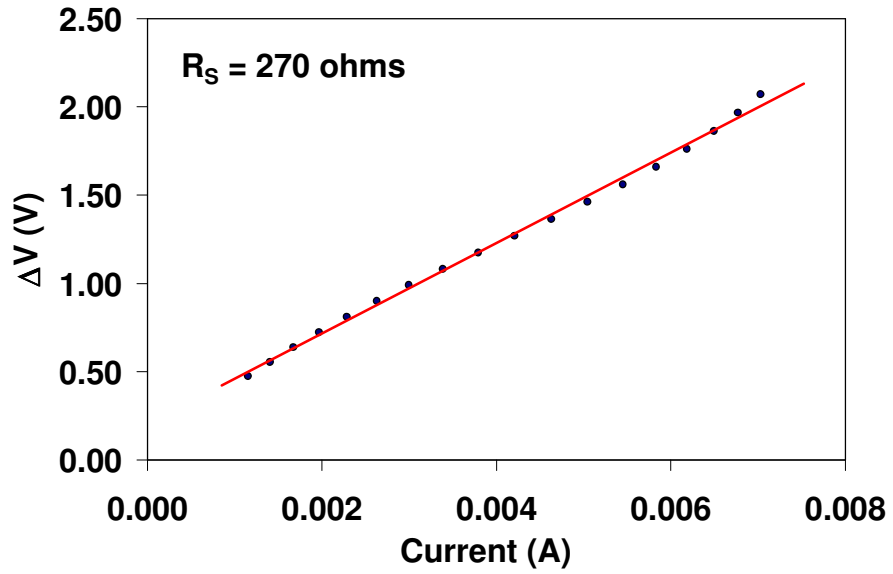


Figure 5-9. LogI-logV plot of Al/[PS]<sub>159</sub>/[PAA]<sub>63</sub> copolymer/p-Si heterostructure



**Figure 5-10. Series Resistance of Al/n-ZnO-[PS]<sub>159</sub>/[PAA]<sub>63</sub>-nanocomposite/p-Si heterostructure evaluated using  $\Delta V$ -I plot corresponding to the logI-V plot of fig. 5-7**

To evaluate the device characteristics and electronic transport mechanisms of the Al/ZnO-nanocomposite/Si heterojunction diode, equation (14),

$$I = I_s \left[ \exp\left(\frac{qV}{\eta kT}\right) \right] \dots\dots\dots (14)$$

was used to describe the diode current for  $V > 3kT/q$  and with series resistance neglected and the parameters were extracted from the logI-V characteristics of the diode (fig. 5-7) as discussed in §5.1.2. The intercept on current axis gave a saturation current,  $I_s = 2.34 \times 10^{-8}A$ , and the slope gave an ideality factor,  $\eta = 5.7$ . The reverse saturation current can be given according to thermionic emission transport as follows [82],

$$I_s = AT^2R^* \left[ \exp\left(-\frac{q\phi_b}{kT}\right) \right] \dots\dots\dots (15)$$

where, A is the area of the diode,  $R^*$  is the effective Richardson constant which for ZnO has a theoretical value of  $32 Acm^{-2}k^{-2}$  [83], T is the absolute temperature,  $\Phi_b$  is the built-in potential barrier at zero bias, q is the electronic charge, and k is the Boltzmann’s constant. From eq. 15 the built-in voltage was found to be 0.7 V. Series resistance for larger applied biases ( $V > 1.4V$ ), was measured as the current started to deviate from its exponential behavior. It was found to be 270 ohms as shown in fig. 5-10.

Since  $\eta > 2$  was obtained from the linear region of the logI-V characteristics of the heterojunction diode, carrier transport is not purely dominated by diffusion ( $\eta=1$ ) or thermionic emission ( $\eta=1$ ) or recombination in depletion region ( $\eta=2$ ) as in an ideal diode. Instead an enhanced form of recombination in the depletion region of

Si dominates the transport behavior with contributions from thermionic emission of carriers over the smaller band discontinuity ( $\Delta E_c$ ) before recombining in the depletion region or diffusing in the quasi neutral region of Si. This enhanced form of recombination in the depletion region of Si is induced by the abrupt nature of the junction and large valence band discontinuity (2.51 eV) compared to the conduction band discontinuity (0.3 eV) of the ZnO/Si heterojunction (fig. 5-11). Recombination in depletion regions of semiconductors with smaller bandgap in heterojunction diodes is the most accepted transport mechanism of heterojunctions with abrupt junction, and large difference in band discontinuities [84, 85, 86, 87, 88, 89]. Presence of interface states encourages even more significant recombination of carriers in depletion regions with negligible injection of minority carriers into quasi-neutral regions in such heterojunctions.

Fig. 5-11 helps illustrate the enhanced recombination process influencing the major current component of the ZnO-nanocomposite/Si heterojunction diode at intermediate forward bias. Fig. 5-11 shows the proposed energy band diagram of an abrupt ZnO/Si heterojunction under forward bias, with interface states neglected. As seen from the figure, the carrier flow in this bias region is largely by electrons from ZnO to Si and hole injection is negligible from Si to ZnO as the energy barrier for electrons is much lower than that for holes due to  $\Delta E_c < \Delta E_v$  (0.3 < 2.51 eV). Thus the large  $\Delta E_v$  creates a bottleneck for hole injection from Si to ZnO under forward bias. As a result, holes are present at the depletion region for a considerable period of time before being injected into ZnO or being swept back to Si by the built-in electric

field. This encourages recombination of the holes in the depletion region on Si side with the electrons passing the depletion region before being injected into the quasi-neutral region of Si. The recombination process could be direct band-to-band recombination or via recombination centers in the depletion region. These centers can be from interface states due to defects at the junction from lattice mismatch between the semiconductors or process-induced defects at the interface [74, 89].

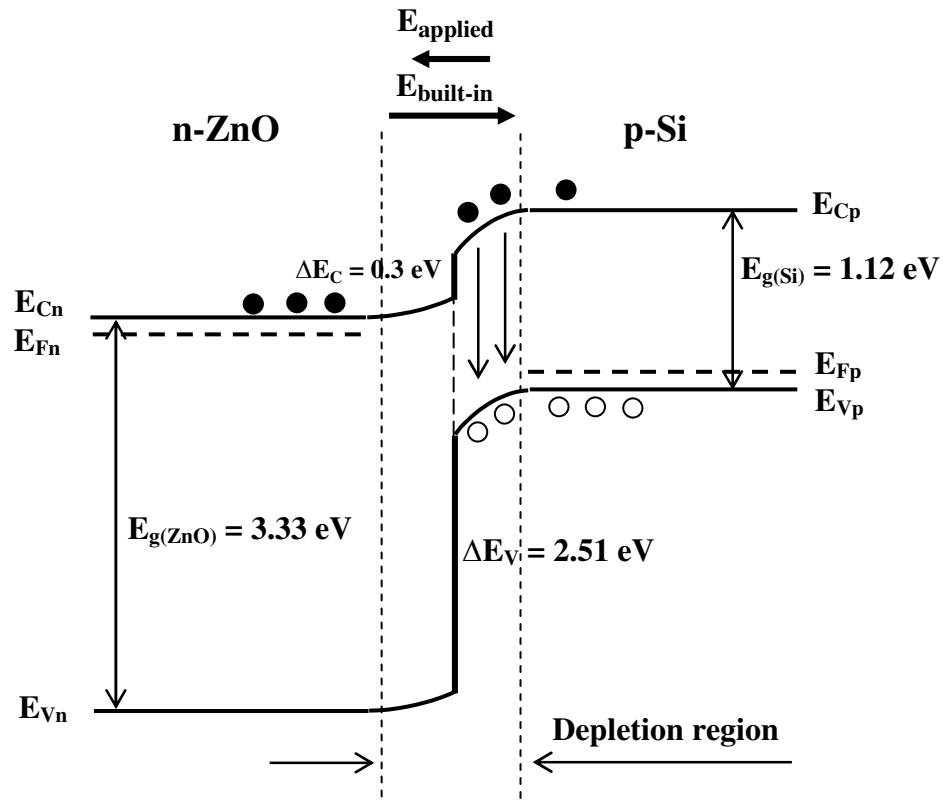


**Figure 5-11. Energy band diagram of an abrupt ZnO/Si heterojunction under forward bias (holes are represented by ○ and electrons are represented by ●)**

Another possible dominant transport mechanism that has been reported to account for large ideality factors found in heterojunction diodes with differences in band discontinuities is a recombination-tunneling mechanism based on the Riben and Feucht model [96]. This mechanism involves tunneling of carrier into interface states instead of injection of carriers over band discontinuity to recombine with carriers in depletion region or energy bands. This model best fits heterojunctions with large density of interface states and heavily doped semiconductors which increases the probability of tunneling into the interface states for recombination [90, 91, 92, 93, 94, 95]. This model of recombination-tunneling current transport mechanism in heterojunctions was proposed by Riben and Feucht [96, 97] based on tunnel diode excess current model [82] involving multi-step tunneling and trap-assisted recombination in energy band gap where the current-voltage relation is ruled by,

$$I \propto \exp(\alpha V) \dots\dots\dots (16)$$

where V is the applied bias and  $\alpha$  is a constant given by,

$$\alpha = (8\pi / 3h)(m^* \epsilon_s)^{1/2} N_D / [N_A^{1/2} (N_A + N_D)] \dots\dots\dots (17)$$

where,  $h$  is Plank's constant,  $m^*$  is the carrier effective mass of semiconductor with wider band gap,  $\epsilon_s$  is the dielectric constant of semiconductor with wider band gap,  $N_D$  is donor concentration, and  $N_A$  is the acceptor concentration. According to the Riben and Feucht model, this mechanism dominates over other conduction mechanisms at lower voltages due to band discontinuities present in heterojunctions which create barriers for carrier diffusion. The interface states which act as recombination centers help provide the tunneling-recombination path for band-to-



band tunneling in these heterojunctions. The lattice defects that are usually created at the interface of heterostructures employing wide bandgap semiconductors to compensate for the lattice mismatch between the two materials of heterostructures are primary reasons for the presence of these interface states. Thus, in the case of a p-n heterojunction with  $\Delta E_C < \Delta E_V$  like our diodes, main conduction at lower voltages has been attributed to electrons tunneling from the conduction band of the n-type material into recombination centers provided by interface states and subsequently recombining with holes in the valence band of the p-type material.

So to examine if the model could be applied to explain the large ideality factor due to dominant recombination-tunneling transport mechanism in the diode,  $\log I - \log V$  (fig. 5-12) was plotted for the exponential region of the I-V characteristics ( $0.5 \text{ V} < V < 1.4 \text{ V}$ ) in fig. 5-6 and the value of  $\alpha$  extracted. The value was found to be  $6.34 \text{ V}^{-1}$  and using the expression of  $\alpha$  in equation (17), and reported values of  $m^*$  and dielectric constant of ZnO, the donor concentration ( $N_D$ ) of ZnO was calculated to be  $4 \times 10^{12} \text{ cm}^{-3}$ . This value is three orders of magnitude smaller than that obtained from C-V measurements of the heterojunction diode (§5.4.2). This strongly suggests that recombination-tunneling is not the limiting current transport mechanism in this voltage range for the ZnO-nanocomposite/Si heterojunction diode. This can be due to the low density of interface states in the heterojunction predicted from the C-V characteristics that showed an abrupt junction suggesting an intimate junction interface consistent with the pseudo-epitaxial nature of the ZnO nanostructure on Si evaluated from the XRD studies. The low doping concentrations measured for ZnO and Si also lowers the probability of carrier tunneling. Thus for our heterojunction

diode, enhanced recombination in the depletion region as described earlier can be expected to influence the major diode current component with minor contributions from injection current and tunneling current

Besides recombination in the depletion region, defects at the interface between the ZnO nanoparticles and the copolymer matrix, surface states due to unsaturated bonds, and contact resistivity are some of the effects that can be responsible for reduced forward current at the applied voltage, thus resulting in a larger ideality factor of the heterojunction diode.

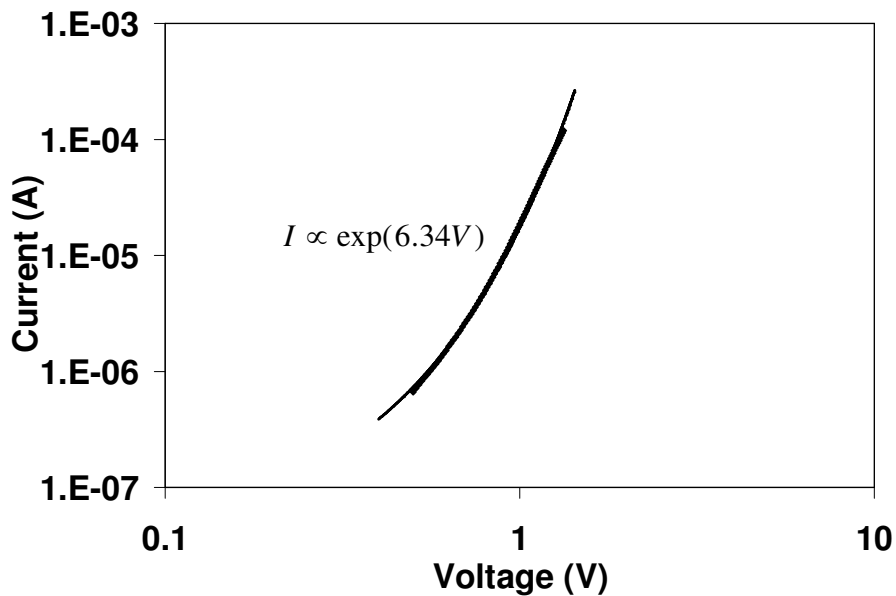


**Figure 5-12. Log I-logV plot corresponding to the linear region of the logI-V plot of Al/n-ZnO-[PS]<sub>159</sub>/[PAA]<sub>63</sub>-nanocomposite/p-Si heterostructure of fig. 5-7. The thick line is experimental plot and thin line is fitted plot.**

In the region below 0.5 V of the logI-V plot, current-voltage exponential relation was not observed. Instead, a power law dependence of current on the applied voltage,  $I \propto V^3$  was observed. This was found from the logI-logV characteristics of the Al/n-ZnO-[PS]<sub>159</sub>/[PAA]<sub>63</sub>-nanocomposite/p-Si heterojunction in the bias region of  $0.2 \text{ V} > V > 0.5 \text{ V}$ , as shown in fig. 5-13. The  $I \propto V^3$  dependence is attributed to current transport through MIS structures with traps. This suggests that the carrier transport through the heterojunction at this low bias region is dominated by the metal/copolymer/Si junction (fig. 5-5). This kind of transport was observed earlier in the Al/copolymer/Si structure in fig. 5-9. The power law dependence observed in that structure was attributed to transport through insulator without traps but in this heterojunction the traps are most likely from defects at the interface between the copolymer matrix and ZnO nanoparticles.

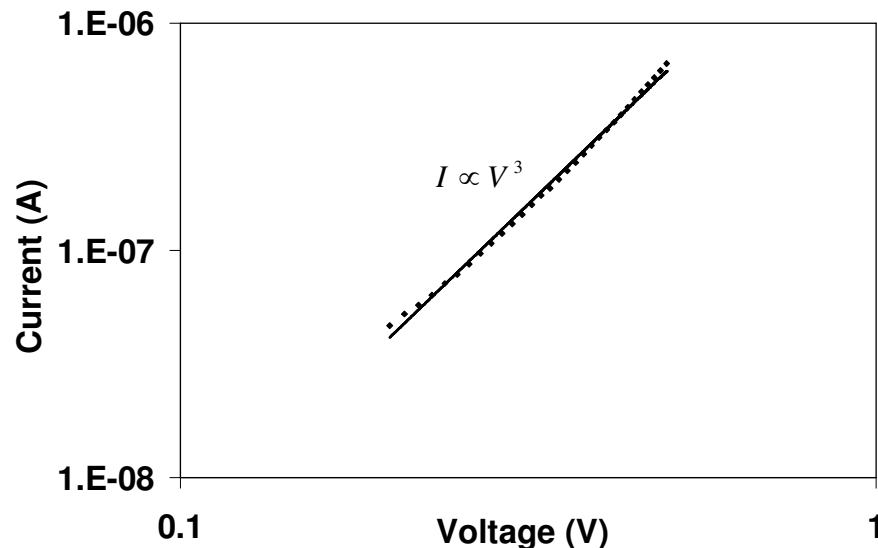


**Figure 5-13. LogI-logV characteristics of Al/n-ZnO-[PS]<sub>159</sub>/[PAA]<sub>63</sub>-nanocomposite/p-Si heterostructure at low bias region, below  $0.3 \text{ V} > V > 0.5 \text{ V}$ .**

In the bias region above 1.4 V, we observed the heterojunction diode current to deviate from its exponential relation due to series resistance effect. The I-V characteristics plot of the heterojunction was corrected for series resistance effect. Fig. 5-14 shows the semilog plot of the diode current and junction voltage ( $\log I-V_j$ ) after  $R_s$  correction of the diode. This showed that the current still behaved exponentially with the junction voltage but the ideality factor had increased from 5.7 ( $0.5V > V > 1.4V$ ) to 7.9 ( $V > 1.4 V$ ). This can be attributed to higher injection of carriers limiting the current transport in this bias region.

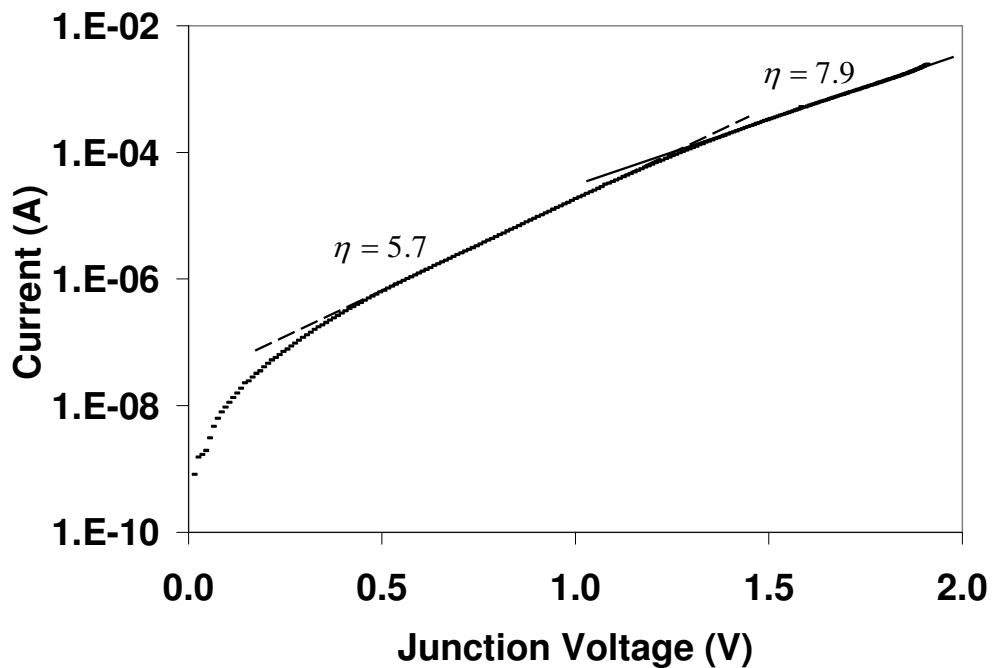


**Figure 5-14. Log I- $V_j$  plot corresponding to the I-V plot of Al/n-ZnO-[PS]<sub>159</sub>/[PAA]<sub>63</sub>-nanocomposite/p-Si heterostructure of fig. 5-6 after series resistance ( $R_s$ ) correction.**

### 5.4.2 Capacitance-Voltage Characteristics

The C-V analysis was also used to examine the junction properties of the Al/ZnO-[PS]<sub>159</sub>/[PAA]<sub>63</sub>-nanocomposite/p-Si heterojunction. The capacitance was measured with varied bias (-2 to 2 V) applied to p-Si substrate with respect to ZnO nanocomposite film at 100 kHz. As shown in fig. 5-15 decreasing capacitance was observed with increasing negative bias on p-Si substrate with respect to ZnO, indicating reverse biased p-n heterojunction with the ZnO nanoparticles unintentionally doped n-type.

Fig. 5-16 shows the  $1/C^2$ -V plot of the heterojunction. The plot exhibited a linear region indicating an abrupt heterojunction. Using a linear least-square fitting on the linear portion of the  $1/C^2$ -V plot, built-in or diffusion voltage extracted from the intercept on the voltage axis was found to be 0.75 V which is in very good agreement with the built-in voltage extracted from the I-V measurements of the heterojunction diode. The characteristics here confirm that an abrupt heterojunction is formed between the nanostructured ZnO and Si with well behaved n-p junction characteristics. The donor concentration of the unintentionally doped ZnO nanoparticles extracted from the slope of the plot as described in §5.1.2 was found to be  $3 \times 10^{15} \text{ cm}^{-3}$ . The built-in voltage calculated from the proposed energy band diagram using this extracted donor concentration was found to be 0.4 eV (calculation shown in §5.2). This value is quite small than that extracted from both C-V and I-V measurements. This could be due to lower donor density obtained from using the metal contact area instead of the effective area of the nano-junction diodes for donor density ( $N_D$ ) calculation (§5.1.2).

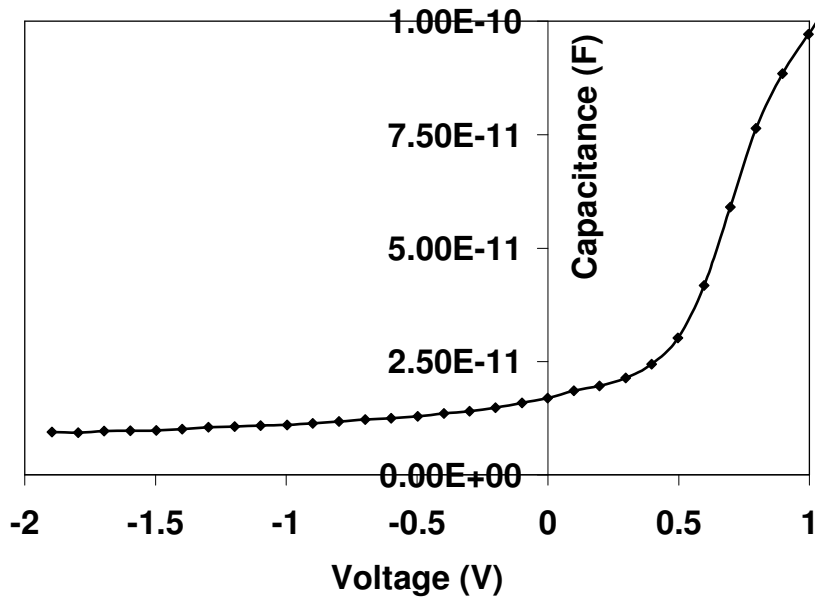


Figure 5-15. C-V plot of Al/n-ZnO-[PS]<sub>159</sub>/[PAA]<sub>63</sub>-nanocomposite/p-Si heterostructure measured at 100 kHz at room temperature

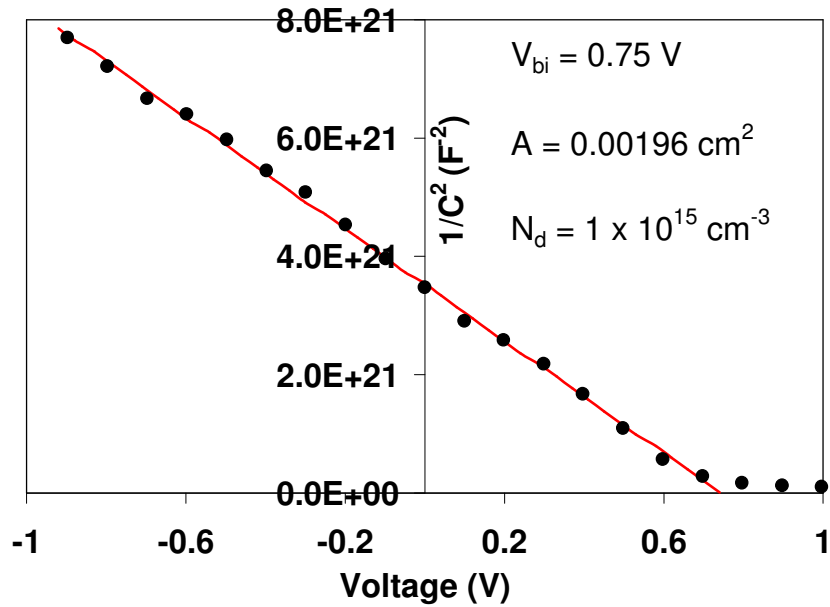


Figure 5-16.  $1/C^2$ -V plot of Au/n-ZnO-[PS]<sub>159</sub>/[PAA]<sub>63</sub>-nanocomposite/p-Si heterostructure corresponding to the C-V plot in fig. 5-15

## 5.5 ELECTRICAL CHARACTERISTICS OF Au/n-ZnO-[PS]<sub>159</sub>[PAA]<sub>63</sub>/p-Si HETEROSTRUCTURE

The electrical characteristics of the n-ZnO-[PS]<sub>159</sub>[PAA]<sub>63</sub>/p-Si heterostructure discussed in an earlier section were studied with Au electrode on the ZnO-nanocomposite film on p-Si. Fig. 5-17 and fig. 5-18 shows the I-V and corresponding logI-V plot of Au/ZnO-[PS]<sub>159</sub>[PAA]<sub>63</sub>/pSi structure, respectively. The plots showed similar rectifying behavior as observed for the structures with Al top electrode in the previous section. The forward bias of the I-V measurements corresponded to positive voltage on Si substrate with respect to ZnO-nanocomposite film. Diode-like behavior was evident, with a rectification ratio of  $10^3$  at  $\pm 2V$  and a leakage current of  $1 \times 10^{-7}$  A at  $V_r = -2V$ . The logI-V showed a linear region extending two orders of current magnitude over a bias of 1.15V to 2.5V. The diode parameters extracted from the linear region in the logI-V plot gave a saturation current of  $2.85 \times 10^{-7}$  A, a built-in voltage of 0.62 eV, and an ideality factor of 13.5. The series resistance was calculated for the bias region,  $V > 2.5$  V, where the current showed deviation from its exponential behavior and was found to be 280 ohms.

Since the same heterostructure as the earlier discussed Al/ZnO-nanocomposite/pSi heterojunction diode was used to develop this diode but with Au contacts, the dominant transport mechanisms are the same at different bias regions. However, deviations in ideality factors and dominant bias regions were observed in this diode from the diode with Al contacts. These deviations can be attributed to the non-linear characteristics of the Au and ZnO-nanocomposite junction as most often Au has been used to form schottky contacts on ZnO [71]. This effect was proposed by

Shah et. al. [98] to account for large ideality factors observed in p-n junctions (homojunction or heterojunction) with small tunneling effects. This theory has been used for other ZnO based heterojunctions to account for large ideality factors [99, 100]. According to this theory, each metal-semiconductor junction behaves as a leaky reverse biased schottky diode during forward bias of the actual p-n junction and each junction can be represented by its own diode equation with ideality factor and saturation current. The I-V characteristics of the diode structure was then given by,

$$\ln I = \frac{(q/kT)}{\sum_i n_i} V + \frac{\sum_i n_i \ln I_{S_i}}{\sum_i n_i} \dots\dots\dots (18)$$

where, all symbols have their usual meaning. Thus according to Eq. (18) the measured ideality factor of the diode is a summation of the ideality factors of the individual junctions which accounts for the increased  $\eta$  value in the diodes.

According to this theory, the Au/ZnO-nanocomposite/Si heterojunction diode can be modeled as a Au/ZnO schottky diode and a ZnO/Si n-p diode connected back to back in series for applied bias corresponding to the linear region of the logI-V characteristics of the diode. The Au/copolymer/Si junction is neglected in this model as the diode transport is dominated by the n-p junction in this bias region. Thus, the schottky diode is reverse biased during forward bias of the ZnO/Si diode and vice versa. Since in our study, n-p heterojunction diodes were obtained with both types of top metal contacts on ZnO it can be understood that the Au contacts formed poor rectifying schottky contacts on ZnO-nanocomposite film. This could be due to poor metal-semiconductor interface from the non-uniform surface morphology of the nanocomposite film which would result in interface states and large leakage currents.



ZnO is known to have high density of unsaturated surface bonds and presence of surface states would also result in poor schottky contacts. Even though the schottky junction was not rectifying due to its leaky nature, the junction provided a highly resistive path for current transport in the actual n-p diode under forward biased. As a result, the exponential current transport through the Au/ZnO-nanocomposite/Si heterojunction was observed at a higher bias ( $V > 1.15$  V) with a lower forward current density than the diode with Al contacts ( $V > 0.5$  V).

LogI-logV plot corresponding to the I-V characteristics of the Au/ZnO-[PS]<sub>159</sub>[PAA]<sub>63</sub>/pSi structure was examined for bias region  $V < 1.15$  V where current-voltage did not show any exponential dependence. The plot was found to be best fitted by a power law function as shown in fig. 5-19. This indicates that the current transport in this bias region was mainly through the MIS (metal/copolymer/Si) structures as the  $I \propto V^3$  relation is attributed to transport through metal/insulator having interface states. Thus due to the non-linear characteristics of the Au contacts, the transport through the MIS structures dominated for bias higher than the diode with ohmic Al contacts.

The bias region,  $V > 2.5$  V, where the I-V relation showed deviation from its exponential dependence was examined after series resistance correction of the I-V plot of fig. 5-17 for 280 ohms. The corrected logI-V plot (fig. 5-20) showed a second linear region that was earlier masked by series resistance effects. The ideality factor obtained for this region decreased to 10 from 13.5 of bias region,  $1.15V < V < 2.5V$ . This region is expected to be the high injection region of the diode as observed from the Al/ZnO-[PS]<sub>159</sub>[PAA]<sub>63</sub>/p-Si structure and ideally a drop in forward current is

observed with a decrease in ideality factor. Instead an increase in current and ideality factor was observed due to increased leakage current across the Au/ZnO-nanocomposite interface at higher bias.

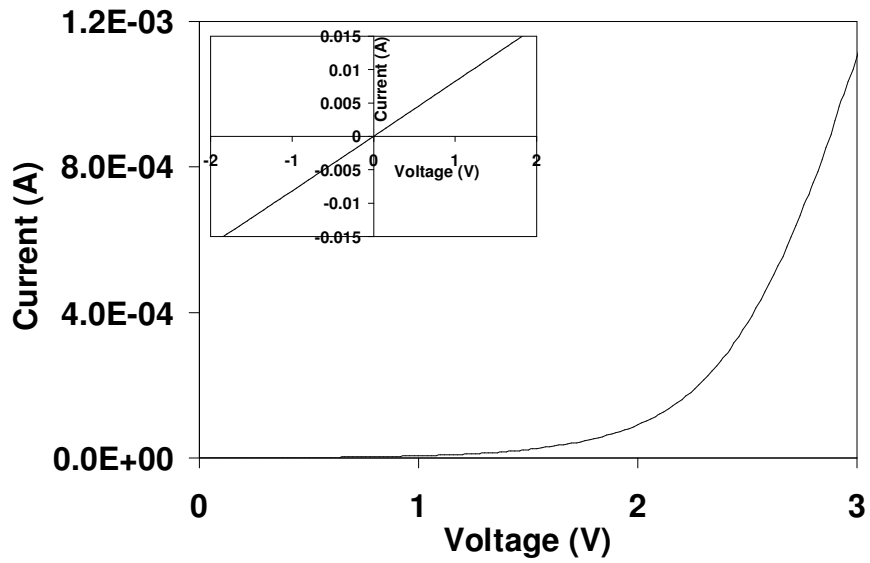


Figure 5-17. I-V plot of Au/n-ZnO-[PS]<sub>159</sub>/[PAA]<sub>63</sub>-nanocomposite/p-Si heterostructure measured at room temperature

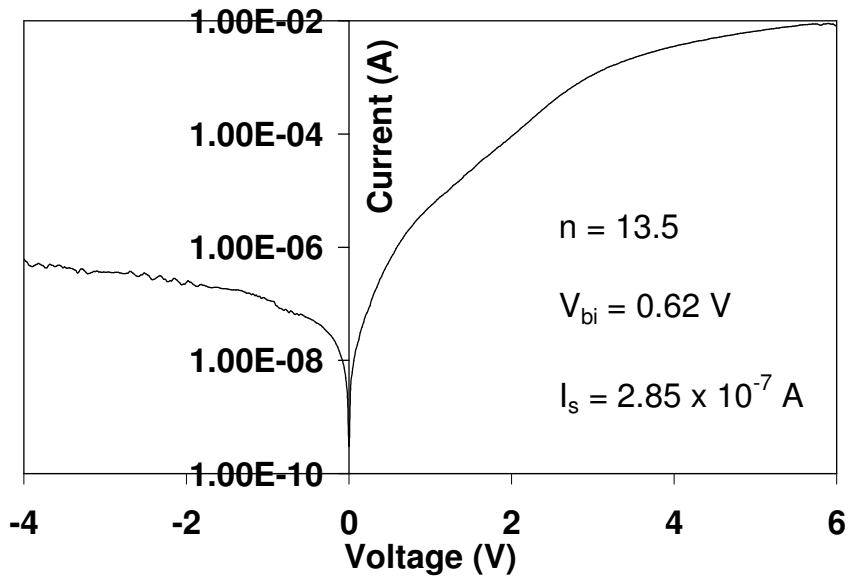


Figure 5-18. Log I-V plot corresponding to the I-V plot of Au/n-ZnO-[PS]<sub>159</sub>/[PAA]<sub>63</sub>-nanocomposite/p-Si heterostructure of fig. 5-17

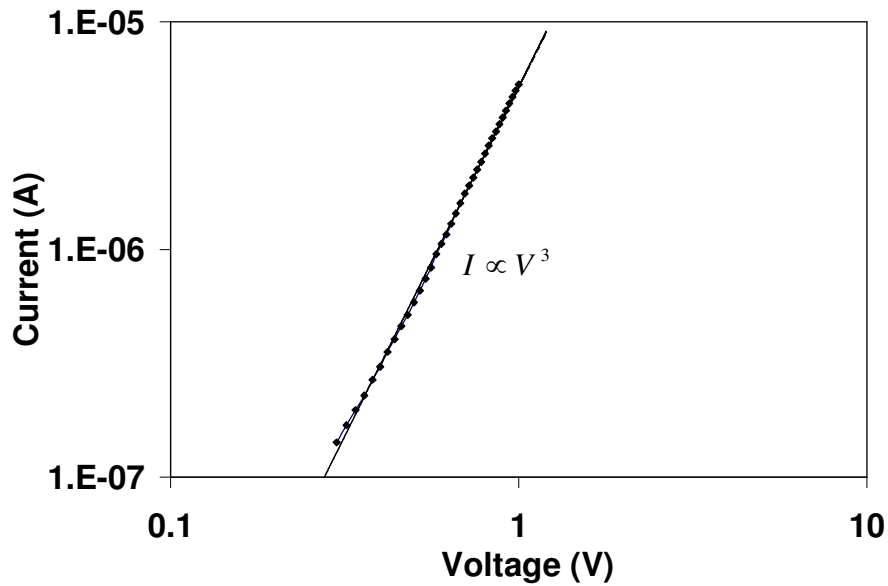


Figure 5-19. LogI-logV characteristics of Au/n-ZnO-[PS]<sub>159</sub>/[PAA]<sub>63</sub>-nanocomposite/p-Si heterostructure at low bias region,  $0.3 \text{ V} > V > 1.0 \text{ V}$ .

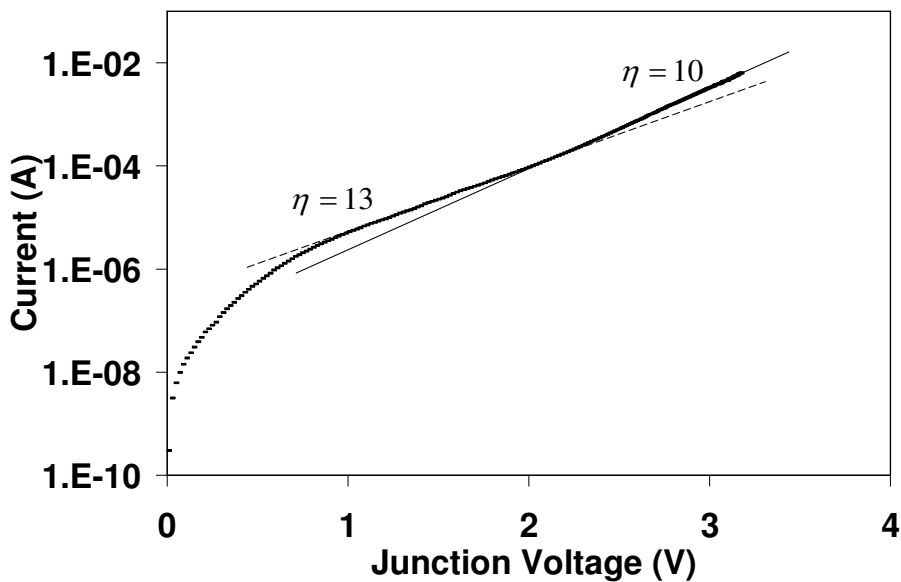


Figure 5-20. Log I- $V_j$  plot corresponding to the I-V plot of Au /n-ZnO-[PS]<sub>159</sub>/[PAA]<sub>63</sub>-nanocomposite/p-Si heterostructure of fig. 5-17 after series resistance ( $R_s$ ) correction

## 5.6 ELECTRICAL CHARACTERISTICS OF Au/n-ZnO-[PS]<sub>106</sub>[PAA]<sub>4</sub>/p-Si HETEROSTRUCTURE

The electrical characteristics of the smaller and denser ZnO nanoparticles in copolymer on Si were also examined. For this purpose, the n-ZnO-[PS]<sub>106</sub>[PAA]<sub>4</sub>/p-Si heterostructure was developed in a similar manner as the previous structures with Au top electrode. The circular contact pads (0.00196 cm<sup>2</sup>) covered an average of  $2 \times 10^7$  ZnO nanoparticles based on the density of the nanoparticles ( $1 \times 10^{10}$  cm<sup>-2</sup>) for the [PS]<sub>106</sub>[PAA]<sub>4</sub> copolymer nanocomposite. Fig. 5-21 and fig. 5-22 shows the I-V and its corresponding logI-V characteristics of Al/n-ZnO-[PS]<sub>106</sub>[PAA]<sub>4</sub>-nanocomposite/p-Si heterostructure plotted on a linear and semilog scale, respectively. The I-V plots showed rectifying behavior with forward bias corresponding to positive voltage on Si substrate with respect to ZnO-nanocomposite film. Diode-like behavior was evident, with a good rectification ratio,  $I_F/I_R$ , of  $10^3$  at  $\pm 2$ V, and no breakdown was evident for bias voltages up to 3V. The logI-V showed a linear region extending two orders of current magnitude over a bias of 0.2V to 1.0V. The diode parameters extracted from the linear region in the logI-V plot gave a saturation current of  $2 \times 10^{-8}$ A, a built-in voltage of 0.69 eV, and an ideality factor of 5.9. These diode parameters were comparable to those obtained with Al contacts on the larger nanoparticles. The ideality factor was not as large as that with Au contacts on the larger particle system. This is because of the enhanced tunneling effects across smaller metal-semiconductor interfaces [101] which resulted in a pseudo-ohmic behavior of the Au contacts and reduced the non-linear effects of the Au/ZnO junction on the transport properties of the diode as discussed in the earlier section.

Fig. 5-23 shows the  $\log I$ - $\log V$  plot corresponding to the I-V plot of fig. 5-21 in bias region  $0.2 \text{ V} < V < 2 \text{ V}$ . The plot showed two distinct regions that could be best fitted to an exponential function ( $0.2 \text{ V} < V < 1 \text{ V}$ ) and a power-law function ( $1 \text{ V} < V < 2 \text{ V}$ ). The exponential I-V relation observed below 1 V and the ideality factor ( $\eta=5.9$ ) obtained indicates dominant carrier transport through recombination of carriers in depletion region similar to that observed in the diodes with the larger nanoparticles. Above 1V, the diode current follows a power-law dependence on the applied voltage that can be explained by the space charge limited conduction (SCLC) model developed by Lampert and Mark [102] based on current transport in insulators. Such space charge limited conduction at high injection levels have been observed in other ZnO based heterojunctions [103, 104].

This model was developed for wide band gap heterojunction diodes with unequal band discontinuities which induces single carrier injection over the smaller band discontinuity until both electron and hole flows under forward bias. At low bias, the injected carrier over the smaller band discontinuity either recombines in depletion region or quasi neutral region and the carrier transport is limited by recombination or diffusion process. However, the injection rate is higher than diffusion rate at high injection levels and the injected carrier density becomes greater than the majority carrier density of the injected semiconductor. As a result, the injected minority carriers accumulate near the depletion region of the injected semiconductor which creates a space charge region. This space charge region is balanced by a widening of the depletion region of the single carrier injecting semiconductor for charge conservation in the diode. Thus further injection of carriers across the smaller band

discontinuity is impeded and the current transport becomes limited by the space charge region created and the widening of the depletion region. This transport is called the space charge limited conduction and the diode current is termed the space charge limited current. The space charge limited current exhibits power law dependence on applied voltage,  $I \propto V^m$  where  $m$  depends on bias and distribution of trapping centers. For conduction through a space charge limited region without traps, current shows a power law dependence with  $m = 2$  and with traps  $m > 2$ .

Thus the SCLC model can be applied to predict the diode current transport behavior in the region,  $1 \text{ V} < V < 2 \text{ V}$ , where the current-voltage was found to obey a power law relation of  $I \propto V^{3.6}$ . This suggests that the diode transport becomes space charge limited above a bias of 1 V due to higher injection rate of electrons from ZnO into the quasi-neutral region of Si than recombination rate in the depletion region. The current transport is limited by the negatively charged region of excess electrons formed in Si and the wider depletion region formed on the ZnO side to compensate for the excess charge in Si. The power law relation with  $m > 2$  obtained also suggests current transport in the presence of traps. This SCLC mechanism is expected to prevail until hole injection starts in the diode.

The space charge limited conduction at high injection levels was not observed in the larger diodes, instead the current showed exponential behavior. Whereas, the smaller diodes showed space charge limited conduction at the high injection region. This is due to the larger bandgap (3.43 eV) of the smaller nanoparticles as calculated from the PL measurements (§4.3.2) which resulted in the larger  $\Delta E_v$  of the smaller

diodes by 0.1 eV than that of the larger diodes. This allowed hole injection in the larger diodes at a lower bias than the smaller diodes. Another interesting observation made from comparing the I-V characteristics of the larger and smaller diodes was the absence of dominant conduction through the metal/copolymer/Si junction in the lower voltages observed in the larger diode. This is due to the highly dense nanoparticles forming the smaller diodes.



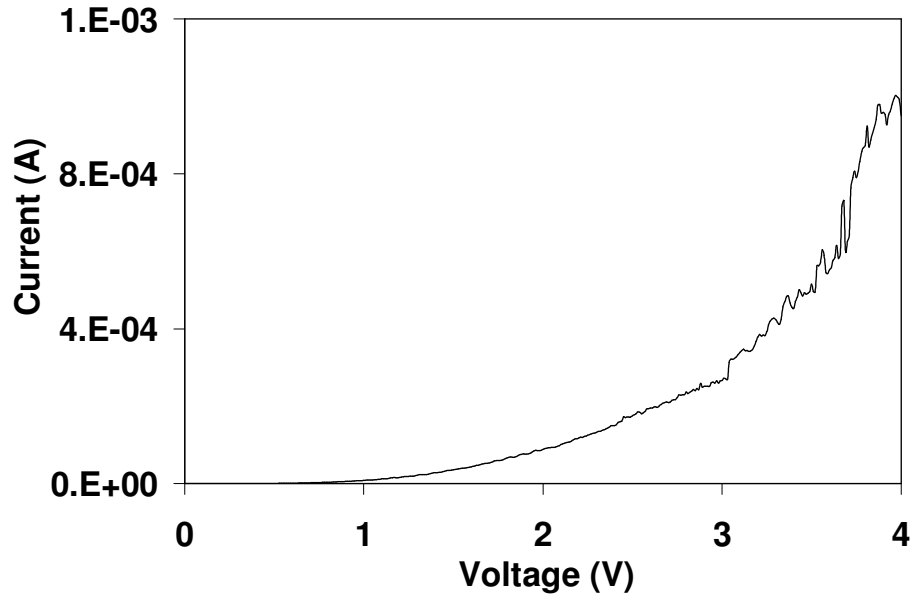


Figure 5-21. I-V plot of Au/n-ZnO-[PS]<sub>106</sub>/[PAA]<sub>4</sub>-nanocomposite/p-Si heterostructure measured at room temperature

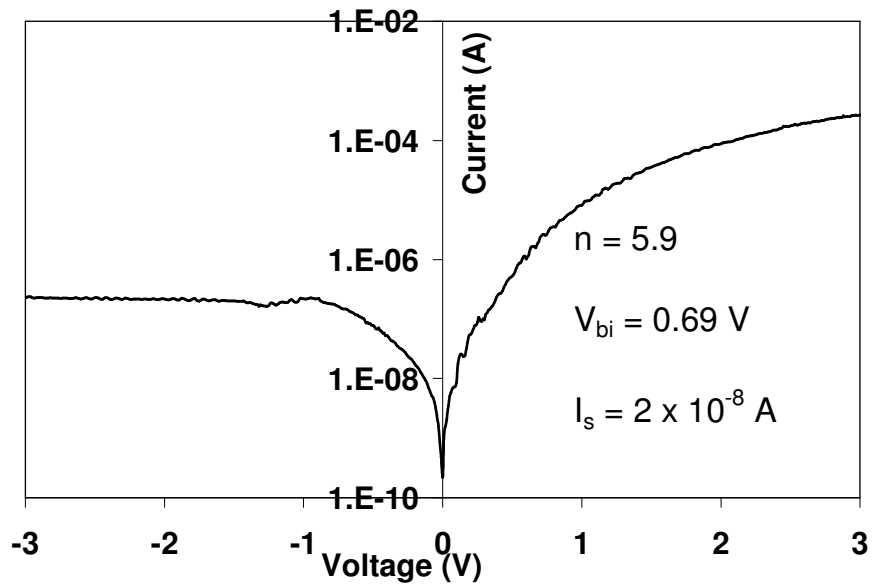
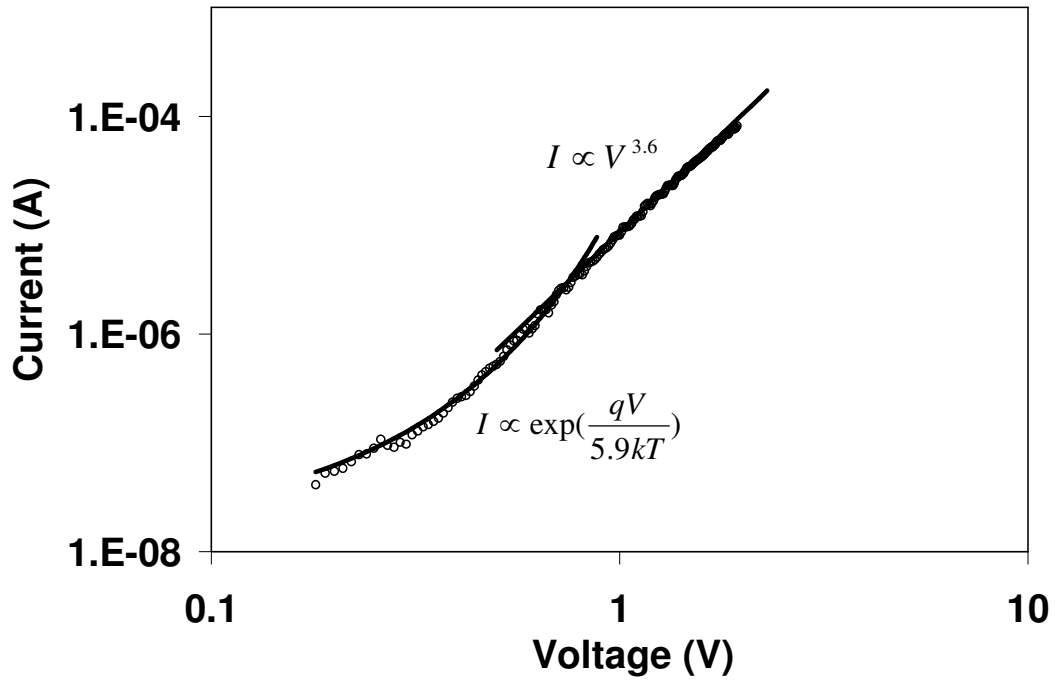


Figure 5-22. Log I-V plot corresponding to the I-V plot of Au/n-ZnO-[PS]<sub>106</sub>/[PAA]<sub>4</sub>-nanocomposite/p-Si heterostructure of fig. 5-21



**Figure 5-23. LogI-logV characteristics of Au/n-ZnO-[PS]<sub>106</sub>/[PAA]<sub>4</sub>-nanocomposite/p-Si heterostructure showing bias dependent current-voltage relation at bias regions of 0.2 V >V>1 V (exponential behavior) and 1V>V>2V (power-law behavior)**

	<b>Diode with the 250 nm sized ZnO nanoparticles</b>	<b>Diode with the 250 nm sized ZnO nanoparticles</b>	<b>Diode with the 20 nm sized ZnO nanoparticles</b>
Top electrode	<b>Al</b>	<b>Au</b>	<b>Au</b>
Metal work function, $\chi_m$	4.2 eV	5.2 eV	5.2 eV
Ideality factor, $\eta$	5.7	13.5	5.9
Saturation current, $I_s$	$2.34 \times 10^{-8}$ A	$2.85 \times 10^{-7}$ A	$2 \times 10^{-8}$ A
Built-in voltage, $V_{bi}$	0.7 V	0.62 V	0.69 V
Linear region of log I-V	0.5 – 1.4 V Dominant transport is recombination in depletion region on Si side of diode	1.15 – 2.80 V Dominant transport is recombination in depletion region on Si side of diode	0.2 – 1.0 V Dominant transport is recombination in depletion region on Si side of diode
Below linear region of log I-V	0.3 – 0.5 V Dominant transport is SCLC through MIS structure of diode	0.3 – 1.0 V Dominant transport is SCLC through MIS structure of diode	—
Above linear region of log I-V	$\eta = 7.9$ Higher injection effects observed	$\eta = 10.0$ Higher injection effects observed	1 – 2 V Dominant transport is SCLC due to larger $\Delta E_V$

**Table 1. Summary of the electrical characteristics of the nanodiodes**

## 5.7 SUMMARY

This chapter discusses the development and electrical characterization of heterojunction diodes with ZnO nanoparticles in copolymer on p-Si. The heterostructures were developed with ZnO-nanocomposite films on Si substrate with metal contacts deposited on film. The electrical properties were studied for both the 250 nm and 20 nm ZnO nanoparticles and for Al and Au contacts on ZnO-nanocomposites.

The Al/250nm-ZnO-nanocomposite/Si heterostructure showed rectifying properties with saturation current of  $3 \times 10^{-8}$  A, a built-in voltage of 0.7 eV, and an ideality factor of 5.7. In the bias region  $0.3\text{V} < V < 0.5\text{V}$ , conduction was mainly through the metal/copolymer/Si, in  $0.5\text{V} < V < 1.4\text{V}$  enhanced recombination in depletion region induced by  $\Delta E_v \gg \Delta E_c$  dominates current transport and in  $V > 1.4\text{V}$  high injection of carriers was observed with increase in ideality factor to 7.9. C-V measurements indicated an abrupt n-ZnO/p-Si junction with built-in voltage of 0.75 V in good agreement with that measured from I-V measurements and donor concentration of  $3 \times 10^{15} \text{ cm}^{-3}$  in ZnO nanoparticles.

The Au/250nm-ZnO-nanocomposite/Si heterostructure also showed rectifying properties but with a lower saturation current of  $2.85 \times 10^{-7}$  A, a built-in voltage of 0.62 eV, and a higher ideality factor of 13.5 compared to the above heterostructure. This is believed to be due to non-linear characteristics of the Au/ZnO junction which acts as a highly resistive contact for the diode current. This resulted in the exponential current behavior to be observed at a higher bias ( $V > 1\text{V}$ ) than the structure with Al contacts ( $V > 0.5\text{V}$ ). Below 1V bias, major current transport was found to be

dominated by the metal/copolymer/Si junction and above 1V bias enhanced recombination in depletion region influenced the diode current.

Finally, the heterostructure with smaller and denser ZnO nanoparticles was studied. These also showed rectifying diode properties with saturation current of  $2 \times 10^{-8}$  A, a built-in voltage of 0.69 eV, and an ideality factor of 5.9. The carrier transport in this diode was dominated by enhanced recombination like the diodes with the larger nanoparticles at bias below 1V. Transport through the metal/copolymer/Si junction was not observed at low bias as a result of the increased density of the nanoparticles in this diode. As a consequence of the larger band gap than the 250 nm nanoparticles, space charge limited current (SCLC) is the major current component of the diode in the bias region  $1V > V > 2V$  which was not observed in the diode with the larger ZnO nanoparticles.

## **CHAPTER 6**

### **DEVELOPMENT OF HIGH PERFORMANCE ZnO GAS NANO-SENSOR DEVICES**

This chapter presents the development of room temperature gas sensor with ZnO-nanocomposite/Si heterojunction diodes. A highly sensitive and rapid sensing gas nanosensor has been developed by exploiting the high surface area of the developed ZnO nanoparticles along with metal catalyst and field-assisted sensing. The dependence of sensor sensitivity and response-recovery times on size and density of ZnO nanoparticles, applied bias and gas concentration was studied.

#### **6.1 GAS DETECTION MECHANISM**

The basic principle of gas detection in surface sensitive metal oxide is the interaction of target gas with pre-adsorbed oxygen on sensor material and detection of conductivity change in sensor material which is directly related to change in the adsorbed oxygen concentration. The detection mechanism primarily involves surface reactions based on charge exchange. The charge exchange occurs between oxygen molecules and sensor material surface during adsorption, between reducing/oxidizing target gas and pre-adsorbed oxygen and between sensor material and reduced/oxidized oxygen. This results in a change in conductivity of the sensor material. The change in conductivity is directly related to the amount of a specific gas

present in the environment, resulting in a quantitative sensing of gas presence and concentration.

Thus, for improved sensor performance, sensor material with highly reactive surface and high surface area is desired to maximize the concentration of adsorbed oxygen and as a result maximize surface reactions with target gas. For this purpose, we employed the developed ZnO nanoparticles as a high surface area sensor material to develop our novel high performance gas sensor. ZnO has a highly reactive surface with its high concentration of unsaturated (dangling) surface bonds. It has a surface with a high isoelectric point (IEP) of 9.5, which is substantially higher than most gases and provides a strong driving force for the gas molecules to adsorb on the surface, hence making it the metal oxide of choice for gas sensing applications. Furthermore, metal catalyst was used on the surface of the nanoparticles to make target gas reactive for efficient reaction with pre-adsorbed oxygen and enable sensing at room temperature. In addition, fast detection mechanism is desired for detecting the change in conductance of the sensor material for which field-assisted processes were introduced in the gas sensor.

The gas detection mechanism of the room temperature nanosensor developed in our work includes the sequential operation of the following processes (fig. 6-1):

- 1) catalytic reaction of the surface contact metal and target gas forming radical complex,
- 2) reducing reaction of the radical complex and pre-adsorbed oxygen on nanoparticle surfaces and subsequent release of electrons to nanoparticle surface and
- 3) field-assisted detection of the change in conductivity of the nanoparticles.

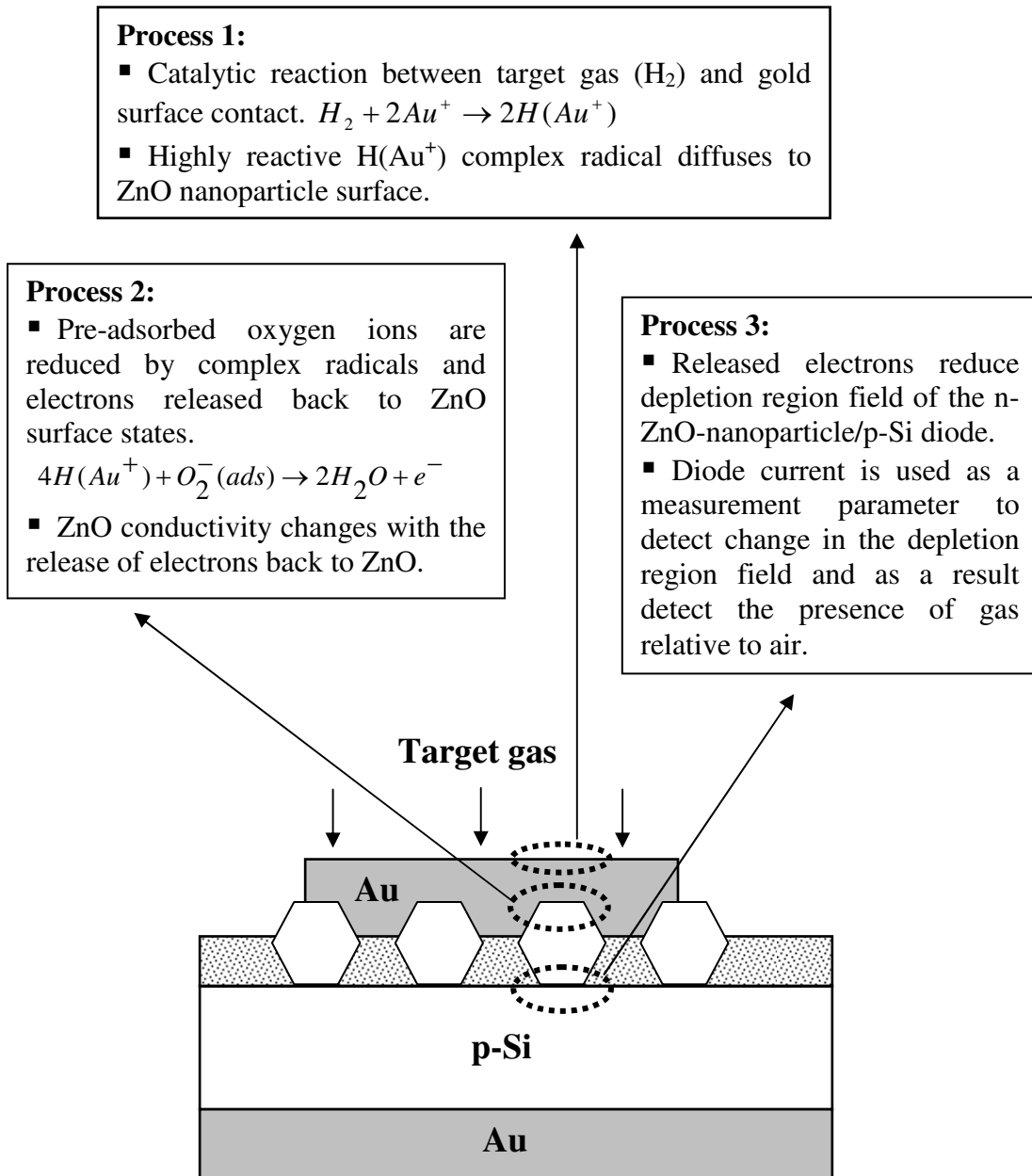


**Figure 6- 1. Schematic of the Au/ZnO-nanocomposite/Si structure developed for the realization of the novel nanosensor in our work with the three sequential processes involved in the gas detection mechanism labeled.**

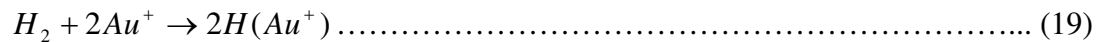


**6.1.1 ZnO Surface Metal and Target Gas Catalytic Mechanism**

As mentioned earlier, gas detection in surface sensitive metal oxide gas sensors largely involves surface reactions. To amplify sensor response, reactions between surface and target gas needs to be accelerated. A catalyst usually serves this purpose by providing an alternate path for reactions that has lower activation energy than the original chemical reaction and as a result speeds up the rate of reaction. This is often done by breaking down gas molecules into radicals which are more reactive than the molecules themselves.

For the development of our nano gas sensors, Au contacts on ZnO-copolymer nanocomposite films on p-Si were introduced as a catalyst and hydrogen was used as a target gas. Our previous work with ZnO thin films with Au nanoclusters [105] showed promising gas sensing properties indicating that Au has an efficient catalytic action for hydrogen through the formation of a complex radical. Other oxides like Fe<sub>2</sub>O<sub>3</sub> and SnO<sub>2</sub> also have found the presence of Au clusters to lower operating temperatures [106].

The hydrogen gas molecules arriving at the surface of the Au contacts decomposes to its atomic state which is more reactive and as such forms a highly reactive complex with Au. The reaction takes place as follows [107]:



The catalytic reaction and formation of radicals is followed by diffusion of the radical complexes to the metal-ZnO interface for interaction with the pre-adsorbed oxygen.

This interaction is the next step in the gas detection process which will be discussed in the section below.

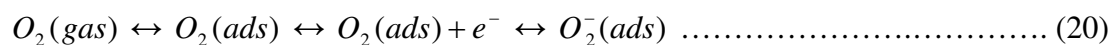
There was a secondary purpose for the Au metal surface layers. It was to provide increased surface area for oxygen adsorption beside the ZnO surface. The oxygen can be loosely attached to surfaces of the metal layer at the interface with the ZnO layer, thus doubling the surface area for interaction with hydrogen.

### 6.1.2 Reducing Gas Direct Interaction with ZnO Surface

The formation of hydrogen radical complex (discussed in previous section) is followed by the reduction reactions of the pre-adsorbed oxygen ions on ZnO surface by the radical complexes.

Pre-adsorption of oxygen – ZnO like many n-type metal oxides have oxygen deficient surface layer which is not in equilibrium with the bulk. These oxygen deficiencies are in the form of oxygen vacancies on ZnO surfaces which creates donor-like surface states. This causes adsorption of oxygen from atmosphere in an attempt to restore equilibrium. The commonly known adsorbed oxygen ions on ZnO surfaces in air are in the form of  $O_2^-$ ,  $O^-$ , and  $O^{2-}$  [108, 109]. However, the radical ion  $O_2^-$  is the most thermodynamically stable at temperatures below 100°C [110].

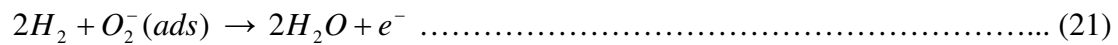
This is formed by the following reaction:



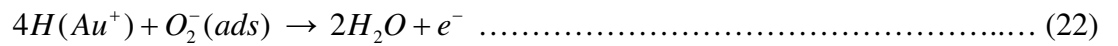
where  $e^-$  is the free electron in the semiconductor. The oxygen molecules in atmosphere first gets weakly bound to ZnO surface by Van der Waals forces by a process of physisorption. This is followed by the formation of negatively charged

radical ion  $O_2^-$  by a process of chemisorption where the weakly adsorbed oxygen molecules reacts with free electrons of donor-like surface states of ZnO. This transfer of free electrons from the conduction band of ZnO produces a space charge region at the ZnO surface and reduces the conductivity of the material. Formation of the surface depletion region also results in a schottky type barrier at the surface due to surface band bending. As will be discussed next, this barrier is lowered in the presence of a reducing gas.

Reducing reactions on ZnO surface - In the presence of a reducing gas like hydrogen on ZnO surface, the adsorbed oxygen ion reacts as follows [105]:



However, when the hydrogen molecule is oxidized and forms a radical in the presence of a catalyst as in the case of our nano gas sensors, the reaction becomes as follows [105]:



The rate of reaction in eq. (22) is faster than that in eq. (21) due to lower activation energy needed to react with a reactive radical like  $H(Au^+)$  than molecular hydrogen. The reactions are exothermic in nature [109] which helps the water molecules to be desorbed from ZnO surface. We can see from these reactions that the electrons trapped by adsorbed oxygen are released. These electrons return back to the conduction band of ZnO, which leads to an increase in the conductivity of the material.

The next step in the gas detection process as discussed below is the measurement of these variations in conductivity of ZnO in the presence of a reducing gas with to air. Most often resistance is used as the measurement parameter to evaluate these changes in conductivity. However for efficient and rapid detection of these changes, we have introduced an additional field-assisted process as rapid detection of these changes translates to fast sensor response.

### **6.1.3 Field Assisted Gas Detection by n- ZnO/p-Si Heterojunction Diodes**

The n-ZnO-copolymer-nanocomposite/Si heterojunction diode (discussed in the previous chapter) provided the means for field assisted detection of the conductivity change due to charge exchange on the ZnO nanoparticle surfaces when exposed to hydrogen (or reducing gas). In this process, the diode current is used as a measurement parameter for detecting changes in the conductivity of the ZnO in the presence of a target gas with respect to air. As the n-type ZnO nanoparticles are fairly small the depletion region edge of the heterojunction diode are expected to be close to the nanoparticle surface and as such any change in the surface charges affects the depletion region thus affecting the diode current flow. In the presence of a reducing gas, the electrons returned back to the shallow donor surface states (discussed earlier), re-emit to the conduction band in the quasi-neutral region of the n-ZnO nanostructures and by drift and diffusion enter the depletion region, emit over the heterojunction barrier into Si, and as a result increase forward current. Thus changes in the surface states and as a result in conductivity of the ZnO nanoparticles induced by the reducing gas are detected by the diode current.

## 6.2 EXPERIMENTAL DETAILS

Au/ZnO-nanocomposite/Si structure shown in fig. 6-2 was used for realization of our novel gas sensor. The gas sensors were developed for both the 250 nm and 20 nm ZnO nanoparticle systems. The Au contacts on the nanocomposite films were of 0.5 mm in diameter and 50 nm in thickness and that on the back of the p-Si substrate were of 100 nm in thickness with a larger area. The contacts were deposited by thermal evaporation in a high vacuum chamber under a pressure of  $10^{-6}$  torr. The sensor was evaluated by measuring I-V characteristics of the heterojunction using a HP4155C semiconductor analyzer under two different concentrations of H<sub>2</sub>, a flow of 10% and 3% H<sub>2</sub> in N<sub>2</sub> carrier gas. The gas was released on the test sample that was setup for I-V measurements on a probe station. The measurements were carried out at room temperature. The gas flow was controlled by a calibrated flowmeter set at 1000 sccm for our measurements. The relative response of the sensor to hydrogen was evaluated using the following definition of sensitivity,  $S = (I_{\text{gas}} - I_{\text{air}}) / I_{\text{air}}$ , where  $I_{\text{air}}$  is the forward current for a specific bias value in air while  $I_{\text{gas}}$  is the forward current in the gas flow for the same bias value.

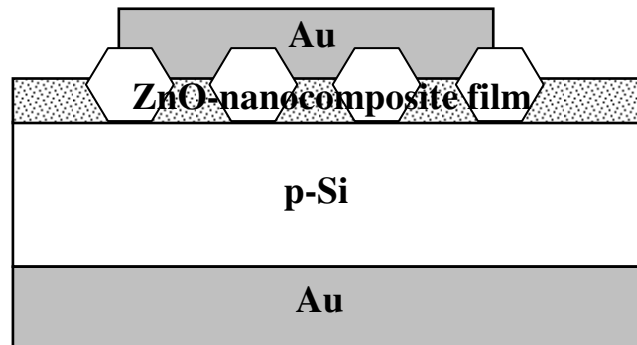


**Figure 6-2. Schematic of ZnO-nanocomposite/p-Si structure used for H<sub>2</sub> gas sensing measurements at room temperature**

### 6.3 GAS SENSING PROPERTIES OF Au/ZnO-[PS]<sub>159</sub>[PAA]<sub>63</sub>/Si

#### HETEROJUNCTION DIODES

Fig. 6-3 shows the forward I-V characteristics of the Au/ZnO-[PS]<sub>159</sub>/[PAA]<sub>63</sub>/Si heterojunction diode with the 250 nm ZnO nanoparticles in the presence and absence of 10% H<sub>2</sub> (N<sub>2</sub> carrier gas) gas at room temperature. The plot shows the diode current for every min of H<sub>2</sub> exposure and for every min after H<sub>2</sub> was removed with respect to air. The current increased significantly after the first min of H<sub>2</sub> exposure with respect to air and increased further in small measures for the next few minutes. The change in current between 2, 3 and 4 min of H<sub>2</sub> exposure was almost negligible, thus the sensor response became saturated after 2 min in H<sub>2</sub> environment. The observed current increase was due to the release of electrons into the conduction band of the nanoparticles from the adsorbed surface oxygen reduced in the H<sub>2</sub> gas environment. It was also observed from the I-V plot that on removing H<sub>2</sub> the forward current decreased and after 2 min the current returned to its value in air. In the absence of H<sub>2</sub>, the oxygen molecules in the atmosphere are adsorbed back to the nanoparticle surfaces and as a result electrons are removed from the nanoparticle, thus decreasing the forward current flow.

Fig. 6-4 shows the dynamic response of the nano-sensor to the presence and absence of 10% H<sub>2</sub> gas at different applied voltages. The sensor response was evaluated from the I-V plot of fig. 6-3 using the relation,  $S = (I_{H_2} - I_{AIR}) / I_{AIR}$ , where S is the sensitivity of the sensor, I<sub>AIR</sub> is the forward current for a specific bias in air while I<sub>H<sub>2</sub></sub> is the forward current in the H<sub>2</sub> environment for the same bias. The dynamic

## CHAPTER 6: ZnO GAS NANO-SENSOR DEVICES

response was plotted for different applied biases to examine the dependence of sensor sensitivity on applied bias and to determine the optimal bias for the nano-sensor performance. From fig. 6-4, the optimal bias was found to be 3 V which gave the maximum sensitivity value of 104 %. Sensitivity decreased for biases above or below the optimal bias. This can be explained from our electrical studies of this diode (discussed earlier) which showed that diode current increased exponentially until the series resistance effects became pronounced above 3V. Thus the sensor response increases with increasing bias until the series resistance effects dampens the sensor response above 3V bias. The response time, defined as the time taken by the sensor to reach 90% of its maximum sensitivity value in presence of a gas was evaluated from fig. 6-4 and was found to be 60 sec for optimal bias of 3V. The response times for biases that corresponds to the exponential region of the I-V characteristics (fig. 5-18) of the diode were also 60 sec. The recovery times, defined as the time taken by the sensor to drop down to 10% of its maximum sensitivity value on removal of a gas were also evaluated and a full recovery was observed after 120 min.

The sensor sensitivity and response-recovery times were also tested in 3% H<sub>2</sub> gas at room temperature. Fig. 6-5 shows the dynamic response of the sensor evaluated from the forward I-V characteristics measured in the presence and absence of 3% H<sub>2</sub> gas. The response is shown for two measurement cycles of 2 min in H<sub>2</sub> gas and 1 min in air. There was a significant decrease in sensitivity, from 104% to 26% in the first cycle and to 24% in the second cycle. The decrease in sensitivity is due to the decrease in the amount of adsorbed oxygen reduced by the lower H<sub>2</sub> concentration. This results in a decrease in the electrons released back from the reduced surface

oxygen to the nanoparticles and consequently drop in the diode forward current. The response time was evaluated to be 75 sec and recovery time was 60 sec for both the cycles. The response time was found to be a function of gas concentration. With decrease in concentration the response time decreased from 60 to 75 sec.

This sensor with the large 250 nm ZnO nanoparticles shows rapid, low temperature detection capabilities. However, the performance was further improved to respond faster with higher sensitivity at room temperature with the application of smaller and denser ZnO nanoparticles, as will be discussed in the section below.

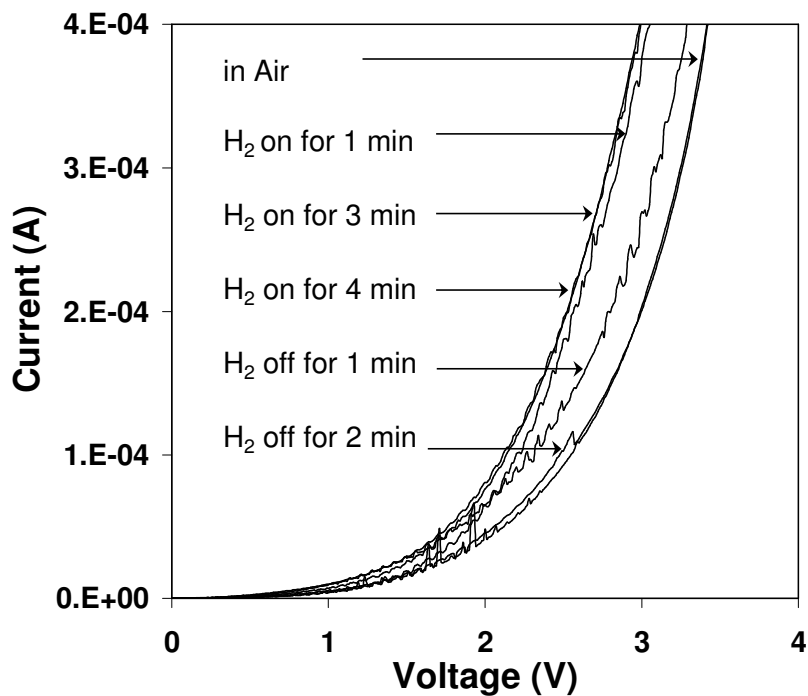


**Figure 6-3. I-V characteristics of ZnO-nanocomposite/p-Si heterojunction in [PS]<sub>159</sub>/[PAA]<sub>63</sub> copolymer system, with the 250nm average sized ZnO particles, under 10% H<sub>2</sub> (N<sub>2</sub> carrier gas) flow, at room temperature**



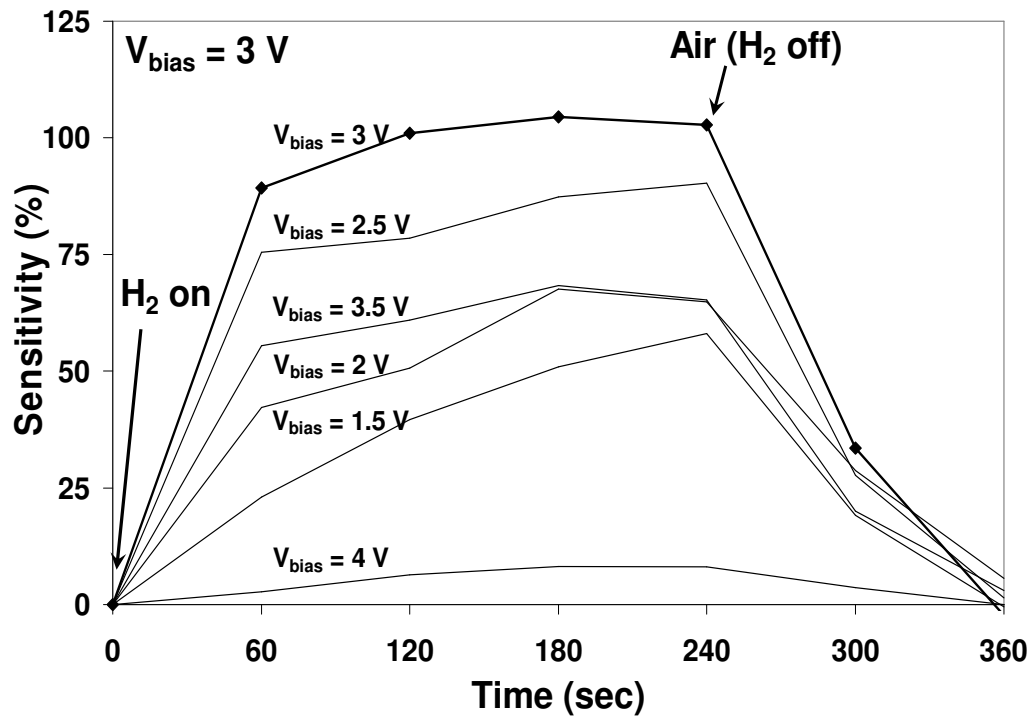


**Figure 6-4. Dynamic response of ZnO-nanocomposite/Si p-n heterojunction in [PS]<sub>159</sub>/[PAA]<sub>63</sub> copolymer system, with the 250nm average sized ZnO particles, under 10% H<sub>2</sub> (N<sub>2</sub> carrier gas) flow, at room temperature for different applied voltages**

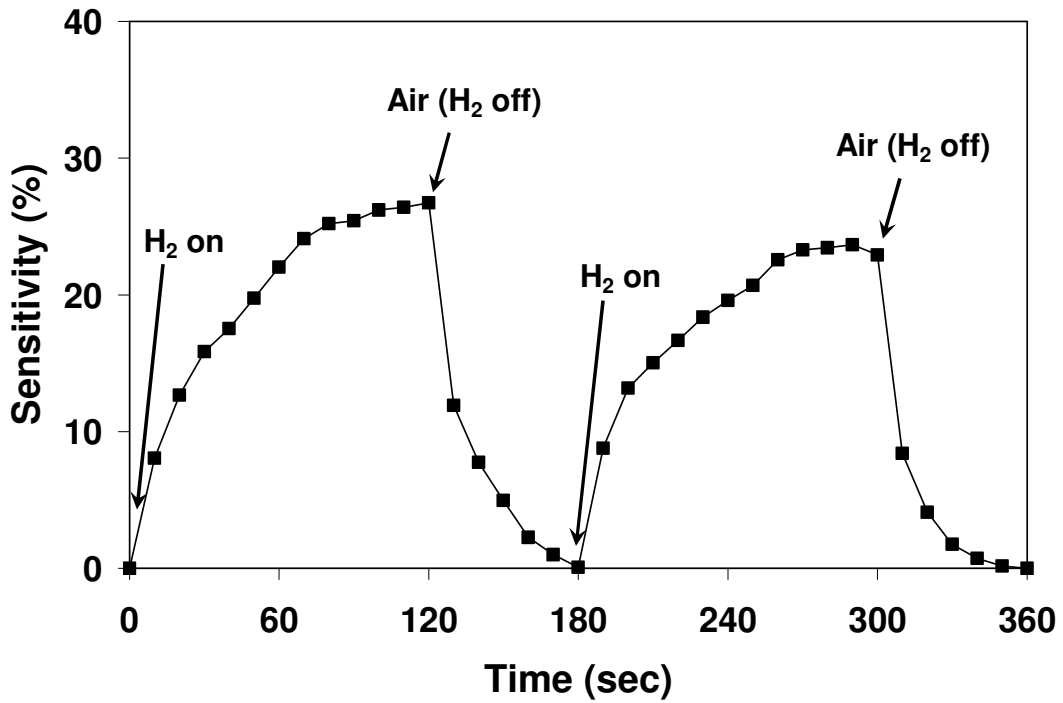


Figure 6-5. Dynamic response of ZnO-nanocomposite/Si p-n heterojunction in [PS]<sub>159</sub>/[PAA]<sub>63</sub> copolymer system, with the 250nm average sized ZnO particles, under 3% H<sub>2</sub> (N<sub>2</sub> carrier gas) flow, at room temperature

#### 6.4 GAS SENSING PROPERTIES OF Au/ZnO-[PS]<sub>106</sub>[PAA]<sub>4</sub>/Si

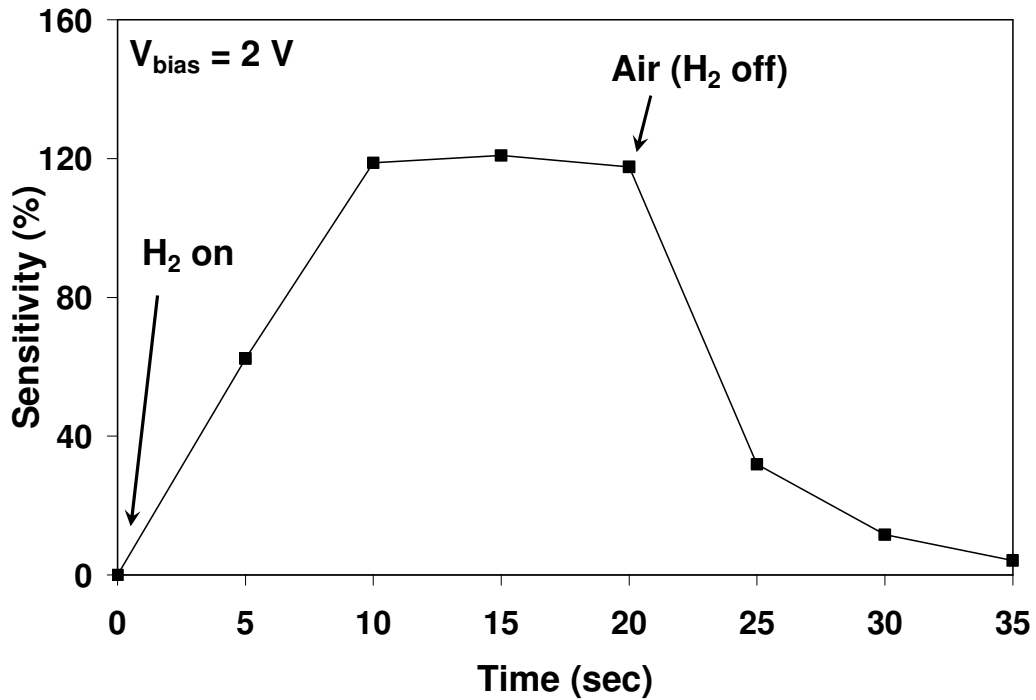
##### HETEROJUNCTION DIODES

Fig. 6-6 shows the dynamic response of the Au/ZnO-[PS]<sub>106</sub>/[PAA]<sub>4</sub>/Si heterojunction diode with the 20 nm ZnO nanoparticles to the presence and absence of 10% H<sub>2</sub> gas at room temperature. The sensor response was evaluated from the I-V measurements made for every 5 sec of H<sub>2</sub> exposure and for every 5 sec after H<sub>2</sub> was removed with respect to air. The optimal bias for the maximum sensitivity of 120% was found to be 2V for this nano-sensor as shown in fig. 6-6. This optimal bias corresponds to the high injection region of the Au/ZnO-[PS]<sub>106</sub>/[PAA]<sub>4</sub>/Si heterojunction diode before the series resistance effects become pronounced as observed from our electrical studies of this diode. The response time was 10 sec and recovery time was 15 sec for this nano-sensor.

Fig. 6-7 shows the dynamic response of this nano-sensor in 3% H<sub>2</sub> environment at room temperature. With the concentration of H<sub>2</sub> reduced, the maximum sensitivity of the sensor dropped to 55% and the response-recovery times increased to 15 and 20 sec, respectively.

Comparing the sensor performance of the two nano-sensors developed showed that the sensitivity and response-recovery times improved with the application of the smaller and denser ZnO nanoparticles in the ZnO-nanocomposite/Si n-p heterojunction diodes. This is due to the increase in surface area compared to the larger nanoparticles. Thus for the same concentration of H<sub>2</sub>, the surface reactions were increased with due to increased area of adsorbed surface oxygen. Increased

surface reactions translate to increased forward current per unit time which increases the sensitivity and response times of the sensor.



**Figure 6-6. Dynamic response of ZnO-nanocomposite/Si p-n heterojunction in [PS]<sub>106</sub>/[PAA]<sub>4</sub> copolymer system, with the 20nm average sized ZnO particles, under 10% H<sub>2</sub> (N<sub>2</sub> carrier gas) flow, at room temperature**

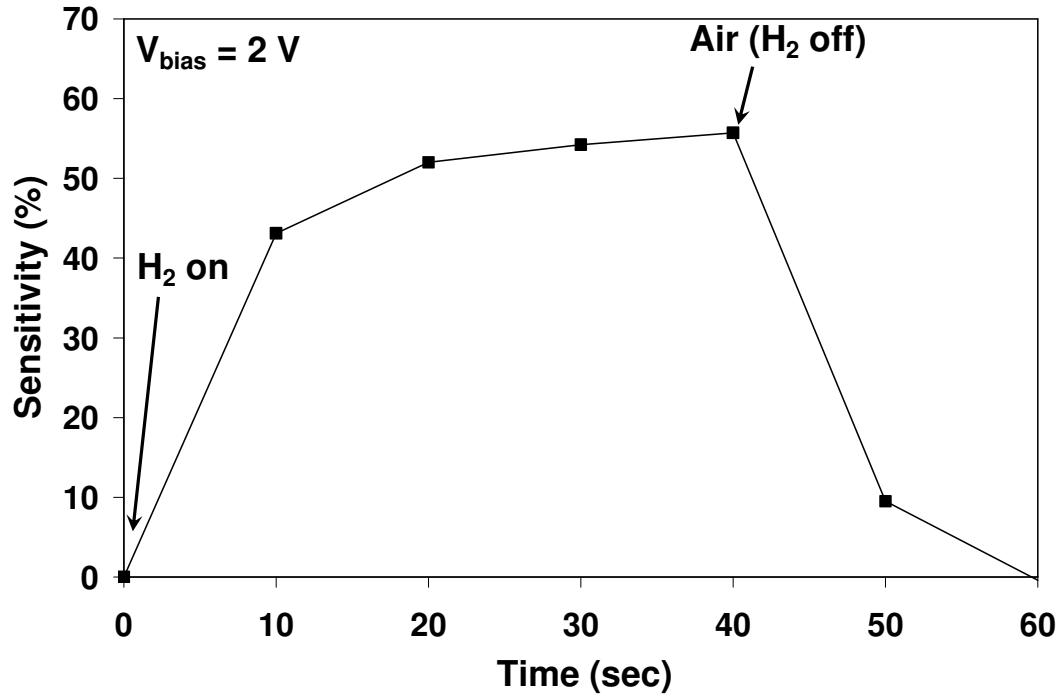


**Figure 6-7. Dynamic response of ZnO-nanocomposite/Si p-n heterojunction in [PS]<sub>106</sub>/[PAA]<sub>4</sub> copolymer system, with the 20nm average sized ZnO particles, under 3% H<sub>2</sub> (N<sub>2</sub> carrier gas) flow, at room temperature**

	Nanosensor with the 250 nm sized and $10^7 \text{ cm}^{-2}$ density ZnO nanoparticles		Nanosensor with the 20 nm sized and $10^{10} \text{ cm}^{-2}$ density ZnO nanoparticles	
H <sub>2</sub> gas concentration	10% H <sub>2</sub>	3% H <sub>2</sub>	10% H <sub>2</sub>	3% H <sub>2</sub>
Optimal bias	3 V	3 V	2 V	2 V
Max. sensitivity	104%	26%	120%	55%
Response time	60 sec	75 sec	10 sec	15 sec
Recovery time	120 sec	60 sec	15 sec	20 sec

**Table 2. Summary of the gas sensing characteristics of the nanosensors**

## 6.5 SUMMARY

This chapter presents the development of a novel hydrogen gas nanosensor based on our developed ZnO-nanocomposite/Si heterojunction diode. A highly sensitive, rapid room temperature sensing was achieved with Au top electrodes, large surface area and high surface reactivity of the ZnO nanoparticles and field-assisted sensing of conductivity change in the nanoparticles in hydrogen environment. The nanosensors were developed and tested for ZnO nanoparticles with different sizes and densities at two different concentrations of hydrogen gas.

## CHAPTER 6: ZnO GAS NANO-SENSOR DEVICES

The nanosensor developed with the ZnO-[PS]<sub>159</sub>/[PAA]<sub>63</sub>/Si heterojunction diode having the 250 nm size and  $4 \times 10^7 \text{ cm}^{-2}$  density ZnO nanoparticles showed a maximum sensitivity of 104 % with a response-recovery times of 60 and 120 sec, respectively, in 10% hydrogen. The sensitivity was reduced to 26% when exposed to 3% hydrogen and the response-recovery times were found to be 75 and 60 sec, respectively. The sensitivity of the nanosensor was found to be bias dependent and the optimal bias for these nanosensors was found to be 3 V.

The nanosensor developed for smaller (20 nm) and denser ( $10^{10} \text{ cm}^{-2}$ ) ZnO nanoparticles with the ZnO-[PS]<sub>106</sub>/[PAA]<sub>4</sub>/Si heterojunction diode showed higher sensitivity and faster response-recovery times in comparison to the larger particle nanosensors at an optimal bias of 2 V. The smaller nanosensors showed a maximum sensitivity of 120% with a response-recovery times of 10 and 15 sec, respectively, in 10% hydrogen. The sensitivity was reduced to 55% in 3% hydrogen environment with the response-recovery times of 15 and 20 sec, respectively. Thus increasing the ZnO surface area improved nanosensor performance significantly.

## **CHAPTER 7: CONCLUSIONS**

### **7.1 SUMMARY**

This thesis presents the functionalization of ZnO nanoparticles on large area Si wafers through diblock copolymer self-assembly, and the development of ZnO nanoparticle-based heterojunction diode and high performance hydrogen gas sensor for the first time. Since the ZnO nanoparticles have the advantage of size dependent UV optical properties and highly reactive large surface area over its bulk counterparts, functionalization of the nanoparticles on substrates and realization of p-n junction diodes with the nanoparticles open up new promising avenues for advanced nanoelectronic devices and applications. The novel highly sensitive, fast responsive, room temperature operational hydrogen gas sensor realized with the ZnO nanoparticle-based diode in our work demonstrates the potential of functionalized ZnO nanoparticles on Si for novel nanodevices.

In our work, self-assembly of ZnO nanostructures with spherical morphology on Si substrates were achieved by using the intrinsic nanoscale domains of diblock copolymers as templates which was validated by XPS, FTIR and SEM. Compatibility of the ZnO-nanocomposite on Si with standard CMOS technology like photolithographic patterning, metallization and reactive ion etching showed potential for monolithic integration of functionalized ZnO nanoparticles with CMOS circuits.

AFM studies validated the size and density control of the ZnO nanoparticles with copolymer block lengths which showed one of the advantages of using diblock copolymer self-assembly approach. Among the four configurations of copolymer



## CHAPTER 7: CONCLUSIONS

used, the block length ratio of 159/63 gave the largest nanostructures with sizes of 250 nm and densities of  $1 \times 10^7 \text{ cm}^{-2}$  while the block length ratio of 106/4 gave the smallest nanostructures with sizes of 20 nm and densities of  $1 \times 10^{10} \text{ cm}^{-2}$ . Correlation between the particle parameters and the copolymer block lengths (m, n) were evaluated from AFM studies. X-ray diffraction revealed wurtzite structure with dominant orientation along (100) that of Si substrate suggesting pseudo-epitaxial nature of the nanoparticles. Photoluminescence obtained from the 250 nm ZnO nanostructures at room temperature showed a UV emission peak at 372 nm and that obtained from the 20 nm ZnO showed a blue shifted peak at 363 nm. The blue shifted luminescence is in agreement with size quantum confinement effect in the smaller particles.

The nanoparticles on p-type Si resulted in the development of a ZnO-nanocomposite/pSi n-p heterojunction diode. The nanodiode showed good rectification and low leakage currents. The 250nm-ZnO-nanocomposite/Si heterojunction showed rectifying properties with saturation current of  $3 \times 10^{-8} \text{ A}$ , a built-in voltage of 0.7 eV, and an ideality factor of 5.7. C-V measurements indicated an abrupt n-ZnO/p-Si junction with built-in voltage of 0.75 V in good agreement with that measured from I-V measurements and donor concentration of  $3 \times 10^{15} \text{ cm}^{-3}$  in ZnO nanoparticles. The heterojunction diode with smaller and denser ZnO nanoparticles also showed rectifying diode properties with saturation current of  $2 \times 10^{-8} \text{ A}$ , a built-in voltage of 0.69 eV, and an ideality factor of 5.9. Evaluation of the diode transport mechanisms showed dominant recombination in depletion region in both the large and small diodes below the high injection level. However above this bias the current

## CHAPTER 7: CONCLUSIONS

transport became space charge limited in the smaller diodes as a consequence of the larger band gap of the smaller nanoparticles.

Sensor performance of the hydrogen gas nanosensors developed with ZnO-nanocomposite/Si heterojunction diodes were evaluated for the larger and smaller nanoparticles in two different concentrations of hydrogen. The nanosensor with the smaller and denser nanoparticles showed higher sensitivity and faster response-recovery times of several tens of seconds than the larger particle nanosensor. Thus the nanosensor performance was significantly improved with increased surface area.

### 7.2 FUTURE WORK

The current study demonstrated the synthesis of device quality ZnO nanoparticles through diblock copolymer self-assembly on large area Si wafers with CMOS compatible techniques developed in our work. These novel nanoparticle synthesis techniques can be applied to develop working nanodevices using metal oxide semiconductors and Si wafers in a pseudo-epitaxial heterojunction system.

This opens up new possibilities for the development of advanced optoelectronic, sensor, and magnetic storage nanodevices based not only on ZnO-Si but also on other important metal oxide semiconductors like MgO, SnO<sub>2</sub>, MnO and NiO, on Si wafers or other technologically important large area substrates.

The thesis presented the development of ZnO-nanocomposite/Si n-p heterojunction nanodiodes for the first time and the study of their current transport properties. Further temperature dependent electrical characterization of these

## CHAPTER 7: CONCLUSIONS

nanodiodes will help substantiate the theory of recombination presented here to account for the current behavior observed in these nanodiodes.

The high performance gas nanosensors demonstrated in the thesis can be further improved and incorporated in a fully integrated IC chip. The development of these nanosensors for other toxic gases is a natural extension of this thesis.

Furthermore, opto-electronic nanoscale devices like UV nano-photodetectors, UV nano-LEDs and UV nano-lasers can be realized with the ZnO-nanocomposite/Si n-p heterojunction nanodiodes with the size-dependent optical properties of the ZnO nanoparticles reported in this thesis.

## BIBLIOGRAPHY

- [1] D. Hwang, S. Kang, J. Lim, E. Yang, J. Oh, J. Yang, and S. Park, “*p*-ZnO/*n*-GaN heterostructure ZnO light-emitting diodes”, *Appl. Phys. Lett.*, vol. 86, pp 222101, 2005.
- [2] S. J. Jiao, Z. Z. Zhang, Y. M. Lu, D. Z. Shen, B. Yao, J. Y. Zhang, B. H. Li, D. X. Zhao, X. W. Fan, and Z. K. Tang, “ZnO *p-n* junction light-emitting diodes fabricated on sapphire substrates”, *Appl. Phys. Lett.*, vol. 88, pp 031911, 2006.
- [3] T. Moon, M. Jeong, W. Lee, and J. Myoung, “The fabrication and characterization of ZnO UV detector”, *Applied Surface Science*, vol. 240, pp 280-285, 2005.
- [4] P. M. Verghese, and D. R. Clarke, “Piezoelectric contributions to the electrical behavior of ZnO varistors”, *J. Appl. Phys.*, vol. 87, pp 4430- 4438, 2000.
- [5] S. S. Lee and R. M. White, “Self-excited piezoelectric cantilever oscillators”, *Sensors and Actuators A: Physical*, vol. 52, pp 41-45, 1996.
- [6] T. H. Aeugle, H. Bialas, K. Heneka, and W. Pleyer, “Large area piezoelectric ZnO transducers produced by R.F. diode sputtering”, *Thin Solid Films*, vol. 201, pp 293-304, 2001.
- [7] K. K. Zadeh, A. Trinchi, W. Wlodarski, and A. Holland, “A novel Love-mode device based on a ZnO/ST-cut quartz crystal structure for sensing applications”, *Sensors and Actuators A: Physical*, vol. 100, pp 135-143, 2002.

## BIBLIOGRAPHY

- [8] S. M. Chou, L. G. Teoh, W. H. Lai, Y. H. Su, and M. H. Hon, "ZnO:Al Thin Film Gas Sensor for Detection of Ethanol Vapor", *Sensors*, vol. 6, pp 1420-1427, 2006.
- [9] M. S. Wagh, G. H. Jain, D. R. Patil, S. A. Patil, and L.A. Patil, "Modified zinc oxide thick film resistors as NH<sub>3</sub> gas sensor", *Sensors and Actuators B: Chemical*, vol. 115, pp 128-133, 2006.
- [10] J. Yoo, J. Lee, S. Kim, K. Yoon, I. Park, S. K. Dhungel, B. Karunagaran, D. Mangalaraj and J. Yi, "High transmittance and low resistive ZnO:Al films for thin film solar cells", *Thin Solid Films*, vol. 480-481, pp 213-217, 2005.
- [11] S. Mahamuni, K. Borgohain, B. S. Bendre, V. J. Leppert, and S. H. Risbud, "Spectroscopic and structural characterization of electrochemically grown ZnO quantum dots", *J. Appl. Phys.*, vol. 85, pp 2861, 1999.
- [12] H. A. Ali, A. A. Iliadis, A. V. Cresce, P. Kofinas, and U. Lee, "Properties of self-assembled ZnO nanostructures on Si and SiO<sub>2</sub> wafers", pp 454-457, 2001.
- [13] H. A. Ali, A. A. Iliadis, R. F. Mulligan, A. V. W. Cresce, P. Kofinas, and U. Lee, "Properties of self-assembled ZnO nanostructures", *Solid-State Electronics*, vol. 46, pp 1639-1642, 2002.
- [14] X. Zhao, Y. Xia, and G. M. Whitesides "Soft lithographic methods for nanofabrication", *J. Mater. Chem*, vol. 7, pp 1069-1074, 1997.
- [15] F. S. Bates and G. H. Fredrickson, "Block Copolymer Thermodynamics: Theory and Experiment", *Ann. Rev. Phys. Chem.*, vol. 41, pp 525-557, 1990.

## BIBLIOGRAPHY

- [16] E. M. Wong, P. G. Hoertz, C. J. Liang, B. Shi, G. J. Meyer, and P. C. Searson, "Influence of Organic Capping Ligands on the Growth Kinetics of ZnO Nanoparticles", *Langmuir*, vol. 17, pp 8362-8367, 2001.
- [17] A. N. Shipway, E. Katz, and I. Willner, "Nanoparticle Arrays on Surfaces for Electronic, Optical, and Sensor Applications", *ChemPhysChem*, vol. 1, pp 18-52, 2000.
- [18] S. Kim, S. Fujita, H. Parka, B. Yang, H. Kim, and D. Yoon, "Growth of ZnO nanostructures in a chemical vapor deposition process", *J. Crystal Growth*, vol. 292, pp 306–310, 2006.
- [19] S. Kim, T. Kotania, M. Uedaa, S. Fujita, and Shigeo Fujita, "Selective formation of ZnO nanodots on nanopatterned substrates by metalorganic chemical vapor deposition", *Appl. Phys. Lett.*, vol. 83, pp 3593-3595, 2003.
- [20] Y.J. Lia, R. Duana, P. B. Shia, and G. G. Qina, "Synthesis of ZnO nanoparticles on Si substrates using a ZnS source", *J. Crystal Growth*, vol. 260, pp 309–315, 2004.
- [21] S. Barik, A. K. Srivastava, P. Misra, R. V. Nandedkar and L. M. Kukreja, "Alumina capped ZnO quantum dots multilayer grown by pulsed laser deposition", *Solid State Comm.*, vol. 127, pp 463-467, 2003.
- [22] S. Kim, M. Uedaa, M. Funato, S. Fujita, and Shigeo Fujita, "Artificial control of ZnO nanodots by ion-beam nanopatterning", *J. Appl. Phys.*, vol. 97, pp 104316, 2005.

## BIBLIOGRAPHY

- [23] H. Z. Wua, D. J. Qiu, Y.J. Caia, X. L. Xua, and N. B. Chen, "Optical studies of ZnO quantum dots grown on Si(001)", *J. Crystal Growth*, vol. 245, pp 50–55, 2002.
- [24] C. S. Rout, S. H. Krishna, S. R. C. Vivekchand, A. Govindaraj, and C. N. R. Rao, "Hydrogen and ethanol sensors based on ZnO nanorods, nanowires and nanotubes", *Chem. Phys. Lett.*, vol. 418, pp 586-590, 2006.
- [25] H. T. Wang, B. S. Kang, F. Ren, L. C. Tien, P. W. Sadik, D. P. Norton, S. J. Pearton, and J. Lin, "Hydrogen-selective sensing at room temperature with ZnO nanorods", *Appl. Phys. Lett.*, vol. 86, pp 243503, 2005.
- [26] R. Rossetti, S. Nakahara, and L. E. Brus, "Quantum size effects in the redox potentials, resonance Raman spectra, and electronic spectra of CdS crystallites in aqueous solution", *J. Chem. Phys.*, vol. 79, pp 1086-1088, 1983.
- [27] A. L. Efros, and A. L. Efros, "Interband Absorption of Light in a Semiconductor Sphere" *Sov. Phys. Semicond.*, vol. 16, pp 772, 1982.
- [28] T. Vossmeier, L. Katsikas, M. Giersig, I. G. Popovic, and H. Weller, "CdS nanoclusters: synthesis, characterization, size dependent oscillator strength, temperature shift of the excitonic transition energy, and reversible absorbance shift", *J. Phys. Chem.*, vol. 98, pp 7665-7673, 1994.
- [29] A. N. Goldstein, C. M. Echer, and A. P. Alivisatos, "Melting in Semiconductor Nanocrystals", *Science*, vol. 256, pp. 1425-1427, 1992.
- [30] S. H. Tolbert, and A. P. Alivisatos, "High-Pressure Structural Transformations in Semiconductor Nanocrystals", *Annu. Rev. Phys. Chem.*, vol. 46, pp 595- 626, 1995.

## BIBLIOGRAPHY

- [31] Y. Kayanuma, "Wannier exciton in microcrystal", *Solid State Comm.*, vol. 59, pp 405-408, 1986.
- [32] Y. Kayamma, "Quantum-size effects of interacting electrons and holes in semiconductor microcrystals with spherical shape", *Phys. Rev. B*, vol. 38, pp 9797-9805, 1988.
- [33] D. Brust, J. C. Phillips and F. Bassani, "Critical Points and Ultraviolet Reflectivity of Semiconductors", *Phys. Rev. Lett.*, vol. 9, pp 94-97, 1962.
- [34] J. C. Slater and G. F. Koster, "Simplified LCAO Method for the Periodic Potential Problem", *Phys. Rev. B*, vol. 94, pp 1498-1524, 1954.
- [35] R. Viswanatha, S. Sapra, B. Satpati, P. V. Satyam, B. N. Dev and D. D. Sarma, "Understanding the quantum size effects in ZnO nanocrystals", *J. Mater. Chem.*, vol. 14, pp 61-668, 2004.
- [36] D. M. Mittleman, R. W. Schoenlein, J. J. Shiang, V. L. Colvin, A. P. Alivisatos, and C. V. Shank, "Quantum size dependence of femtosecond electronic dephasing and vibrational dynamics in CdSe nanocrystals", *Phys. Rev. B*, vol. 49, pp 14435-14447, 1994.
- [37] S. Sapra, J. Nanda, D. D. Sarma, F. Abed El-Al and G. Hodes, "Blue emission from cysteine ester passivated cadmium sulfide nanoclusters", *Chem. Comm.* vol. 21, pp 2188-2189, 2001.
- [38] O. Dabbousi, J. Rodriguez-Viejo, F. V. Mikulec, J. R. Heine, H. Mattoussi, R. Ober, K. F. Jensen and M. G. Bawendi, *J. Phys. Chem. B*, vol. 101, pp 9463 1997.



## BIBLIOGRAPHY

- [39] T. Castro, R. Reifengerger, E. Choi, and R.P. Andres, "Mechanochemical synthesis of intermetallic compounds", *Phys. Rev. B:Condens. Matter*, vol. 42, pp 8548, 1990.
- [40] R. D. Beck, P. St. John, M. L. Homer, and R. L. Whettten, "Impact-Induced Cleaving and Melting of Alkali-Halide Nanocrystals", *Science*, vol. 253, pp 879-883, 1991.
- [41] T. P. Martin, U. Naher, H. Schaber, and U. Zimmermann, "Evidence for a size-dependent melting of sodium clusters", *J. Chem. Phys.*, vol. 100, pp 2322, 1994.
- [42] S. H. Tolbert, and A. P. Alivisatos, "Size dependence of a first order solid-solid phase transition: the wurtzite to rock salt transformation in CdSe nanocrystals", *Science*, vol. 265, pp 373-376, 1994.
- [43] U. Ozgur, Y. I. Alivov, C. Liu, A. Teke, M. Reshchikov, S. Dogan, V. Avrutin, S. J. Cho, and H. Morkoc, "A comprehensive review of ZnO and related devices", *J. Appl. Phys.*, vol. 98, pp 041301, 2005.
- [44] F.J.V. Pressig, H. Zeng and E.S. Kim, "Measurement of piezoelectric strength of ZnO thin films in MEMS applications", *Smart Materials and Structures*, vol.7, pp 396-403, 1998.
- [45] H. Nakahata, S. Fujii, K. Higaki, A. Hachigo, H. Kitabayashi, S. Shikata and N. Fujimori, "Diamond based surface acoustic wave devices", *Semiconductor Science and Technology 1B*, vol. 18, no. 3, pp. S96-S104, 2003.
- [46] H.D Sun et .al, "Temperature dependence of Excitonic absorption spectra in ZnO/MgZnO multiquantum wells grown on lattice matched substrates" *Applied Physics Letters*, vol. 78, pp. 2464-2466, 2001.

## BIBLIOGRAPHY

- [47] K. L. Chopra, S. Major, and D. K. Pandya, "Transparent conductors—a status review," *Thin Solid Films*, vol. 102, p. 1, 1983.
- [48] F. S. Bates, M. F. Schulz, S. Forster, J. H. Rsedale, K. Almdal, and K. Mortensen, "Fluctuations, conformational asymmetry and block copolymer phase behavior", *Faraday Discuss*, vol. 98, pp 7-18, 1994.
- [49] M. Park, C. Harrison, P. M. Chaikin, R. A. Register, and D. H. Adamson, "Block Copolymer Lithography: Periodic Arrays of  $\sim 10^{11}$  Holes in 1 Square Centimeter", *Science*, vol. 276, pp 1401-1404, 1997.
- [50] H. C. Kim, X. Q. Jia, C. M. Stafford, D. H. Kim, T. J. McCarthy, M. Tuominen, C. J. Hawker, and T. P. Russell, "A route to nanoscopic SiO<sub>2</sub> posts via block copolymer templates", *Adv. Mater.*, vol. 13, pp 795-795, 2001.
- [51] R. E. Cohen, "Metal Nanoclusters within Block Copolymer Domains", *Polymeric Materials Encyclopedia*, vol. 6, pp 4143-4147, 1996.
- [52] J. F. Ciebien, R. T. Clay, B. H. Sohn, and R. E. Cohen, "Brief review of metal nanoclusters in block copolymer films", *New J. Chem.*, vol. 22, pp 685-691, 1998.
- [53] V. Sankaran, C. Cummins, R. R. Schrock, R. E. Cohen, and R. J. Silbey, "Small PbS clusters prepared via romp block copolymer technology", *J. Am. Chem. Soc.*, vol. 112, 6858-6859, 1990.
- [54] J. Yue, V. Sankaran, r. E. Cohen, and R. R. Schrock, "Interconversion of ZnF<sub>2</sub> and ZnS nanoclusters within spherical microdomains in block copolymer films", *J. Am. Chem. Soc.*, vol. 115, pp 4409-4410, 1993.

## BIBLIOGRAPHY

- [55] V. Sankaran, J. Yue, R. E. Cohen, R. R. Schrock and R. J. Silbey, "synthesis of zinc sulfide clusters and zinc particles within microphase-separated domains of organometallic block copolymers", *J. Chem. Mater.* vol. 5, pp 1133-1142, 1993.
- [56] J. Yue, and R. E. Cohen, *Supramolecular Sci.*, vol. 1, pp 117-122, 1994.
- [57] R. T. Clay, and R. E. Cohen, "Synthesis of metal nanoclusters within microphase-separated diblock copolymers: a 'universal' approach", *Supramolecular Sci.*, vol. 2, pp 183-191, 1995.
- [58] R. S. Kane, R. E. Cohen, and R. Silbey, "Synthesis of PbS nanoclusters within block copolymer nanoreactors", *Chem Mater.*, vol. 8, pp 1919-1924, 1996.
- [59] R. T. Clay, and R. E. Cohen, "Synthesis of metal nanoclusters within microphase-separated diblock copolymers: sodium carboxylate vs carboxylic acid functionalization", *Supramolecular Sci.*, vol. 5, pp 41-48, 1998.
- [60] K. Siegbahn, *ESCA Applied to Solids: Almqvist and Wiksells*, Uppsala, Sweden, 1967.
- [61] R. M. Silverstein, in *Spectrometric Identification of Organic Compounds*, 6<sup>th</sup> ed., Wiley, NY, 1998.
- [62] K. Nakamoto, in *Infrared and Raman Spectra of Inorganic and Coordination Compounds, Part B*, 5<sup>th</sup> ed., Wiley, NY, 1997.
- [63] L. Fiermans, R. Hoogewija, and J. Vennik, "Electron spectroscopy of transition metal oxide surfaces", *Surface Sci.*, vol. 47, pp 1-40, 1975.
- [64] *The NIST X-Ray Photoelectron Spectroscopy (XPS) Database Microform*, by C. D. Wagner, NIST Technical Note (1991).

## BIBLIOGRAPHY

- [65] *Handbook of X-Ray and Ultraviolet Photoelectron Spectroscopy*, edited by D. Briggs (Heydin and Son Ltd., London, 1988).
- [66] C. R. Cothorn, D. W. Langer and C. J. Veseley, *J. Elec. Spec. and Related Phen.*, vol. 3, pp 399, 1974.
- [67] S. Perkowitz, *Optical Characterization of Semiconductors: Infrared, Raman and Photoluminescence Spectroscopy*: Academic Press Inc, San Diego, 1993.
- [68] P. Dawson, G. Duggan, H. I. Ralph and K. Woodbridge, "Free excitons in room-temperature photoluminescence of GaAs-Al<sub>x</sub>Ga<sub>1-x</sub>As multiple quantum wells" *Physics Review B*, vol. 28, no. 12, pp. 7381-83, 1983.
- [69] R.A. Smith, *Semiconductors*: Oxford University Press p.109, Second Edition (1978)
- [70] K. Vanheusden, C. H. Seager, W. L. Warren, D. R. Tallant, and J. A. Voigt "Correlation between photoluminescence and oxygen vacancies in ZnO phosphors", *Appl. Phys. Lett.*, vol. 68, pp 403, 1996.
- [71] E.G. Bylander, "Surface effects on the low-energy cathodoluminescence of zinc oxide", *Journal of Applied Physics*, vol. 49, pp 1188-95, 1978
- [72] K. Vanheusden, C.H. Seager, W.L. Warren, D.R. Tallant and J.A. Voiget, "Correlation between photoluminescence and oxygen vacancies in ZnO phosphors", *Applied Physics Letters*, vol. 68, pp 403-405, 1996.
- [73] B.Lin, Z. Fu and Y. Zai, "Green luminescent center in undoped zinc oxide films deposited on silicon substrates", *Applied Physics Letters*, vol. 79, pp 943-945, 2001.

## BIBLIOGRAPHY

- [74] C. Sah, *Fundamentals of solid-state electronics*, World Scientific, p 437, 1991.
- [75] C. Sah, R. N. Noyce, and W. Shockley, "Carrier generation and recombination in P-N junctions and P-N junctions characteristics", *Proc. IRE*, vol. 45, pp 1228-1243, 1957.
- [76] R. L. Anderson, "Germanium-Gallium Arsenide Heterojunctions", *IBM Journal*, pp283-287, 1960.
- [77] X. Li, B. Zhang, H. Ahu, X. Dong, X Xia, Y. Cui, Y. Ma, and G. Du, "Study on the luminescence properties of n-ZnO/p-Si heterojunction diode grown by MOCVD", *J. Phys. D: Appl. Phys.*, vol. 41, pp 1-5, 2008.
- [78] T. L. Tansley, and S. J. T. Owen, "Conductivity of Si-ZnO p-n and n-n heterojunctions", *J. Appl. Phys.*, vol. 55, pp 454-459, 1984.
- [79] S. J. Pearton, D. P. Norton, K. Ip, Y. W. Heo, and T. Steiner, "Recent progress in processing and properties of ZnO", *J. Vac. Sci. Technol*, vol. 22, pp 932-940, 2004.
- [80] K. B. Sundaram, and A. Khan, "Work function determination of zinc oxide films", *J. Vac. Sci. Technol. A*, vol. 15, no. 2, pp. 428-430, 1997.
- [81] X. Li, B. Zhang, H. Ahu, X. Dong, X Xia, Y. Cui, Y. Ma, and G. Du, "Study on the luminescence properties of n-ZnO/p-Si heterojunction diode grown by MOCVD", *J. Phys. D: Appl. Phys.*, vol. 41, pp 1-5, 2008.
- [82] S. M. Sze, *Physics of Semiconductor Devices*, Wiley, New York, p 369, Second Edition, 1981.

## BIBLIOGRAPHY

- [83] K. Ip, Y. W. Heo, K. H. Baik, D. P. Norton, S. J. Pearton, S. Kim, J. R. LaRoche, and F. Ren, “Temperature-dependent characteristics of Pt Schottky contacts on n-type ZnO”, *Appl. Phys. Lett.*, vol. 84, pp 2835-2837, 2004.
- [84] E. Danielsson, C. M. Zetterling, M. Ostling, A. Nikolaev, I. P. Nikitina, and V. Dmitriev, “Fabrication and characterization of heterojunction diodes with HVPE-grown GaN on 4H-SiC”, *IEEE Trans. Electron Devices*, vol. 48, pp 444 – 449, 2001.
- [85] D. L. Smith, “Recombination currents in a p-n heterojunction diode”, *Physica Status Solidi (a)*, vol. 44, pp 381 – 390, 2006.
- [86] W. Yu, C. Wang, W. Lu, and S. Cui, “Deposition of n-type nanocrystalline SiC films and current transport mechanisms in nanocrystalline SiC/crystalline Si heterojunctions”, *Solid State Communications*, vol. 143, pp 228–231, 2007.
- [87] E. Danielsson, C. M. Zetterling, M. Ostling, K. Linthicum, D. B. Thomson, O. H. Nam, and R. F. Davis, “The influence of band offsets on the IV characteristics for GaN/SiC heterojunctions”, *Solid State Electronics*, vol. 46, pp 827-835, 2002.
- [88] A. A. Ibrahim, and A. Ashour, “ZnO/Si solar cell fabricated by spray pyrolysis technique”, *J. Mater. Science: Mater. Elec.*, vol. 17, pp 835-839, 2006.
- [89] A. G. Milnes, and D. L. Feucht, *Heterojunctions and Metal-Semiconductor Junctions*, Academic Press, New York and London, p 55, 1972.
- [90] J. D. Ye, S. L. Gu, S. M. Zhu, W. Liu, S. M. Liu, R. Zhang, Y. Shi, and Y. D. Zheng, “Electroluminescent and transport mechanisms of n-ZnO/p-Si heterojunctions”, *Appl. Phys. Lett.*, vol. 88, pp 1821121-1821123, 2006.

## BIBLIOGRAPHY

- [91] V. Nadenau, U. Rau, A. Jasenek, and H. W. Schock, "Electronic properties of CuGaSe<sub>2</sub>-based heterojunction solar cells. Part I. Transport analysis", *J. Appl. Phys.*, vol. 87, pp 584, 2000.
- [92] D. Song, D. Neuhaus, J. Xia, and A. G. Aberle, "Structure and characteristics of ZnO:Al/n-Si heterojunctions prepared by magnetron sputtering", *Thin Solid Films*, vol. 422, pp 180-185, 2002.
- [93] H. Bayhan, and A. S. Kavasoglu, "Tunnelling enhanced recombination in polycrystalline CdS/CdTe and CdS/Cu(In,Ga)Se<sub>2</sub> heterojunction solar cells", *Solid-State Electronics*, vol. 49, pp 991-996, 2005.
- [94] M. Topf, D. Meister, I. Dirnstorfer, G. Steude, S. Fischer, B. K. Meyer, A. Krtschil, H. Witte, J. Christen, T. U. Kampen, and W. Monch, "Electrical and optical properties of p-SiC:n-GaN heterostructures", *Materials Science and Engineering B*, vol. 50, pp 302-306, 1997.
- [95] M. I. Chaudhry, "Electrical Transport Properties of Crystalline Silicon Carbide/Silicon Heterojunctions", *IEEE Electron Devices Letters*, vol. 12, pp 670-672, 1991.
- [96] A. R. Riben, and D. L. Feucht, "Electrical Transport in nGe-pGaAs Heterojunctions", *Int. J. Electron.*, vol. 20, pp 583-599, 1966.
- [97] A. R. Riben, and D. L. Feucht, "NGe-pGaAs heterojunctions", *Solid-State Electron.*, vol. 9, pp 1055-1056, 1966.
- [98] J. M. Shah, Y. L. Li, T. Gessmann, and E. F. Schubert, "Experimental analysis and theoretical model for anomalously high ideality factors ( $\eta \gg 2.0$ ) in AlGaIn/GaN p-n junction diodes", *J. Appl. Phys.* vol. 94, pp 2627-2630, 2003.

## BIBLIOGRAPHY

- [99] C. Wang, G. Yang, H. Liu, Y. Han, J. Luo, C. Gao, and G. Zou, “Experimental analysis and theoretical model for anomalously high ideality factors in ZnO/diamond p-n junction diode”, *Appl. Phys. Lett.*, vol. 84, pp 2427-2429, 2004.
- [100] J. H. He, and C. H. Ho, “The study of electrical characteristics of heterojunction based on ZnO nanowires using ultrahigh-vacuum conducting atomic force microscopy”, *Appl. Phys. Lett.*, vol. 91, pp 2331051-2331053, 2007.
- [101] G. D. J. Smit, S. Rogge, and T. M. Klapwijk, “Enhanced tunneling across nanometer-scale metal–semiconductor interfaces”, *Appl. Phys. Lett.*, vol. 80, pp 2568-2570, 2002.
- [102] M. A. Lampert, and P. Mark, *Current Injection in Solids*, Academic New York, 1970.
- [103] R. Ghosh, and D. Basak, “Electrical and ultraviolet photresponse properties of quasicaligned ZnO nanowires/p-Si heterojunction”, *Appl. Phys. Lett.*, vol. 90, pp 2431061-2431063, 2007.
- [104] J. H. he, and C H Ho, “The study of electrical characteristics of heterojunction based on ZnO nanowires using ultrahigh-vacuum conducting atomic force microscopy”, *Appl. Phys. Lett.*, vol. 91, pp 2331051-2331053, 2007.
- [105] Ch. Pandis, N. Brilis, E. Bourithis, D. Tsamakias, H. Ali, S. Krishnamoorthy, A. Iliadis, and M. Kompitsas, “Low-Temperature hydrogen sensors based on Au nanoclusters and Schottky contacts on ZnO films deposited by pulsed laser deposition on Si and SiO<sub>2</sub> substrates”, *IEEE Sensors Journal*, vol. 7, pp 448-454, 2007.
- [106] D. Kohl, “Function and applications of gas sensors”, *J. Phys. D: Appl. Phys.*, vol. 34, pp R125-R149, 2001.



## BIBLIOGRAPHY

- [107] N. Brilis, C. Foukaraki, E. Bourithis, D. Tsamakis, A. Giannoudakos, M. Kompitsas, T. Xenidou, and, and A. Boudouvis, “Development of NiO-based thin film structures as efficient H<sub>2</sub> gas sensors operating at room temperatures”, *Thin Solid Films*, vol. 515, pp 8484-8489, 2007.
- [108] A. R. Raju, and C. N. R. Rao, “Gas-sensing characteristics of ZnO and copper-impregnated ZnO”, *Sensors and Actuators B*, vol. 3, pp 305-310, 1991
- [109] S. Saito, M. Miyayama, K. Kuomoto, and H. Yanagida, “Gas sensing characteristics of porous ZnO and Pt/ZnO ceramics”, *J. Am. Ceram. Soc.*, vol. 68, pp 40-43, 1985.
- [110] A. Bielánski, and J. Haber, *Oxygen in Catalysis*, CRC Press, 1<sup>st</sup> Edition, 1990.